Inertial Confinement Fusion Neutronics

Lee W. G. Morgan

A thesis submitted for the degree of
Doctor of Philosophy

The University of York
Department of Physics

December 2012

ABSTRACT

Since fire was first harnessed one million years ago, man's appetite for energy has become ever more insatiable. As we come close to the end of the fossil fuel era, new energy sources must be found as a matter of urgency. The utilisation of renewable energy sources, such as solar and wind, to completely satisfy the world energy demands would be an ideal scenario. However, the low energy density achieved by renewables as well as local opposition to the building of renewable energy infrastructure will ensure that renewable energy sources will continue to play a relatively minor role in the supply of electricity to the grid. Hence, high energy density energy sources must be employed in order to minimize local opposition to building new power stations, while sustaining the growing energy demands. Nuclear fission is a strong candidate for meeting these high energy demands due to its reliability and safety-driven new technologies. However, nuclear waste and accidents, such as Chernobyl and Fukushima, still remains a concern for many people; thus, other high energy density technologies must utilized in conjunction with fission and renewables in order to maintain energy stability without the loss of public approval. A technology which would revolutionise power production is that of nuclear fusion. However, technological complexities and limited funding ensure that commercial fusion power plants are still at least 30 years away.

In essence, fusion is a process whereby two light nuclei combine to form a larger nucleus. In order to meet binding energy requirements in the newly formed nucleus, energy is released in the form of gammas or particle kinetic energy. The ejected particles have a large amount of kinetic energy, which can be used to heat water and drive electricity generating turbines as in a conventional fossil fuel power plant. The proposed fuels for all mainstream fusion reactor concepts are deuterium, which can be extracted from sea water, and tritium, which can be manufactured on the power plant site using relatively small amounts of lithium. In order to initiate and maintain fusion reactions, the fusion fuel must be heated to approximately 100 million degrees Celsius, resulting in the fuel being in the plasma state.

Until fairly recently, the quest for safe and clean energy in the form of IFE has mainly been driven by areas of research relevant to formation and the ignition of the fuel. The understanding of this physics holds the key to creating a reactor that can efficiently and effectively ignite the fuel and release more energy than is supplied. However, in recent years, as these area of physics have become more understood and the reality of fusion gain actually occurring in the near future has become more apparent, the need to understand the physics and technology issues, which are peripheral to the reactor core, has become more important.

An area of research which is gaining popularity is reactor blanket technology. The blanket is a component which surrounds the fusion core whose main functionality includes: Shielding fusion reactor staff from harmful neutron radiation; absorbing the energy of the 14.1MeV neutrons emitted from the D-T reaction and using this energy to convert water into steam and drive turbines; producing tritium, via the ^{6}Li(n,α)T reaction, in order to maintain reactor tritium self-sufficiency.

In order to achieve this functionality, the neutron and materials physics must be understood in greater detail. The extremely high temperatures and neutron fluxes exert forces on the reactor walls which are much higher than experienced by fission reactors. It is vital that fusion energy is to produce energy with significantly less nuclear waste than is produced in the fission industry. To achieve this, blanket materials must be chosen such that they are adequately resilient to transmutation via neutron interactions. Thus, ensuring that the blanket materials, once decommissioned, will be classified as low or medium level nuclear waste and that the amount of such waste is minimal. In addition to environmental concerns, the transmutation of nuclides in the blanket, other than lithium, is not beneficial to the mechanical properties of the material which can reduce the blanket performance. A balance must be found between the addition of impurities, such as molybdenum and niobium in steels, to improve the mechanical properties of materials and the potential nuclear waste associated with the added chemicals. Thus, the study and control of nuclide transmutations within the blanket is crucial in determining the level of success of fusion reactors.

The production of tritium is an important function of the blanket, as without this function the reactor core would have no fuel to burn. In order for a fusion reactor to become commercially viable, the blanket must create at least 10% more tritium than the reactor core is burning. This is due to tritium decay, small losses of tritium to the environment and tritium retention within structural materials. The vast majority of tritium produced in the blanket is a result of neutron absorption of lithium-6, which then decays to tritium and releases an alpha particle as a by-product. As the blanket ages, the amount of lithium in blanket decreases and so does the rate of tritium production, hence a solid blanket needs to be replaced every 3-6 years in order to maintain a large enough tritium breeding rate to sustain the reactor core.

The concept of utilising the neutron energy, to create electricity, and a lithium blanket, to create tritium, has been studied extensively for magnetic confinement fusion (MCF) devices. Recent advancements in ICF research have lead to the realisation that ICF blanket technology (BT) must now be developed in order to ensure the technology is well understood by the time

that commercial scale ignition has been achieved experimentally. However, ICFBT is generally less developed when compared to MCFBT; MCFBT research cannot be assumed to be directly applicable to ICFBT due to the vast difference in temporal distribution of neutron radiation emitted by ICF and MCF confinement regimes which results in different transmutation rates, damage and tritium breeding rates.

This thesis includes an introduction to fusion and presents background theory of fusion blanket technology. The main features include the description and benchmarking of a fusion specific depletion code named FATI (Fusion Activation and Transport Interface), the development and evaluation of control theory applied to blanket impurity removal, the study of time-dependent depletion and the development of a fusion specific energy binning format for Monte-Carlo modelling.

Both fission and fusion neutronic calculations rely heavily on Monte-carlo neutron transport codes, such as MCNP. The most important and frequently used functions used within these codes is the calculation of reaction rates. Calculating reaction rates can be accomplished via the point-wise estimator approach, which is accurate but very computationally expensive, or the multi-group method, which is fast but can lack accuracy if an inappropriate energy group structure is used to bin the reaction energies. Jean-Christophe Sublet, CCFE, was planning to develop a energy group structure, to be used in conjunction with Monte-carlo calculations of fusion devices. Thus, this work was completed via a collaboration between the author and Jean-Christophe. This study concluded that a 16,000 group structure was required in order to achieve $< 5\%$ uncertainty. This study could potentially have a large impact on the group structure used in fusion activation calculations. The most commonly used group structure used for fusion activation analysis is comprised of only 175 groups. Thus, the 175 group calculations could be significantly over estimating activation. One might consider the over-estimation to be better than underestimating activation, however larger activation may result in the over-engineered radiation shields which will cost more and might have a negative effect on tritium breeding capability.

To date, no transport-burnup (T-B) codes exist which have been designed specifically for fusion activation and tritium breeding studies. Codes such as MONTEBURNS, MOCUP, VESTA etc have been designed for fission applications, hence they lack some features that are absolutely necessary for fusion studies. As a result of this, and the overlooking of the need for full T-B, very few T-B studies have been undertaken. Chapter 4 describes the methodology behind the T-B linking mechanism and then goes on to describe the FATI code. The FATI (Fusion Activation and Transport Interface) has been designed and produced by the solely by the author

of this thesis. The code has many fusion specific features, which are not evident in any other documented T-B code. Some of the basic features of the code were benchmarked against the VESTA code, developed by Wim Haeck. The author created VESTA input files, which were then sent to Wim at IRSN, where the simulation was completed. the benchmarking procedure showed that the majority of the calculations performed by the FATI code matched the calculations of the well tested and validated VESTA code, within acceptable margins. Large differences in the calculation of hydrogen and helium isotopes highlighted the different methods used to approach gas production in the FATI and VESTA codes. This is another case where the underlying physics of fission and fusion neutronics differs, which then leads to alternative methods of analysis. By means of tritium production and tritium breeding calculations with the FATI code, Chapter 4 also clearly shows the importance of full T-B calculations. Non T-B calculations can underestimate the tritium self-sufficiency time by 60-70%, whilst some activation products be underestimated by up to hundreds/thousands of percent.

In summary, chapters 3 and 4 of this thesis will describe and test T-B methodology which has not yet been fully implemented in the study of fusion neutronics. Non-T-B calculations tend to underestimate activation whilst insufficient group structure energy resolution tends to overestimate activation. Further studies which take the findings of chapter 3 and 4 into account will need to be completed with more realised reactor geometries in order to increase the confidence in activation and tritium breeding calculations.

Due to the current shortage and cost of tritium the general consensus of fusion community is that tritium production should be maximised within future DEMO reactors. However, tritium is a highly radio-toxic and the calculations associated with the production of tritium within breeding blankets have high uncertainty. Thus, in order to ensure enough tritium is to be produced, the median tritium production level must be significantly higher than is required by tritium consumption of the reactor. This poses the risk of producing significantly more tritium than can be handled by the reactor site, thus creating a health and safety concern. In addition to this, the more tritium is produced. Chapter 5 of this thesis addresses this issue by studying the capability of a Proportional-Integral-Differential (PID) controller to manage the lithium-6, lithium-7 ratio, which can be used to stabilise tritium surplus inventory. The results clearly show that a simple controller is capable of managing the tritium production and surplus. However, calculations which include fuel cycle analysis needs to be included in the control theory model in order to fully determine the type of controller that is required.

CONTENTS

LIST OF FIGURES

LIST OF TABLES

Acknowledgements

Many thanks to my family, who have supported me in many ways and have put up with me talking about physics and maths during my 10 years at university.

I would like to express my sincere gratitude to Dr John Pasley for taking me on as PhD student, especially due to the circumstances by which this arrangement arose. I also appreciate that John was willing to supervise a project which is far from his core research area of ICF target physics. After only briefly meeting once in person with Wim Haeck (IRSN), he has kindly run 30-40 VESTA input files in over the last couple of years. These runs contributed to the multi-group reaction rate calculations in chapter 3 and the benchmarking in chapter 4. He has also been very helpful in debugging VESTA input files and providing extra valuable information regarding the simulations.

I would like to thank all of the neutronics team at CCFE, all of which have provided several nuggets of knowledge and information at some point during my PhD. Lee Packer was an excellent MSc supervisor and has continued to provide valuable support during the PhD. Jean-Christophe Sublet has provided a wealth of knowledge and experience in general, but has been particularly supportive and helpful in the multi-group optimisation work presented in chapter 3.

I would like to thank Prof Howard Wilson and all YPI academics for providing a great working environment for the post-grads at the YPI.

Last but certainly not least, this PhD could not have been completed without the sandwiches, baked potatoes, pastries and cakes provided by Browns of Heslington.

Author's Declaration

I declare that the work presented in this thesis, except where otherwise stated, is based on my own research and has not been submitted previously for a degree in this or any other university. Parts of the work presented in this thesis have been published in:

- L. Morgan, W. Haeck, L. Packer, J. Pasley. "The development of a fusion specific depletion interface code - FATI". Submitted to the Journal of Fusion Engineering & Design (In Press)
- L. Morgan, J-C Sublet, W. Haeck, J. Pasley. "Optimisation of energy binning structure for the Monte-Carlo modelling of fusion devices". Annals of Nuclear Energy, Volume 55, May 2013, Pages 108-115.
- L. Morgan & J. Pasley. "Tritium breeding control within liquid metal blankets". Fusion Engineering and Design, Volume 88, Issue 3, March 2013, Pages 107-112.
- L. Morgan & J. Pasley. "The impact of time-dependant spectra on fusion blanket burn-up". Fusion Engineering and Design, Volume 88, Issue 2, February 2013, Pages 100-105.

Name:

Signed:

Dedicated to the memory of my father, Glenn Morgan.

He was unceasingly kind and considerate.

Always provided logical, well considered advice.

He taught by example.

His energy resides in a dimension which is yet to be discovered.

CHAPTER 1

INTRODUCTION TO FUSION AND ICF

1.1 Fusion Reactions

Due to the extremely high temperature that is needed to induce fusion, only a small number of fusion reactions exist which can be exploited on earth. The following list contains some of the primary fusion reactions that occur within stars [1] :

$$
\begin{array}{lll}
D-D & {}^{2}_{1}H + {}^{2}_{1}H \rightarrow {}^{3}_{1}H + {}^{1}_{1}H + 4.0MeV & (50\%) \\
D-D & {}^{2}_{1}H + {}^{2}_{1}H \rightarrow {}^{3}_{1}He + n + 3.3MeV & (50\%) \\
D-T & {}^{2}_{1}H + {}^{3}_{1}H \rightarrow {}^{4}_{2}He + n + 17.6MeV & \\
He-D & {}^{3}_{2}He + {}^{2}_{1}H \rightarrow {}^{4}_{2}He + {}^{1}_{1}H + 18.3MeV & \\
T-P & {}^{3}_{1}H + {}^{1}_{1}H \rightarrow {}^{3}_{1}He + n - 0.764MeV & \\
\left({}^{3}He\right)^{2} & {}^{3}_{2}He + {}^{3}_{2}He \rightarrow {}^{4}_{1}He + 2{}^{1}_{1}H + 12.86MeV & \\
T-He & {}^{3}_{1}H + {}^{3}_{2}He \rightarrow {}^{4}_{2}He + {}^{2}_{1}H + 14.32MeV &
\end{array}
$$

Following the examination of the above reactions and cross-sections (see figure 1.1), the D-T reaction is the best candidate for fusion energy on earth due to its high cross-section at relatively low plasma temperatures. The high energy release, the availability of deuterium in seawater and the manufacturability of tritium are also positively contributing factors. D-^{3}He is also a promising reaction as its cross-section is relatively high at low-mid energy ranges and is more attractive than tritium as a fuel due to its stability. Using ^{3}He as a fuel would not require the fusion plant to have a tritium licence which is needed due to its beta radioactivity with a 12.5 year half life. However, ^{3}He is incredibly scarce on earth and unlike tritium, no economically viable method has been developed to artificially produce it. Current fusion experiments are fuelled by deuterium and tritium and it is highly likely that the first commercial fusion power plants will be also.

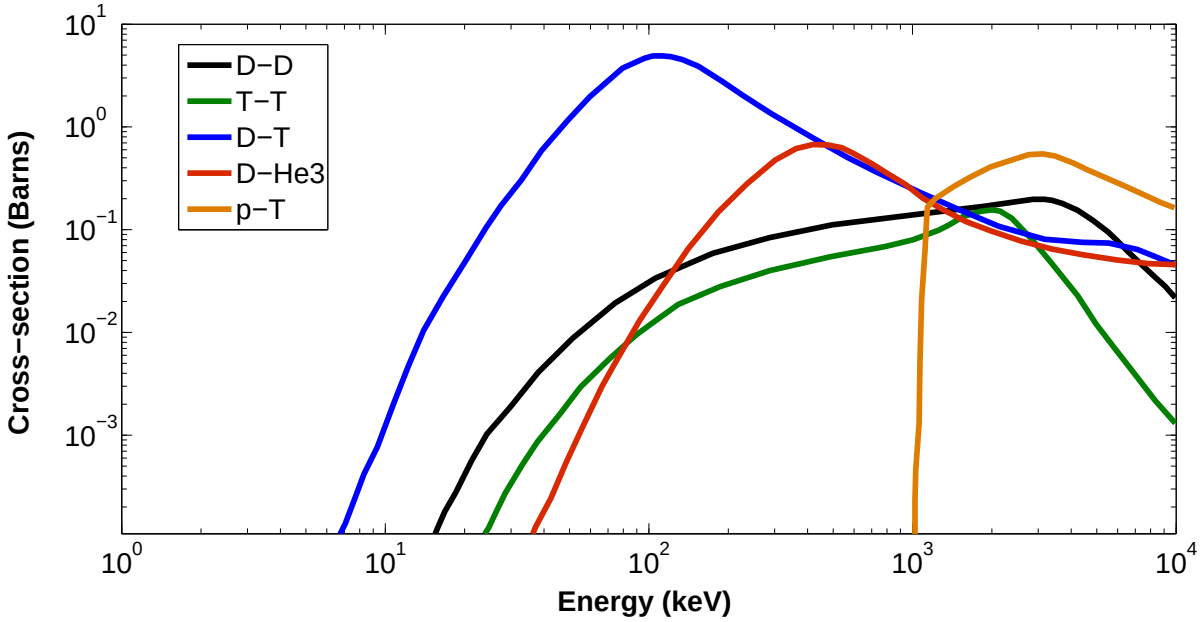

Figure 1.1: Fusion reaction cross-sections[1]

Unfortunately, tritium is rarely found in nature; and as a result of this, the production of tritium on-site, within a fusion device, is necessary for fusion power to be a credible solution to the world energy requirements. The world's entire civil tritium inventory [1] is estimated to be approximately 20kg [2] which is currently sourced from standard fission power plants via ^{10}B(n,T)^{4}He and ^{235}U fission reactions, costing \$200M/Kg, and CANDU reactors via the ^{2}H(n,g)^{3}H reaction, costing \$30M/Kg [3]. Tritium decays to helium-3 by beta emission with a half-life of approximately 12.5 years. As a result, the radioactivity of tritium has led to all tritium handling sites requiring a tritium licence which usually limits the amount of tritium that can be held on-site. A typical ICF reactor would have a refuelling rate of about 0.6Kg/day (assuming the same rate of tritium consumption as a MCF DEMO model) which is why ITER will be testing tritium blanket designs and a key requirement for DEMO is that it must be self-sufficient in tritium. This requirement is likely to apply to future ICF demonstration reactors. The most likely pathway to producing tritium on-site, the lithium blanket, is considered in detail in chapter 2. However, future fusion power plants need not necessarily be self-sufficient as alternative methods of tritium sourcing have also been studied, namely:

- Sourcing tritium from fission reactors [4, 5]
- Dedicated tritium producing reactors [6]

[1] This does not include the military inventory, which is classified.

Reaction	Energy released (MeV)	Energy released (MWh/g)
D-D	3.25	22
D-D	4.0	27
D-T	17.6	94
D -^{3}He	18.3	98

Table 1.1: The energy released from first order deuterium reactions[9]. Secondary reactions may also contribute significantly to the total energy released by the capsule.

The tritium inventory of a fusion power reactor is dependent on [7]:

- Plasma physics parameters
- Machine operation scenario
- The geometry and materials of the plasma facing components (PFC's)
- System integration choices

The second fuel, deuterium, accounts for 0.014% of all hydrogen contained in water [8], therefore the ocean provides a virtually inexhaustible supply of deuterium. In just one gallon of seawater, half a gram of deuterium can be extracted which has the energy equivalence of 300 gallons of petrol [9]. Table 1.1 shows some deuterium reactions and the energy released as a result of the reaction.

Currently, deuterium is produced in large hydrogen producing plants with techniques using electrolysis and distillation of liquid hydrogen [10], using well established pre-WWII technology.

1.2 Inertial Confinement Fusion

A number of fusion power technologies are currently being developed, with the most developed technologies being magnetic confinement fusion (MCF) and inertial confinement fusion (ICF). Other concepts such as the Z-pinch, bubble fusion, electrostatic confinement fusion (ECF), muon-catalysed fusion and reversed field pinch have been studied but are in the very early stages of development when compared to ICF and MCF. This thesis is concerned with the neutronics of inertial confinement fusion reactors; the following chapter will initially give an overview of ICF in general and will then go on to describe neutronics relevant concepts in greater detail.

The ICF method usually involves firing a particle beam (10's ns length), or more commonly a laser beam, at a fuel pellet of a few mm's diameter. The outer shell of the pellet, the ablator,

is heated to around 10 keV and rapidly expands radially outwards as a result of being heated by the laser. As a consequence of the conservation of momentum, the ablator applies a force to the fuel capsule that is directed radially inward; an action which is often compared to the rocket effect. This causes the pellet to implode, creating an extremely high density at the centre of the pellet for a very short time, which initiates a fusion burn throughout the pellet. Essentially, the modus operandi of ICF is the use of the inertia of the fuel mass to provide confinement [11].
The three most important conditions which need to be attained in order to achieve ignition are:

1. A temperature which results in a high fusion cross-section, which can initiate fusion burn. Once fusion burn has been initiated, the alpha particles released from the fusion reactions deposit their energy within the capsule, resulting in self / bootstrap heating.

2. The density-radius product of the hot fuel must be great enough to ensure that the alphas get absorbed within it. For DT: $\rho_{hs} r_{hs} > 0.3 g/cm^2$

3. The density-radius product of the whole capsule must be large enough so that ignition has time to occur and that the burn wave has time to traverse a significant portion of the fuel before the radially inwardly travelling rarefaction wave collides with it, so extinguishing the burn. (for DT: $\rho_F r_F > 3 g/cm^2$)

ICF and MCF operate within an order of magnitude in terms of temperature, however they differ significantly in terms of the density, pressure and confinement time of the plasma.

	T(keV)	n(cm^{-3})	P(bar)	τ_c
ICF	100	10^{26}	10^{12}	10^{-11}
MCF (DEMO)	10	10^{14}	10	$>10^5$

Table 1.2: Orders of magnitude of temperature, density, pressure and confinement time for ICF and MCF plasma states [12].

Unlike MCF which is likely to be steady state, ICF is a pulsed process which will operate at frequencies of 5 - 10 Hz (assuming a yield of around 500 MJ per pellet), in order to release enough energy to meet the requirements of a typical power plant.
Many designs, concepts and configurations have been tested for ICF target physics.
Direct/Indirect drive - Direct drive is the most conceptually simple of the laser driven ignition methods. The concept is based on the focussing a large number of high power lasers onto a small pellet containing fusionable materials, causing a shock wave to travel from the surface of the

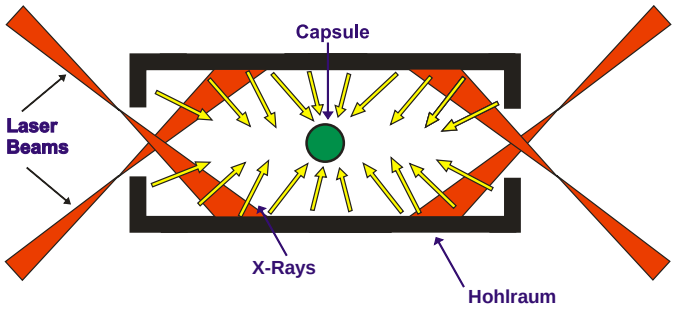

Figure 1.2: A schematic of the indirect drive configuration, consisting of a hohlraum, target capsule and laser light [13].

pellet to the centre, where all the shock waves constructively interfere. The merging set of shock waves can create the necessary conditions needed to induce fusion. Once fusion reactions have been initiated in the centre of the pellet, the heat generated by the fusion reactions creates a radially outward travelling burn wave that induces fusion reactions elsewhere in the pellet. The indirect drive method, shown in figure 1.2, was developed to improve the symmetry of the radiation incident on the target, thus reducing the magnitude of instabilities such as the Rayleigh - Taylor instability. The capsule is housed in a hohlraum which is heated by laser light entering from side entrance holes. The laser light causes the hohlraum, constructed with a high-Z material such as gold or lead, to heat up and emit x-rays. These x-rays then heat the capsule and cause the pellet to implode in the same manner as direct drive, however the x-ray radiation has greater isotropy when compared to direct laser beams.

Ion Driver - Ion driven ICF could potentially be used in commercial ICF power plants due to its ability to easily achieve a high repetition rate and its higher efficiency when compared to laser driven ICF. The ion energy is deposited in more spatially constrained region than with electromagnetic energy due to reflection playing no part in the physics of ion transport. Unlike, the transport of EM radiation through plasma, where the EM radiation can be reflected away from the pellet if the plasma density is above a specified threshold, the critical plasma density, for a particular plasma material. The function that describes the energy deposition per unit length, stopping power, is known as the Bragg curve; a generalised Bragg curve is shown in figure 1.3. It clearly shows that most of the ion energy is deposited at a distance which is slightly less than the stopping distance of an ion.

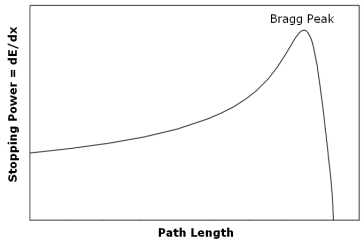

Figure 1.3: A typical Bragg curve showing the energy deposition per unit length of ionising radiation as it travels through matter

Fast Ignition - The fast ignitor concept [14, 15] is based on the separation of the compression and ignition phases. The two most developed methods of fast ignition are hole-boring and cone-guiding. The hole-boring method involves a high intensity laser pulse which bores through the ablated capsule material, followed by another pulse which is able to deposit its energy directly into the dense fuel, resulting in ignition. The cone-guiding method involves a capsule which is fabricated with a cone section bored out. After an initial laser pulse which initiates a plasma shock wave, the engineered access cone allows a second laser pulse or proton beam to deposit its energy directly into the dense fuel, resulting in ignition.

The target physics could be considered to be be far removed from the subject of neutronics; However, the target physics will have important implications on blanket design. For instance: indirect drive will result in an increased x-ray flux on the first wall, but will also require fewer laser entry holes into the fusion chamber when compared to direct drive, and fast ignition may require additional laser entry holes through the blanket due to a greater number of drivers.

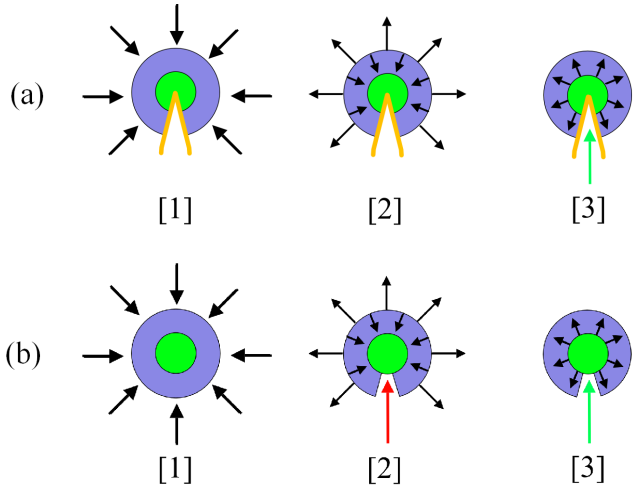

Figure 1.4: Fast ignition: **a)** Cone guided **b)** Hole boring

The ultimate goal of fusion is to produce electricity to be supplied to the grid. In order to do this, the energy supplied to a fusion reactor must enable the "production" of energy which is a factor of

at least 15 larger than the input in order to ensure the fusion power plant is economically viable. The requirement of a large energy yield from each fuel pellet lies at the heart of an economical and scalable fusion power plant.

For two fuels with number densities, N_D and N_T , averaged reaction rate density, R, is defined as

$$R =< \sigma\, v > N_1 N_2 =< \sigma\, v > N_0^2/4 \tag{1.1}$$

Assuming $N_D + N_T = N_{0.}$ and $N_D = N_T$, the energy released, E_{out}, by burning all of the fuel is

$$E_{out} = R\, V\, \tau\, Q \tag{1.2}$$

where Q is the energy released by each fusion reaction, V is the volume of the fuel and τ is the confinement time. After ignition, the fusion events will continue to occur until the radially inward travelling rarefaction wave disassembles the capsule, resulting in the destruction of the outwardly travelling fusion burn wave. Assuming that the fusion ignition and the rarefaction wave initiate at the same time, the confinement time can be calculated. The time, t, taken for the rarefaction wave to arrive at a radial position, r, is simply $t = {}^{(r-r')}/_{c_s}$. Thus, the mean burn time given by

$$\bar{t} = \frac{3}{4\pi r^3 \rho c_s} \int_0^r \frac{(r - r')}{c_s} 4\pi\rho r'^2 dr' = \frac{r}{4c_s} \tag{1.3}$$

Substituting this mean burn time into equation 1.2, the energy released from the capsule is given by

$$E_{out} = \frac{< \sigma\, v > \pi\, r^4 N_0^2\, Q}{12 c_s}$$

This roughly approximates to an E_{out}, or fusion yield, in the order of 100's MJ.

The total number density is given by $2N_D$, since $N_0 = N_D + N_T$ and $N_D = N_T$. Therefore, equation 1.1 becomes:

$$R = \frac{1}{2}\frac{dN}{dt} = - < \sigma\, v > \frac{N^2}{4} \tag{1.4}$$

Integrating between the confinement time, t_c, and zero gives:

$$\frac{1}{N} - \frac{1}{N_0} = \frac{t_c}{2} < \sigma\, v > \tag{1.5}$$

where N_0 is the initial number density. Equation 1.2 assumes that 100% of the fuel within the capsule is burned, which is unrealistic. In order to compensate for this a burn fraction can be defined:

$$f_b = \frac{N_0 - N}{N_0} \tag{1.6}$$

Substituting equations 1.4, 1.5 and $N_0 = \frac{\rho}{m_{DT}}$ into 1.6 gives [16]

$$f_b = \frac{\rho r}{\rho r + \beta}$$

where the burn parameter is defined as $\beta = (8 m_{DT} C_S) \,/\, (< \sigma\, v >)$ which corresponds to a value of $6 - 9 g/cm^2$ for DT at 30keV, and ρr is the density radius product of the fuel. This implies that the initial ρr must be at least $3 g/cm^2$ in order to achieve an efficient fusion burn ($f_B \sim 0.3$).

The heat energy, E_H, required to raise the capsule to a temperature, T, which initiates fusion burn is

$$E_H = N_0\, V\, 3 k_B\, T = \left(\frac{\rho N_A}{A}\right) \left(\frac{4\pi r^3}{3}\right) 3\, k_B\, T$$

where T is the temperature of the fuel, A is the molecular mass and k_B is the Boltzmann constant. However, taking into account the burn-fraction ($f_B \sim 0.3$) and the beam-fuel coupling efficiency ($\eta_{bf} \sim 0.01$) and the efficiency of the driver($\eta_d \sim 0.01 - 0.3$), results in a significant increase in the energy required to heat the fuel, E_{in} such that it will ignite.

$$E_{in} = \eta_{bf} \eta_d\, E_H \sim 10\, MJ$$

1.3 Neutron spectrum

The ICF simulated neutron spectrum shown in figure 1.5 broadly illustrates the physical processes which form the spectrum. This section on fusion neutronics develops the physical models which are important to neutron interactions within an ICF target during thermonuclear fusion and within the fusion blanket.

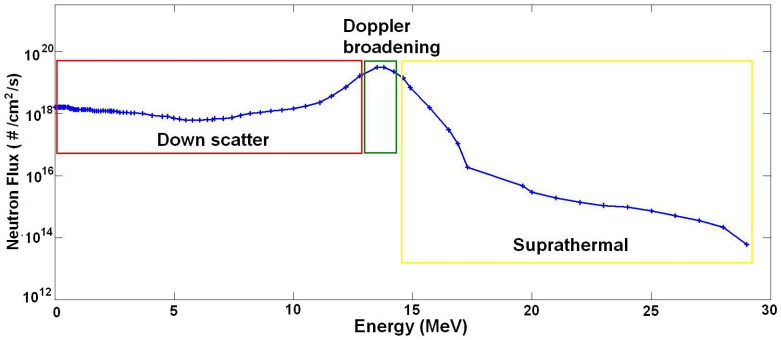

Figure 1.5: Simulated neutron spectra [17].

The type of confinement used to induce fusion reactions will leave a signature in the neutron spectrum. Both MCF and ICF neutron spectra are Doppler broadened as a result of the hot plasma, however, the ICF spectra is dominated by down-scattered and suprathermal neutrons which are not found in MCF spectra.

The term "suprathermal neutron" generally refers to a neutron which is observed to have a kinetic energy which is above the Q-value of the fusion reaction from which it originated. However, a neutron distribution containing supra-thermals can be more formally defined by having a broader high-energy tail than would be expected for a thermal distribution. Neutrons of this type are produced as a result of fusion reactions in which one or both of the fusing nuclei have an energy which is significantly above the thermal average. Prior to the fusion event, the fusing nuclei can gain energy via elastic scattering with neutrons or via large angle coulomb scattering with alpha particles, where both alpha and neutrons have been produced as a result of fusion. The suprathermal neutrons are born as a result of in "in-flight" reaction, where it gains energy from the Q value of the fusion reaction plus impartation of kinetic energy from the high energy scattered nuclei. The energy and probability of occurrence of the suprathermal neutrons can be deduced from the consideration of the scattering kinematics.

Assumptions:

- Kinematics as illustrated in figure 1.6.
- Elastic scattering - this is the dominant scattering process with light nuclei.
- $V_{f,CoM} = 0$ which is a reasonable assumption based on the fact that $1/2 m_n v_{i,Lab}^2 \gg k_B T_{D,T} \Rightarrow v_{i,Lab} \gg V_{i,Lab}$.

Considering the conservation of momentum in the lab system, the velocity of the compound

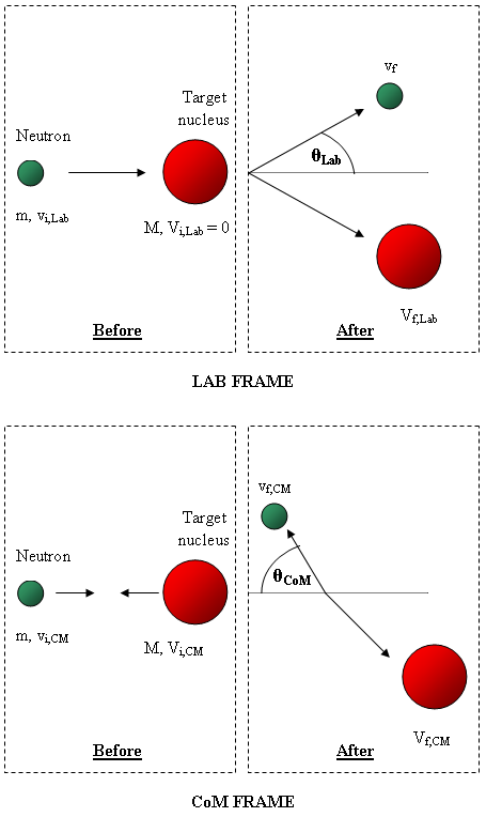

Figure 1.6: Neutron scatter in center of mass (CoM) and Laboratory (Lab) frames of reference.

Symbol	Description
$V_{i,CoM}$	Initial velocity of nucleus in CoM frame
$V_{f,CoM}$	Final velocity of nucleus in CoM frame
$v_{i,CoM}$	Initial velocity of neutron in CoM frame
$v_{f,CoM}$	Final velocity of neutron in CoM frame
V_{CoM}	Velocity of CoM
$V_{f,Lab}$	Final velocity of nucleus in Lab frame
$v_{i,Lab}$	Initial velocity of neutron in Lab frame
$v_{f,Lab}$	Final velocity of neutron in Lab frame
$v_{C,Lab}$	Velocity of compound nucleus
θ_{Lab}	Neutron scattering in angle in Lab frame
θ_{CoM}	Neutron scattering angle in CoM frame
m_A	Mass of nucleus
m_n	Mass of neutron
A	$M_{nucleus}/M_{neutron}$

Table 1.3: Variables and their descriptions used in the neutron kinematic derivations

nuclues after the collision is given by

$$v_{f,CoM} = \frac{V_{i,Lab}^2}{1+A}$$

The kineitic energy in the lab frame is therefore

$$E_{CoM} = (v_{i,Lab} - v_{c,CoM})^2 - A v_{f,CoM}^2 \tag{1.7}$$

Considering the conservation of momentum in the centre of mass system, the velocity of the incident neutron is given by

$$(v_{i,Lab} - v_{f,coM})(m_n + m_A) = m_n v_{i,Lab} \tag{1.8}$$

Substituting 1.8 into 1.7,the conservation of energy takes the form [18, 19]

$$\frac{A v_{i,CoM}^2}{2(1+A)} = \frac{A V_{f,CoM}^2}{2} + \frac{v_{f,CoM}^2}{2} \tag{1.9}$$

Considering the conservation momentum in the centre of mass frame

$$m_n v_{f,CoM} = M V_{f,CoM} \Longrightarrow v_{f,CoM} = A V_{f,CoM}$$

which, when substituted into equation 1.9 results in

$$\frac{A V_{CoM}^2}{2(1+A)} = \frac{A V_{f,CoM}^2}{2} + \frac{A^2 V_{f,CoM}^2}{2}$$

which reduces to

$$V_{f,CoM} = \frac{V_{CoM}^2}{1+A} \qquad v_{f,CoM} = \frac{A V_{CoM}^2}{1+A} \tag{1.10}$$

Conservation of momentum in the CoM frame also reveals that

$$m_n v_{i,CoM} = (M+1) V_{CoM} \Longrightarrow V_{CoM} = \frac{v_{i,CoM}}{A+1} \tag{1.11}$$

The analysis of the kinematics in the centre of mass frame (or laboratory frame) alone cannot extricate a simple relation between $v_{i,coM}$ ($v_{i,Lab}$) , $v_{f,CoM}$ ($v_{f,Lab}$) and $\theta_{Com/Lab}$ which is required. In addition to this, the frame of primary interest is the laboratory one, as this is the frame in

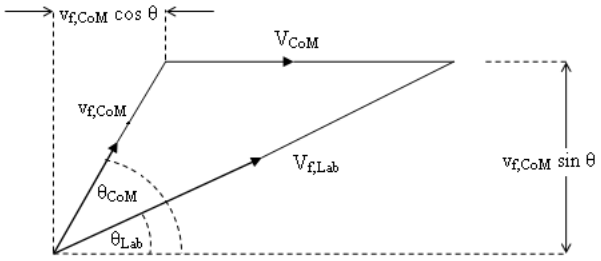

Figure 1.7: Trigonometric relation between the scattering angles in the CoM and Lab frames of reference.

which measurements are made and the analytical kinematics can be validated. As a result, attention is now given to the trigonometry that links the two frames of reference.
The relation between the CoM and Lab velocities is illustrated in figure 1.7, which mathematically translates to

$$v_{f,Lab}^2 = \left(v_{f,CoM}\, sin\theta_{CoM}\right)^2 + \left(v_{f,CoM}\, cos\theta_{CoM} + V_{CoM}\right)^2 \tag{1.12}$$

Substituting equations 1.10 and 1.11 into equation 1.12 results in:

$$v_{f,Lab}^2 = \left(\frac{A\, v_{i,Lab}^2}{1+A}\, sin\theta_{CoM}\right)^2 + \left(\frac{A\, v_{i,Lab}^2}{1+A}\, cos\theta_{CoM} + \frac{v_{i,Lab}}{1+A}\right)^2$$

which simplifies to

$$v_{f,Lab}^2 = \left(\frac{A^2 + 2A\, cos\theta_{CoM} + 1}{(1+A)^2}\right) v_{i,Lab}^2 \tag{1.13}$$

This result can now be used to calculate the ratio of the neutron kinetic energy before to that after the scattering collision as a function of the scattering angle.

$$\frac{E}{E_0} = \frac{\frac{1}{2} m_n v_{f,Lab}^2}{\frac{1}{2} m_n v_{i,Lab}^2} = \frac{A^2 + 2A\, cos\theta + 1}{(1+A)^2} = \left[\frac{(1+\alpha) + (1-\alpha)\, cos\theta}{2}\right]$$

The maximum, minimum and average kinetic energy of the neutron, once the scattering collision has occurred, is:

$$E_{max} = \frac{A^2 + 2A\, cos\, 0 + 1}{(1+A)^2} E_0 = \frac{(1+A)^2}{(1+A)^2} E_0 = E_0$$

$$E_{min} = \frac{A^2 + 2A\, cos\pi + 1}{(1+A)^2} E_0 = \frac{(1-A)^2}{(1+A)^2} E_0 = \alpha E_0$$

$$E_{av} = \frac{1}{2\pi}\int \frac{(1+\alpha)+(1-\alpha)\,cos\theta}{2} d\theta = \frac{(1-A)^2}{(1+A)^2}E_0 = \left(\frac{1+\alpha}{2}\right)E_0$$

The maximum energy of the post-collision neutron, as a result of a zero scattering angle, is equal to the energy of the neutron before the collision. This is essentially a non-collision, as no energy or momentum is exchanged between the neutron and the target nucleus. The minimum energy of a post-collision neutron occurs when the scattering angle is 180°, which is a complete recoil. The energy lost by the neutron in the scattering reaction is transferred to the target nucleus. In the ICF pellet, this translates to the heating of a fraction of the deuterium and tritium nuclei to a temperature which is significantly above the background average temperature. The D and T ions typically gain energy in the order of MeV from a scattering reaction, while their background temperature is in the order of 10-100 KeV. The neutron-nucleus kinematics analysis used above applies similarly to the heating of D and T atom via collisions with alpha particles released from the fusion reaction. Once the D and T nuclei have gained energy from a scattering reaction, the likelihood of the nuclei undergoing a fusion reaction decreases due to the 1/v nature of the cross-section. However, the extremely high density found in the ICF pellet ensures that high energy fusion reactions take place. In these fusion reactions, the neutrons released gain around 14.1MeV from the loss of binding energy and also gain kinetic energy from the parent nuclide, producing suprathermal neutrons. The resultant energy of the suprathermal neutrons and alphas can be calculated using the same methodology as the scattering analysis, however kinetic energy is not conserved in this case. The energy balance equation for a fusion reaction is

$$\frac{1}{2}m_n v_n^2 + \frac{1}{2}m_\alpha v_\alpha^2 = Q + \frac{1}{2}m_D v_D^2 + \frac{1}{2}m_T v_T^2$$

which is often approximated as

$$\frac{1}{2}m_n v_n^2 + \frac{1}{2}m_\alpha v_\alpha^2 \approx Q \qquad Q \gg v_T,\, v_D$$

This approximation is valid for MCF neutrons and the majority of ICF neutrons, however the small number of suprathermal neutrons produced has an impact on transmutation and damage of structural materials within the IFE reactor, hence the probability of their production and the energy dependence is of importance.

The primary reactions are thermonuclear reactions [20]

- $\boldsymbol{D_{slow} + T_{slow} \rightarrow n}\,(14.05\,MeV) + \boldsymbol{\alpha}\,(3.53\,MeV)$
- $\boldsymbol{D_{slow} + D_{slow} \rightarrow} P(3.02MeV) + T(1.01MeV)$ [50%]
- $\boldsymbol{D_{slow} + D_{slow} \rightarrow n}\,(2.45\,MeV) + \boldsymbol{^3He}\,(0.82MeV)$ [50%]
- $\boldsymbol{T_{slow} + T_{slow} \rightarrow \alpha}\,(0 - 3.9\,MeV) + \boldsymbol{2n}\,(0 - 9.4\,MeV)$

Neutron interactions such as elastic scattering, (n, n'), and multiplication, (n, xn), account for the large amount of neutrons which lie in the range 0-14.MeV

- $\boldsymbol{D_{slow} + n \rightarrow D' + n'}$
- $\boldsymbol{T_{slow} + n \rightarrow T' + n'}$
- $\boldsymbol{D + n \rightarrow P' + 2n}$
- $\boldsymbol{T + n \rightarrow D' + 2n}$

where D', n', P' and T' are scattered deuterons, neutrons, protons and tritons respectively. The helium nuclei produced as a result of fusion impart energy on D and T nuclei via coulomb scattering

- $\boldsymbol{D_{slow} + \alpha \rightarrow D' + \alpha'}$
- $\boldsymbol{T_{slow} + \alpha \rightarrow T' + \alpha'}$

Following the initial thermonuclear reactions and secondary scattering reaction, tertiary fusion reactions can take place which produce suprathermal neutrons.

- $\boldsymbol{D_{slow} + T' \rightarrow \alpha' + n'}\,(9.2 - 28.2\,MeV)$
- $\boldsymbol{T_{slow} + D' \rightarrow \alpha' + n'}\,(12 - 30.1\,MeV)$
- $\boldsymbol{D' + D_{slow} \rightarrow P + T}$ [50%]
- $\boldsymbol{D' + D_{slow} \rightarrow n}\,(2 - 15.4\,MeV) + \boldsymbol{^3He}\,(0.82MeV)$ [50%]

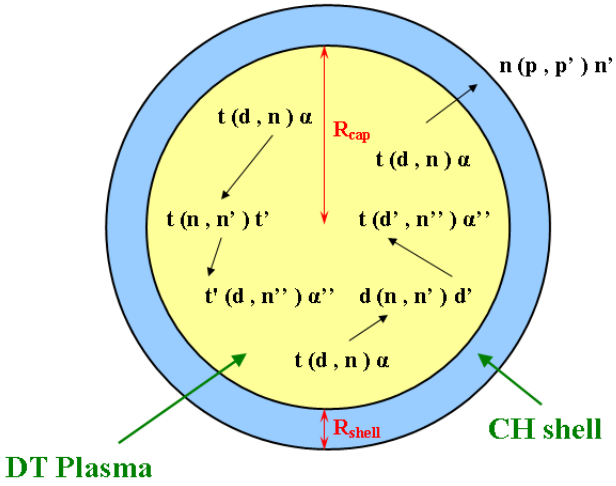

Figure 1.8: A schematic of some primary, secondary and tertiary reaction within the ICF capsule.

Many ICF capsules are coated with a polymer (CH) ablator, which aids in the compression of the DT fuel. Protons, within hydrogen, found in the ablator can undergo a scattering reaction with a fusion neutron resulting in the release of a fast proton.

- $\boldsymbol{n + p \rightarrow n' + p'}$

The yield of the primary and suprathermal neutrons can be evaluated analytically given the assumption that all of the primary fusion events occur in an infinitesimally small point at the center of the capsule (hot spot model)[21].

The yield of suprathermal neutrons that have been created via a deuterium scatter is given by

$$Y_d = \int_0^{R_{cap}} \sigma_d \phi \, n_d \, dr$$

where σ_d is the neutron scattering cross-section of deuterium, ϕ is the fusion primary neutron flux, n_d is the deuterium number density and R_{cap} is the radius of the DT capsule. The fusion primary neutron flux is related to the primary yield, Y_P, via

$$\phi = \frac{Y_P}{unit\ volume} = \frac{Y_P \rho_{cap}}{m_{AMU}\,(2N_d + 3N_t)}$$

where m_{AMU} is the atomic mass unit. Hence the yield of suprathermal neutrons which have been created via a deuterium scatter is

$$Y_d = \frac{Y_P \sigma_d \, N_d}{m_p \, (2N_d + 3N_t)} \rho_{cap} \, R_{cap}$$

An equivalent analysis can be implemented to derive the yield of suprathermal neutrons which have been created via a tritium scatter. The total suprathermal neutron yield is given by:

$$Y_{supra} = Y_d + Y_t = \left[\frac{Y_P \sigma_d \, n_d}{m_p \, (2N_d + 3N_t)} + \frac{Y_t \sigma_t \, n_t}{m_p \, (2N_d + 3N_t)} \right] \rho_{cap} \, R_{cap}$$

Hence the ratio of the primary to suprathermal yield is

$$\frac{Y_{supra}}{Y_P} = \frac{\gamma \sigma_d + \sigma_t}{m_p \, (2\gamma + 3)} \rho_{cap} \, R_{cap}$$

where $\gamma = N_d / N_t$. The hot proton yield ratio, Y_{proton}, produced via n-p scatter, to the initial neutron yield can be calculated in a similar manner.

$$Y_{proton} = \int_0^{R_{shell}} \sigma_p \phi \, N_p \, dr \tag{1.14}$$

where σ_p is the neutron scattering cross-section of hydrogen. Defining the initial neutron flux as

$$\phi = \frac{Y_P}{unit \; volume} = \frac{Y_P \rho_{shell}}{m_p \, (n_p + 12N_c)} \tag{1.15}$$

where N_c is the carbon and hydrogen number density in the CH ablator. Substituting equation 1.15 back into equation 1.14 and defining $\beta = n_p / n_c$ gives

$$\frac{Y_{supra}}{Y_P} = \frac{\gamma \sigma_p}{m_p \, (\gamma + 12)} \rho_{shell} \, R_{shell}$$

1.3.1 Downscatter

A significant number of neutrons are observed at energies which are significantly below the fusion energy threshold at which the neutrons would have been created. These neutrons have lost energy as a result of colliding with background nuclei within the plasma. The neutron undergoes an elastic scattering with a deuterium or tritium ion, losing a fraction of its energy in the process, while the ion gains energy and can then go on to fuse with another ion and create suprathermal

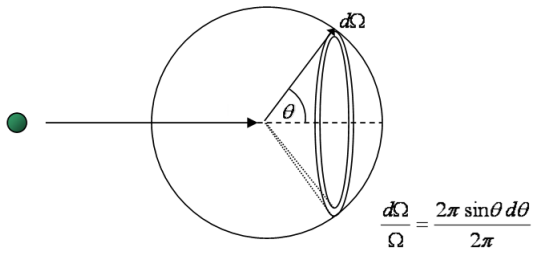

Figure 1.9: Scattering in CoM frame with reference to the solid angle, $d\Omega$, subtended by an angle, θ.

neutrons. After undergoing a scattering reaction the neutron, with its reduced energy, may undergo another scattering reaction within the burning capsule, losing more of its energy. An average loss of energy can be defined for each collision, which leads to the multi-scattered neutron energy having a logarithmic relation with the initial energy. The lethargy of a neutron is used to define the relative energy of the incident and scattered neutron.

Lethargy is defined as [19]

$$u = ln\left(\frac{E_0}{E}\right)$$

where E_0 is the maximum energy a neutron can acquire, which is most often the energy of the neutron at its source. The mean lethargy gain per collision, ξ, is defined as:

$$\xi =< u >= ln\left(\frac{E_0}{\overline{E}}\right) \tag{1.16}$$

The relation between the initial and final neutron velocity after a scattering collision is given in equation 1.13, which can then be substituted into equation 1.16

$$\xi = ln\left(\frac{E_0}{\overline{E}}\right) = ln\left(\frac{A^2 - 2Acos\theta + 1}{(1+A)^2}\right) \tag{1.17}$$

In order to calculate the lethargy gain per collision, the lethargy must be integrated over the solid angle subtended by an incident neutron (as shown in figure 1.9)

$$\frac{dn}{n} = \frac{sin\theta d\theta}{2} \tag{1.18}$$

Integrating equation 1.17 with respect to dn, as defined in 1.18, gives

$$\int \xi dn = ln\left(\frac{A^2 - 2A\,cos\theta + 1}{(1+A)^2}\right)\frac{n\,sin\theta\,d\theta}{2}$$

	<A>	α	ξ	$< \# > (E_0 \rightarrow E_{thermal})$
H	1	0	1	17
D	2	0.111	0.725	23
T	3	0.25	0.538	31
C	12	0.716	0.158	106
Li	6	0.510	0.299	55
Au	197	0.98	0.01	1668
Be	9	0.64	0.207	80

Table 1.4: Slowing down parameters of common fusion materials

Integration via the following substitution and appropriate change of limits

$$x = \frac{A^2 - 2A\,cos\theta + 1}{(1+A)^2} \implies dx = \frac{2A\,sin\theta\,d\theta}{(A+1)^2}$$

$$x(\theta = \pi) = \alpha \qquad x(\theta = 0) = 1$$

results in the equation taking the form

$$\xi = \frac{(A+1)^2}{4A} \int ln(x)dx \tag{1.19}$$

The coefficient of the integral can be simplified by introducing the α ratio

$$\frac{(A+1)^2}{4A} = \frac{(A+1)^2}{(A+1)^2 - (A-1)^2} = \frac{(A+1)^2}{(A+1)^2 - \frac{(A-1)^2}{(A+1)^2}} = \frac{1}{1-\alpha}$$

Thus, equation 1.19 becomes

$$\xi = \frac{(A+1)^2}{4A} \int ln(x)dx = 1 + \frac{\alpha}{1-\alpha} ln\,(\alpha)$$

This states that the lethargy gain per collision is not dependant on the initial neutron energy, rather it is only dependant on the mass of the target nucleus.

The average number of collisions (or mean free paths MFP's), <#>, that a neutron will undergo in order to be down scattered from an energy, E_0, to energy, E, is given by:

$$< \# > (E_0 \rightarrow E) = \frac{ln\left(\frac{E_0}{E}\right)}{\xi}$$

Thus, the average number of collisions a 14MeV neutron will undergo to be down-scattered to

thermal speed is 40-50 assuming a 50:50 ratio of D and T.

1.3.2 Doppler broadening

The phenomenon that is Doppler broadening, or more specifically thermal Doppler broadening in the case of neutronics, is attributed to the widening of resonance peaks. The widening of the velocity/energy peaks is a result of the neutron being emitted while the parent nucleus is in motion. Hence, the velocity of the ejected neutron is relative to the velocity of the parent nuclide. Thus, a neutron ejected from stationary nuclie undergoing fusion will emerge from the reaction at an exact energy which is defined by the particular reaction. Conversely, a high speed, in-flight fusion reaction will eject a neutron, not at a particular energy, but instead with an energy which is defined by a Gaussian probability density function. The energy spectrum of a Doppler broadened line, initially centered at E_0, will always be symmetric Gaussian shaped profile with a width, Δ, proportional to the temperature of the plasma [22].

$$\Delta = \sqrt{\frac{4E_0 k_B T}{A}}$$

For IFE applications, Doppler broadening has a less significant effect on the shape of the spectrum than to supra-thermalisation (ST) and down-scatter (DS). The effect of Doppler broadening is more evident in MFE neutron spectra where other physical phenomena such as ST and DS are practically non-existant. However, Doppler broadening has only a slight effect on ICF and MFE spectra due to the temperature of the plasma (∼10's KeV), in both cases, being significantly less than the energy of the fusion neutron (∼MeV).

In addition to the effect of Doppler broadening within plasma, the Doppler effect broadens the cross-sections of neutron reactions at low energies. Once the neutrons have been down-scattered to eV energies within the fusion blanket, they will be of a speed which is comparable to the thermal speeds of the atoms within the structural materials. The cross-sections of the structural materials have been calculated based on a stationary target. Hence, if the neutron energy is in the eV range and the structural materials within the blanket are hot, the atoms and the nuclides will be travelling at similar speeds but with different velocities. The cross-section is dependant on the superposition of the velocity of the atoms and the nuclide, hence the reaction speed will equal the neutron speed plus/minus the thermal speed of the nuclide [23].

$$\overline{\sigma}(v,T) = \frac{1}{\sqrt{\pi} v_{th}^2 v} \int dv_r v^2 \sigma(v_r) \left[exp\left(-\frac{(v-v_r)^2}{2v_{th}^2} \right) - exp\left(-\frac{(v+v_r)^2}{2v_{th}^2} \right) \right] \tag{1.20}$$

Doppler broadening is most prominent in reactions with strong resonance regions such as Ni-58 (n,γ), Cr-52 (n,γ), W-186 (n,γ), Fe-56 (n, n') and O-16 (n,α).

1.4 Summary

This chapter introduced the physics of fusion, with a bias towards inertial confinement. A summary of potential fusion reactions, which could be exploited for the production of electricity, were discussed and the tritium sourcing options were outlined. A description of the fuels, and their availability, required for fusion were discussed. The sourcing of tritium via lithium blankets placed around the fusion reactor is, by far, the leading technology for meeting the tritium requirements of a fusion reactor. The three most important conditions required for ICF ignition are: high gain burn ($\rho_F r_F > 3g/cm^2$) , ignition ($\rho_C r_C > 0.3g/cm^2$) and temperature ($T \approx 100\,keV$). Target methods used to meet these requirements fall into the categories of direct or indirect fusion.

The overall theme of this thesis is the study of tritium production for ICF reactors. Thus, the target methods described will have an effect on the blanket in ways such as the number of ports and the protection used to maintain blanket longevity. The final part of this section described the kinematics of the neutron transport within the fusion pellet and the effect it has on the emitted particle spectrum. The particle spectrum can also introduce subtle effects to the blanket, especially the first wall.

The next chapter describes the physics and technology of fusion blankets. Within the blanket, high energy neutrons released from the fusion capsule are absorbed, which heats the circulating coolant, and also reacts with lithium and neutron multipliers in order to produce tritium. This chapter will also introduce some IFE reactor conceptual designs, their functionality and their decommissioning attributes.

CHAPTER 2

FUSION TECHNOLOGY

In this chapter, the theory of fusion reactor physics is addressed, which mainly consists of the theory of tritium production, blankets technologies and the generation of nuclear waste. The theory behind blanket technologies is first introduced in a qualitative manner, which is then followed by a mathematical treatment of neutron transport and nuclide transmutation later in the chapter.

The blanket is a component that surrounds the fusion reactor. The main functions of a blanket are:

- **Tritium Production** – The primary material in the blanket is lithium which is used to create tritium via the ${}^{6}Li(n,\alpha)^{3}H$ and ${}^{7}Li(n,n'\alpha)^{3}H$ reactions. Depending on the blanket technology, the tritium is either purged by a fluid (such as helium or water) or is carried away in a liquid lithium (or lithium compound/mixture) flow.
- **Heat Extraction** – The energetic neutrons released from the fusion reaction are moderated and eventually absorbed in the blanket. Kinetic energy is transferred from the neutron to the blanket coolant, which is then used to indirectly drive a turbine for electricity production.
- **Radiation Shielding** – The neutron flux produced in the plasma would result in a lethal neutron dose to the fusion reactor workers if shielding was not present. The lithium blanket indirectly acts as a neutron shield to protect fusion reactor staff, although additional radiation shields are also required.
- **Waste Transmutation** - A blanket containing fissile/fissionable waste could be irradiated by fusion neutrons, initiating fission events. These fission reactions, which are to be kept sub-critical, can burn long-lived actinides and fission products, reducing the amount of spent nuclear fuel which is to be sent for long term storage in a geological repository. In

addition to this, a fission blanket can significantly increase the energy yield of a fusion power plant and places less stringent requirements on the capsule gain than a pure ICF reactor.

2.1 Tritium Breeding

The most promising tritium breeding concept is a lithium containing blanket that surrounds the plasma. Lithium 6 & 7 produce tritium via the ^{6}Li(n,α)T and ^{7}Li(n,n'α)T reactions. However, the lithium-6 reaction is the most dominant due to its higher cross-section at low neutron energies (Fig. 2.1).

The two main naturally occurring isotopes of lithium are ^{6}Li and ^{7}Li, the abundances of which are 7.7% and 92.2% respectively. In many applications it is desirable for the ^{6}Li to be enriched as its cross-section is several orders of magnitude higher than that of ^{7}Li. In addition to this, $^{6}Li(n,\alpha)$ is an exothermic reaction whereas the ^{7}Li reaction is endothermic (hence, a threshold reaction), hence the ^{6}Li reaction produces more tritium per neutron. Although lithium is the most dominant tritium producer, other pathways exist which contribute a relatively low yet significant fraction. One example of tritium pathways is shown in table 2.1 (from a recent HCPB (helium cooled pebble bed) DEMO study [24]) and in fig 2.2.

Pathway	Tritium Contribution	Contribution
^{6}Li(n,α) ^{3}H	64.606 %	87.03%
^{6}Li(n,α) H(β-)^{3}He(n,p)^{3}H	22.424 %	
^{7}Li$(n,t\alpha)$ ^{3}H	2.054 %	12.97%
^{9}Be$(n,t\alpha)$ ^{3}H	2.378 %	
^{9}Be(n,α) ^{6}He(β-)^{6}Li(n,α) ^{3}H	6.179 %	
^{9}Be$(n,t\alpha)$ ^{3}H(β-)^{3}He(n,p) ^{3}H	0.582 %	
^{9}Be(n,α) ^{3}He(β-)^{6}Li(n,α) ^{3}H (β-)^{3}He(n,p)^{3}H	1.042 %	

Table 2.1: Tritium pathways for a helium cooled pebble bed DEMO model [24]. Reactions are defined as $Nuclide_{Parent}(Particle_{Incident},\ Particles_{Ejected})Nuclide_{Daughter}$

The tritium breeding ratio (TBR) is used to define the rate at which tritium is being created, N_{+}, to the rate at which it is being burned, N_{-} .

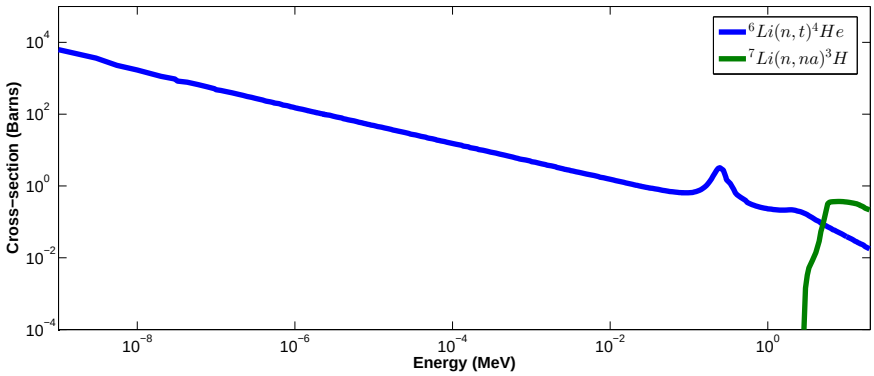

Figure 2.1: Tritium producing cross-sections of the two most abundant isotopes of lithium.

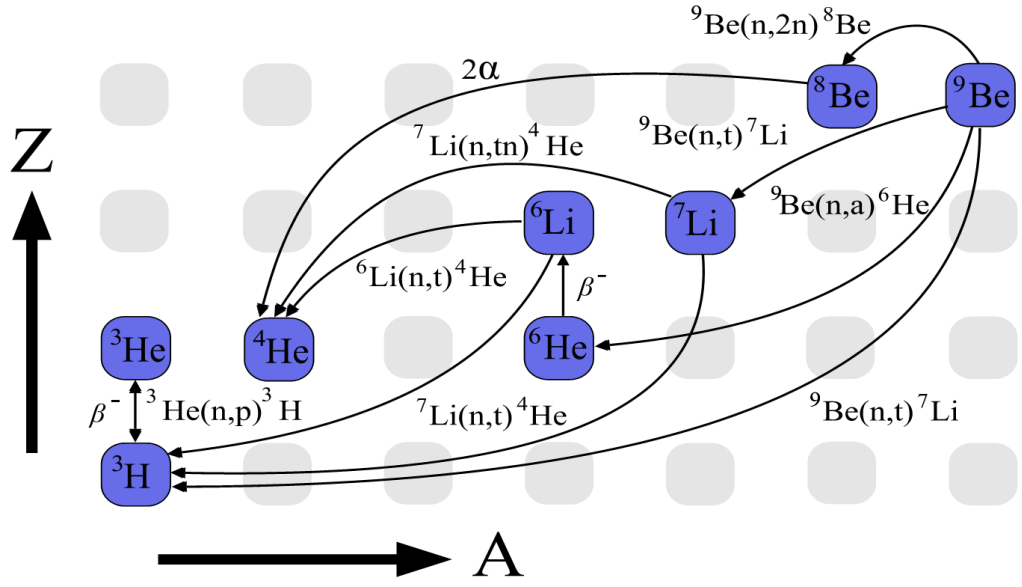

Figure 2.2: Dominant absorption and decay pathways for a HCPB blanket.

$$TBR = N_+/N_-$$

Hence, by definition, a TBR of unity is required in order to sustain tritium self-sufficiency within the fusion reactor. In reality, the TBR must be greater than unity, due to losses in the system.

$$TBR \geqslant 1 + M$$

An MCF conceptual design study [25] finds that $M \sim 0.1$. The excess breeding margin, M, can be divided into three main categories [26]:

1. Tritium required to provide the start-up inventory for a new fusion power plant:

   a. T build-up in the power core materials (especially in the breeder, multiplier, structural materials) and the T recovery systems for the blanket.

   b. T build-up in the fuel reprocessing system (especially in the cryopanels, getters, molecular sieves).

   c. T build-up in the de-tritation systems for coolants, building atmosphere, and vacuum pumping system.

   d. T to be stored in getters as reserve to continue plasma operation in case of temporary malfunctions of the T reprocessing system.

2. Tritium necessary to compensate for the decay of the total T inventory.

3. T lost to the environment (atmosphere, cooling water etc), F_{env}. This is expected to be 10 Ci/day which is negligible when compared to other sources and sinks and corresponds to approximately 1g of tritium per 1000 days of operation [30].

The findings of [25] are likely to be broadly applicable to ICF reactors, although the solid nature of ICF pellets is likely to result in less leakage build-up in structural materials due to the relatively simple ICF reactor structure when compared to the tokamak and associated equipment.
The net rate of tritium production, F_{net}, in terms of all of the sources and sinks in the fuel cycle is [27]:

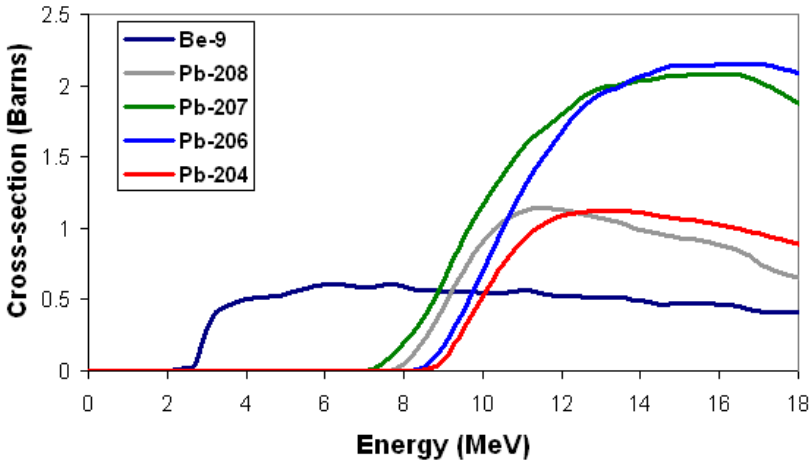

Figure 2.3: (n,2n) cross-sections for beryllium and lead.

$$F_{net} = \bar{F}_{bred} - \bar{F}_{fus} + \bar{F}^{in}_{ext} - \bar{F}^{in}_{out} - \bar{F}_{env}$$

Where F_{bred} is the tritium bred in the lithium blanket, F_{fus} is the tritium used a fusion fuel, F_{in} is the initial or top-up tritium inventory and F_{out} is the removal of tritium for external sources such as another reactor, sold for industrial applications or for weapons replenishment. In the above equation, losses of tritium due to decay is neglected. Kuan and Abdou [27] do not comment on this fact, however the averaged notation indirectly suggests that the authors made the assumptions that: 1) the ^{3}H→^{3}He decay is counter balanced by the ^{3}He(n,p)^{3}H reaction in the long term, which may also imply the use of ^{3}He as a purge gas and/or coolant, 2) The time which tritium is stored between being produced and used is small when compared to its half-life. For every D-T reaction in the plasma, a neutron is ejected that has the potential to initiate a $^6Li(n,\alpha)^3H$ reaction, hence a 1:1 ratio of tritium burn to tritium production is established. However, in order to achieve the required thermal and mechanical properties, the blanket is composed of a lithium compound/mixture. The finite reactor size and addition of other elements cause neutron leakage and losses in the breeding blanket, resulting in the number of tritium atoms being produced in the blanket being less than the number of tritons being burned in the plasma. To solve this problem neutron multipliers are placed within the lithium blanket in order to boost the number of neutrons entering the tritium breeding material. This counteracts the neutron losses and creates a neutron surplus, ensuring a TBR which is greater than unity. The most common neutron multipliers that appear in blanket concepts are beryllium and lead:

$$^{9}Be + n \rightarrow {}^{8}Be + 2n \quad \searrow \; 2^{4}He \qquad\qquad ^{208}Pb + n \rightarrow {}^{207}Pb + 2n$$

Both lithium and lead (n,2n) reactions are threshold (endothermic) reactions, which is evident from figure 2.3. A lead neutron multiplier operates in the liquid phase, due to its low melting point (600.61 K), and produces polonium-210 via bismuth, which is an α-emitter. This necessitates the online removal of polonium or bismuth [28]. The use of beryllium as a neutron multiplier also has the advantage of increasing the TBR by decaying to lithium directly or via helium. Other reactions exist that release more than two neutrons per reaction [29], however the majority either have high absorption cross sections (Zirconium) or produce radioactive daughter nuclides (Bismuth, Thorium) that would result in fusion power stations producing radioactive waste similar to that of fission power stations.

2.1.1 Energy Multiplication

In addition to the energy released from fusion in the plasma, additional energy is released and absorbed in the blanket due to exothermic and endothermic nuclear reactions. The Li-6 reaction is exothermic with a release of 4.8 MeV per reaction while the Li-7 reaction is endothermic, absorbing 2.5 MeV per reaction. Other materials within the blanket such as neutron multipliers also have an effect on the multiplication, especially fissile materials which have a positively significant effect on both neutron multiplication and multiplicativity (M). The general definition of M is given by [30]:

$$M = \frac{E_{plasma} + E_{blanket}}{E_{plasma}} = 1 + \frac{4.784\, R_{Li6} - 2.467\, R_{Li7} + \sum_{i}^{N} E_{i,nm}\, R_{i,nm} + \sum_{i}^{N} E_{i,f}\, R_{i,f}}{14.1}$$

where $R_{Li6} = \int\int \Phi \cdot \Sigma_{(n,\alpha)T} dEdV$, $R_{Li7} = \int\int \Phi \cdot \Sigma_{(n,n'\alpha)T} dEdV$, $E_{i,nm}$ is the energy released from neutron multiplication, $R_{i,nm}$ is the reaction rate of neutron multiplication, $E_{i,f}$ is the energy released from fission and $R_{i,f}$ is the fission reaction rate.

For a helium-cooled pebble bed reactor design with beryllium neutron multiplier the energy multiplication is given by:

$$M = 1 + \frac{4.784\, R_{Li6} - 2.467\, R_{Li7} + 2.1\, R_{Be9}}{14.1}$$

2.1.2 ICF First Wall

The ICF first wall will operate under unprecedented conditions. The structures will be subject to an extremely high flux of photons, neutrons and energetic target fragments, thus the choice of target is a significant factor in the design of ICF first walls due to the additional hohlraum debris and x-rays that the walls are subjected to in the case of in-direct targets [31]. The harsh irradiation conditions can be managed in essentially four ways ways:

- **Dry Wall** - This method utilizes materials with a resilience to extremely high temperatures and thermal properties that permit the absorption of energy [32]. Examples of such materials include carbon based structures and tungsten. Dry wall materials must be exceptionally resilient to evaporation, as a loss of just one layer of atoms per shot would result in more than a centimetre of material being lost each year. The dry wall has the advantage of being the most technologically simple of all of the wall concepts, however the damage rates are likely to decrease availability, increase operational costs associated with component replacement and increase the amount activated materials to be sent for waste disposal.
- **Wetted Wall** - The first wall is protected by a flow of liquid along the surface, a flow of liquid through a porous structure or a spray of liquid near or on the surface [33]. The advantage of materials in the liquid phase is that they do not suffer from crystal damage, such as dislocations and interstitials, in the same way as solid materials due to an inherent lack of crystal structure. The wetted wall softens the radiation spectrum, resulting in an increased lifetime of the solid wall. A homogeneous coverage of liquid is an absolute requirement, as a flux of $1 J/cm^2$ incident on any dry wall material, regardless of their refractory proficiency, would result in the evaporation of several layers of atoms per shot.
- **Liquid Wall** - This concept is based on a thick flow of liquid, such as lead or FLiBe, between the target and the first wall, such that the neutrons are highly moderated and subject the first wall and blanket structures to softened neutron spectrum that results in an increased blanket lifetime. The reduced damage to the walls lowers operational costs associated with component replacement and increases availability as a result of less maintenance. Hence, if the technological issues are overcome, the implementation of liquid walls is likely to reduce the cost of electricity when compared to dry walls. The liquid wall can also significantly reduce the radioactive waste produced when compared to the dry

wall, due to the frequent replacement of dry wall components, which are considered to be high level radioactive waste. The liquid, within the blanket, is recirculated for the lifetime of the reactor, hence only one batch of radioactive waste need to be disposed of during the lifetime of a reactor with liquid walls.

- **Gas Filled Chamber** - Approximately 30% of the fusion yield is in the form of x-rays and target debris [34]; Both of which have the potential to cause significant damage to the first wall. This can be prevented by filling part of the chamber with a gas such as xenon, which has a high x-ray absorption cross-section [35], which will absorb and re-irradiate the energy in a spectrally and temporally softened manner, reducing damage to the first wall.

Protection of the first wall will inevitably have a detrimental effect on the laser beam quality incident on the target capsule. Direct drive chambers are likely to require a wetted wall or liquid first wall to protect against neutron damage, while indirect drive chambers will require inert gas protection of the FW to protect against the x-rays produced in the hohlraum and possibly additional liquid / wetted FW. Before hitting the target capsule, the laser or ion beams will have to travel several meters through the inert gas, liquid metal vapor and target debris resulting in the interaction, and ultimately the degradation, of the finely tuned and focused beam with the gas/vapor. Several physical processes exist which contribute to the degradation of the laser beam which include [36], but are not limited to, stimulated Raman scattering [37], refractive defocusing [38], inverse bremsstrahlung [39] and filamentation [40].

The design and specifications of MCF and ICF blankets may be significantly different even if the reactor power and reaction type is identical. Each of the reactor blankets have their own advantages and disadvantages which can lead to added complexity of blankets, reduced performance or reduced lifespan. Table 2.2 shows a brief summary of the differences between ICF and MCF blanket physics [41].

ICF	MCF
Extremely high instantaneous neutron flux	Relatively low/constant neutron flux
No MHD effects	MHD - liquid wall interaction
Energetic target debris	ELMs/Disruptions
X-ray damage - especially with indirect drive	

Table 2.2: A comparison of ICF and MCF blanket properties.

The temporal profiles of ICF and MCF neutron fluxes differ by many orders of magnitude. An ICF neutron pulse is typically in the order of 10's of picoseconds whereas MCF pulses are likely to be greater than 1000's of seconds in a fusion power reactor. The extremely low ICF confinement time results in a large neutron flux, which can broaden the range of nuclides being created as a result of transmutation/activation. This phenomenon occurs in stellar evolution where particular nuclides can only be formed at latter stages of a star's life, when it is hotter and the neutron flux is higher. This increased neutron flux results in short lived nuclides being transmutated before they have a chance to decay, thereby increasing the chances of heavier and more exotic nuclides being created. This may have a significant impact on the nuclear decommissioning of ICF fusion power plants as exotic nuclides are more likely to exhibit undesirable decay patterns.

A physical phenomenon of interest is that of the temporal broadening of the sharp neutron pulse as it travels through the fusion blanket. The width of the pulse at the first wall is initially of the order of nanoseconds wide, which then broadens to many milliseconds at the last wall, as a result of many scattering events. Figure 2.5 shows a simulation of the temporal profile a 14.1MeV neutron pulse within a spherical blanket geometry with dimensions which are similar to the HYLIFE conceptual IFE reactor.

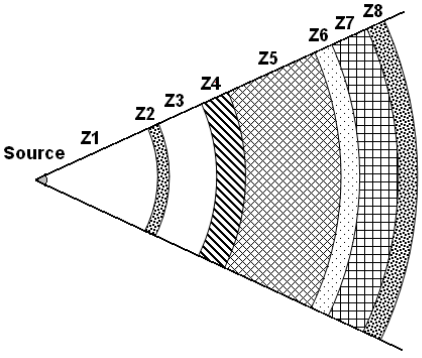

Material	Radial depth (cm)	Zone
Vacuum	300	1
Molten salt	40	2
EUROFER	5.2	3
FLiBe	50.1	4
EUROFER	2.5	5
FLiBe	12.5	6
EUROFER	2.5	7
SiO2	10.2	8

Figure 2.4: HYLIFE-like blanket geometry transformed into a spherical model

One of the most significant differences between ICF and MCF emissions is the effect of extremely damaging x-ray radiation on the ICF first wall. The x-rays, which have particularly high flux for indirect drive ICF ignition, can ablate the first wall at a rate of several centimetres per day, for a typically sized reactor, if no first wall protection used. In addition to the instantaneously high neutron fluxes that the first wall is subjected to, the presence of ICF target debris and alpha particles is also of concern for the ICF first wall.

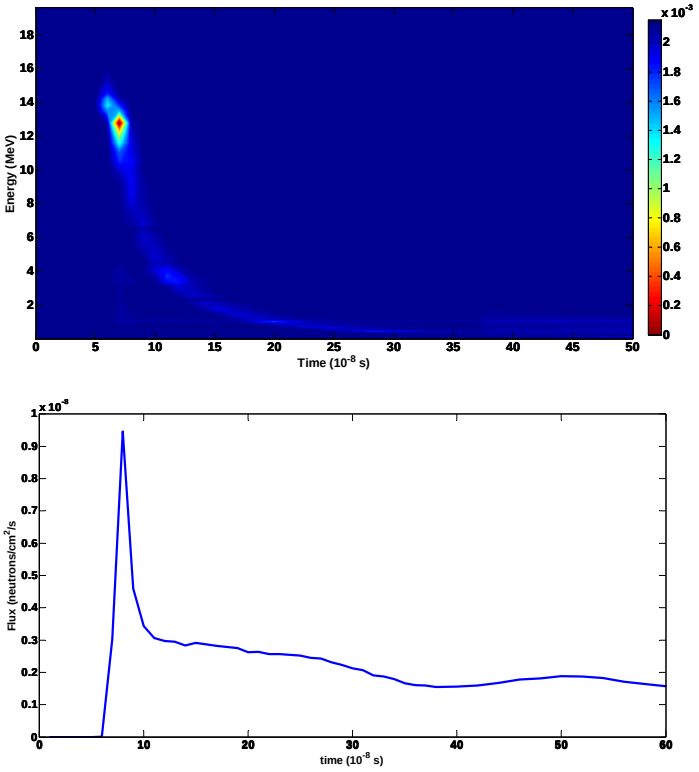

Figure 2.5: Temporal profile of neutron pulse at the back of a blanket of 73 cm thickness. The neutron pulse is initially ∼ps wide, after LiPb, silicon carbide and FLiBe moderation the pulse length is ∼ms wide.

	Laser direct drive	Targets with high Z layer
Neutrons	75%	70%
X-rays	6%	22%
Debris	19%	8%

Table 2.3: Mechanisms for energy output[42]

2.1.3 Tritium Breeding Blanket Concepts

The ICF tritium blanket concepts are broadly similar to MCF blankets after the first wall issue is addressed. The following section provides a brief overview of tritium blanket concepts, which is largely based on MCF research:

- **Water cooled lithium lead (WCLL)** [43] – A liquid eutectic formed by approximately 17% lithium and 83% of lead, at maximum of 550^oC [44], flows within channels constructed with SiC . The blanket is cooled with water, flowing in adjacent channels to the LiPb, and has a temperature and pressure similar to PWR fission reactors ($T_{in} = 265^oC$, $T_{out} = 325^oC$) [45]. For MCF reactors, the liquid metal must be circulated slowly through the blanket to avoid magneto hydrodynamic (MHD) effects in flowing liquid metals, however

an ICF reactor does not have this restriction.

- **Helium cooled pebble bed (HCPB)** – This concept [46] is based on solid blanket modules constructed with low activation martenstitic ferritic steel, such as EUROFER, and contains neutron multiplying pebbles ($\sim 1mm$) of beryllium or beryllide mixed with breeding pebbles (∼0.5mm) of a lithium compound, such as Li_4SiO_4, $LiAlO_2$, Li_2AlO_2, Li_2AlO_3. Helium acts both as a coolant and a tritium purge gas. The thermodynamic efficiency is higher than in WCLL due to a larger temperature differential (Tin = 250^{o}C, Tout = 500^oC). The blanket lifetime is limited to around 5 years due to irradiation damage, transmutation of blanket material and a finite tritium breeding capability.
- **Self Cooled LiPb** – This concept utilizes lithium as both breeder and coolant and has the advantage of high thermal conductivity and heat capacity. However, the highly reactive nature of lithium raises safety concerns and requires electrical insulation between the structure and liquid metal due to MHD effects [47] in a MCF reactor.
- **Dual Coolant Concept** – This concept is based on the liquid lithium lead concept, however comprises of additional helium cooling of the ferritic steel structure. This helium cooling at the first wall enables a higher blanket temperature, raising the thermodynamic efficiency, and also eliminates the need for electrical insulation against the MHD pressure on the liquid metal.

2.1.4 Liquid breeders

The liquid breeder has many advantages over the solider breeder, which include:

- Separate neutron multiplier not needed
- Separate coolant not needed for SCLL
- Online TBR control
- Reduced nuclear waste
- Resistant to radiation damage

However, many issues exist which still need to be overcome before the liquid breeder can become a practical solution for tritium breeding:

- For MCF reactors, an insulating coating is necessary in order to reduce the MHD pressure drop within the liquid metal [48]
- Structural materials need to be chemically compatible, to prevent/limit corrosion and reduce tritium permeation
- Tritium recovery and retention within the blanket.

The suitability of a material to be used as a liquid breeder is based on a number of factors, which include:

- **Neutronics** - The tritium breeding capability and the energy multiplication must be as high as possible in order to achieve an efficient and sustainable power plant.
- **Solubility** - As the solubility of gases within the liquid breeder increases the gas becomes more difficult to extract. Therefore, materials with low Sieverts' constants within the temperature range of the blanket are most suitable.
- **Melting point** - A high melting and boiling point will prevent the coolant from boiling, thus allowing higher temperatures and increased thermal efficiencies.
- **Specific heat** - A liquid metal with a high specific heat capacity will enable the lowering of the coolant circulation rate and an increased thermal efficiency of the heat exchanger.
- **Thermal conductivity** - A high thermal conductivity and low viscosity will increase the convective heat transfer rates, increasing thermal efficiency.
- **Chemical properties** - The initial composition of the liquid metal and its activation products must be chemically matched with the structural components in order to reduce corrosion. In addition to corrosion, the permeation or leakage of coolant into the liquid lithium based metals can cause explosive reactions.

- **Nuclear waste** - The material composition of the liquid breeder may be considerably different at the end of the reactors lifetime when compared to the composition at start-up. Transmutation products are likely to build-up, possibly resulting in the need for geological disposal of the breeder material. Choosing materials which have low activation/ transmutation properties will reduce the amount of nuclear waste to be processed and, as a result, may reduce the cost of electricity. Also, ensuring the purity of the liquid metal is important. For example, small traces of bismuth in lead will result in an increased amount

of the highly radio-toxic Po-210.

A summary of the physical properties of the liquid breeders is shown in table 2.4. The three possible liquid breeders are pure lithium, LiPb and FLiBe:

- **Pure lithium -** Pure lithium has a higher tritium breeding capability than LiPb or FLiBe, however it is a highly chemically active alkaline metal. Its highly reactive nature with both air and water could result in hydrogen explosions in the event of breeder leakage. If a coolant is required, an inert gas such as helium would certainly have to be used in conjunction with pure lithium. Pure liquid lithium has a high tritium solubility, hence the tritium partial pressure is relatively low which results in little permeation into the coolant. Numerical simulations performed by Gervasini [49] of permeation into coolant suggest that pure lithium is most suitable for a separately cooled blanket. The low partial pressure becomes problematic at the tritium recovery stage where more sophisticated techniques such as molten salt, cold trapping or gettering are required due to the inability of the tritium to be released in the gas phase.
- **Lithium-Lead -** The number density ratio associated with the eutectic point of the LiPb alloy is commonly quoted as 17:83, however the the most recently quoted ratios are approximately 16.3 : 83.7 [50]. Due to the relatively high tritium partial pressure in LiPb the tritium tends to leak through the structural materials into the coolant. Based on the numerical simulations of permeation into coolant performed by Gervasini [49], LiPb requires permeation barriers in order to be used in a separately cooled blanket. Thus, the self-cooled lithium-lead blanket may be preferable over the helium or water cooled lithium lead blankets. The solubility of tritium in LiPb is relatively low, thus the extraction of tritium requires less complicated technologies, such as spray towers or permeation barriers, when compared to FLiBe or pure lithium.

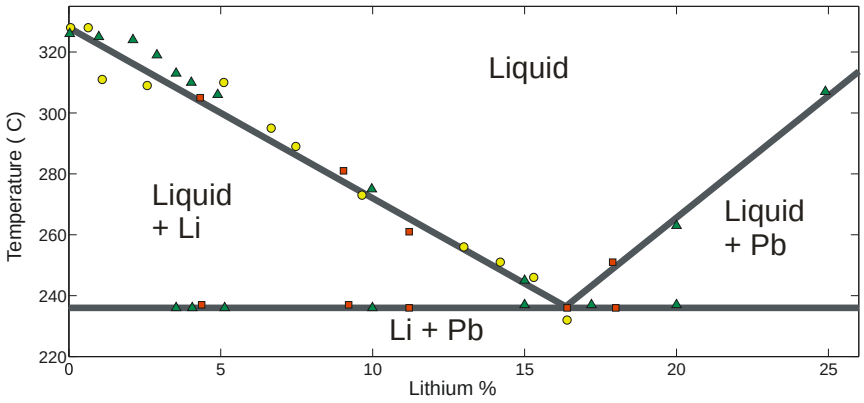

Figure 2.6: Phase diagram of lithium-lead alloy [50] with the location of the eutectic point - the chemical composition which results in the lowest temperature at which a material solidifies.

- **FLIBE -** The tritium breeding capability of FLiBe is the lowest of the three compared, however this can be increased with neutron multipliers. This is evident from the ratio of lithium within the chemical compound, Li_2BeF_4. It is very chemically stable and can operate up to 650 $°C$ with steel structural materials [51]. As with LiPb, the high partial pressure of tritium within FLiBe allows for a less complex tritium recovery system to be used. For the same reason, the numerical simulations of Gervasini [49] of tritium permeation into coolant shows that FLiBe is not suitable for a separately cooled blanket. The electrical conductivity of FLiBe is three and four orders of magnitude higher than that of LiPb and Li. Thus, it is particularly suitable for use in MCF reactors where the MHD pressure drop is less prominent [30].

Property	Unit	Li	LiPb	Li_2BeF_4
Density	g/cm^3	0.48	8.98	2.0
Li density	g/cm^3	0.48	0.062	0.28
Melting point	$°C$	180	235	459
Viscosity	P	3.6×10^{-3}	2.0×10^{-2}	1.5×10^{-1}
Specific heat	$J/g \cdot K$	4.2	~0.15	2.34
Chemical reactivity	-	Active	Middle	Almost stable
Tritium solubility	-	High	Very low	Very low
Thermal conductivity	$W/m \cdot K$	48	25	1.1

Table 2.4: Comparison of physical properties of liquid tritium breeders. Data compiled from [52], [53] & [54].

2.1.5 Tritium Recovery

After the tritium has been produced in the liquid metal blanket it must be extracted by a process which is energy efficient, capable of reducing the tritium concentration down to ∼1 appm and capable of achieving an extraction rate of at least 300g per day. Many tritium extraction methods have been suggested, however very few have been tested thoroughly for the application of fusion. The remainder of this section describes the three most promising tritium extraction methods.

Cold trap

The cold trap technique, which is commonly used in fission fast breeder systems [55], relies on the differences of partial pressures within liquids in order to extract particular isotopes. Several concepts have been proposed in which an intermediate Na or NaK circuit is placed between the LiPb and the water coolant. The relatively small tritium partial pressure in NaK when compared to LiPb allows the tritium to permeate between the LiPb and the NaK, which then precipitates as a tritide in the NaK. The tritium is recovered in a separate loop where it is heated, causing the tritide to decompose and rise to the surface where it can then be removed by a vacuum pump. The advantage of having an additional loop of NaK within the blanket (as opposed to having an NaK loop external to the blanket) between the Pb and the water coolant is the significant reduction of permeation from the Pb to the water [56].

Gettering

The gettering method takes advantage of the solubility of tritium in yttrium being larger than in lithium. Liquid lithium is passed through beds of scintered small yttrium pebbles resulting in the production of yttrium tritide. In order to continue to extract tritium from the lithium, the tritium atoms must recombine at the surface of the gettering bed. Moriyama [48] points out that the rate of regeneration of tritium via gas purging is too slow, however a combined gettering and molten salt process was proposed [57] which includes a secondary lithium loop (600^oC) which regenerates tritium from the yttrium bed(300^oC). Equations 2.1 [58] and 2.2 [59] show that the Seivert constants for tritium in yttrium decreases at a faster rate than tritium in lithium as temperature increases, thus the increased temperature in the secondary loop allows the concentration of tritium in the secondary loop to increase by a factor of 20.

$$K_{Y-T} = 0.55\, exp(22900/RT) \tag{2.1}$$

$$K_{L-T} = 42.8\, exp(10104/RT) \tag{2.2}$$

Where R is the universal gas constant. The tritium in the small secondary loop can be extracted using the molten salt method. The advantage of this process is that the primary loop does not get contaminated with impurities, as with the molten salt process alone [57] and the tritium extraction occurs away from the blanket, unlike the cold trap method which complicates the neutronics and introduces more activation products.

Molten salt

The three-stage molten salt extraction process was proposed by Maroni [60]. The first stage involves mixing the liquid lithium, which contains tritium, with a salt mixture of lithium halides in a centrifugal contactor/seperator [48], generating tritium salt in the form of LiT. The second stage involves the use of electrolysis in order to form T_2 from the oxidation of LiT. The tritium is extracted from the electrolysis unit by purging it with helium bubbles. The third step involves the separation of the helium-tritium mixture and the removal of impurities.
Several technical difficulties are associated with this process, such as efficient and effective extraction units. However the greatest problem associated with this technique is the contamination of the liquid lithium with traces of salts which will have an effect on: blanket neutronics, the corrosion of structural materials and the creation of transmutation products [61].

2.2 Radioactivity

In order for fusion energy to sustain government support and funding, gain public acceptance and gain the support of the media, a transparent and persuasive strategy for safely dealing with and minimizing radioactive waste produced by fusion power plants must be devised.

2.2.1 Radioactive Waste

The IAEA defines radioactive waste as "Any material that contains or is contaminated by radionuclides at concentrations or radioactivity levels greater than the exempted quantities established by the competent authorities, and for which no use is foreseen" [62]. In the case of spent nuclear fuel, the definition of waste and resource varies from country to country, mainly depending on the choice of open or closed fuel cycle.

The general classification of wastes, according to the IAEA, are shown in table 2.5, however further regulations are likely to be imposed by the local authorities which may limit activities of specific isotopes, go beyond the IAEA regulations or limit overall volumes/activities.

Waste Class	Typical Characteristics	Disposal options
Exempt waste (EW)	Activity levels at or below clearance levels	No radiological restrictions, normal landfill
Short Lived (L/ILW-SL)	Restricted long-lived radionuclide concentrations, e.g. long lived α emitters, average <400Bq/g or 4000Bq/g maximum per package	Near surface or geological disposal
Long Lived (LLW)	Long lived radionuclide concentrations exceeding limitations for short lived wastes	Geological disposal facility
High-level waste (HLW)	Thermal power greater than about 2 kW/m^3 and long-lived radionuclide concentrations exceeding limitation for short lived wastes.	Geological disposal facility

Table 2.5: Waste classification as defined by the IAEA [63]

Many methods for reducing the amount of fusion/fission waste for burial have been proposed/implemented. These include:

- It has been suggested that HLW could be diluted in order for it to be classified as LLW. As a general rule, the "dilution as the solution to pollution" [64] cliche is not endorsed by governments mainly for three reasons: the public unease regarding the burial of nuclear waste regardless of its classification, the cost of waste disposal generally being based on volume and the limited amount of low-level waste disposal sites.
- The volume of waste that is to placed in a waste depository can, in some cases, be reduced by interim storage for up to 100 years [65]. In this time, the radiotoxicity can decrease to below clearance levels or reduce the radiotoxicity class. Although interim storage is not ideal, it is cost-effective procedure which is widely recognized as an acceptable practice while more permanent solutions are being devised.
- A further way to reduce the amount of waste that goes to a waste depository is the recycling of the material, such as reusing the material within other areas of the nuclear industry [66].
- Ensure very low levels of impurities within structural materials, which lead to undesirable transmutation products, before the component is used in the reactor assembly.

Isotope	Decay	Reaction	Component
^{94}Nb	$^{-}\beta$	$^{93}Nb(n,\gamma)$	Steels, Nb and V based alloys and super conducting magnet
^{99}Tc	$^{-}\beta$	$^{98}Mo(n,\gamma)(^{-}\beta)$	Mo-based alloys and steels
^{186m}Re	γ	$^{186}W(^{-}\beta)$	W based alloys
^{108m}Ag	γ	$^{107}Ag(n,\gamma)$	W based alloys
^{63}Ni	$^{-}\beta$	$^{62}Ni(n,\gamma)$	Steels and copper alloys
^{29}Al	$^{+}\beta$	$^{29}Si(n,\alpha)$	SiC composites
^{208}Bi	$^{+}\beta$	$^{208}Pb(n,\gamma)^{209}Pb(\beta)$ $^{209}Bi(n,2n)$	LiPb breeder
^{210}Po	α	$^{208}Pb(n,\gamma)^{209}Pb(\beta)$ $^{209}Bi(n,\gamma)^{210}Bi(\beta)$	LiPb breeder
^{14}C	$^{-}\beta$	$^{13}C(n,\gamma)$	FLiBe breeder

Table 2.6: Long-lived isotopes that contribute to fusion HLW. Partly compiled from refs [68, 69]

Although fusion power plants do not produce transuranic waste, HLW is produced via the recycled materials, refractory metals and liquid breeders [67]. Some isotopes that contribute to long-lived fusion waste are listed in table 2.6.

Although the nuclear industry should never be complacent about its waste disposal responsibilities, it must be stated that the current fission wastes account for less than 1% of the total toxic wastes produced in OECD countries in terms of volume [70]. In addition to this, the high level waste forms just 3% of the total nuclear waste volume. A study performed in 1978 [71] showed that the radioactivity from coal ash, produced in a 1GW power station, can be more radioactive than the nuclear waste produced from an equivalent PWR. The volumes of nuclear waste associated with a fusion power plant is expected to be similar to that of an equivalent fission plant, however radioactivity and the amount of HLW is expected to be significantly less [72].

In addition to the classifications described in table 2.6, the waste disposal rating (WDR) and clearance index (CI) are also used to determine the means by which radioactive waste is to be dealt with. The WDR is used to specify whether a material would qualify for shallow land burial [73] (USA class C) and is defined as the ratio of the specific activity (in Ci/m^3 at 100 y after shutdown) to the allowable limit summed over all radioisotopes. For a material containing N isotopes, each of which have specific ativity , S_i (Ci/m^3), and waste disposal limits, L_i, the CI is defined as:

$$WDR = \sum_{i}^{N} \frac{S_i}{L_i}$$

A material with a WDR < 1 is categorized according to 10CFR61 rules (USA):

The clearance index specifies whether the material can be released from regulatory control or

Waste Class	Definition	Disposal
Class A Segregated waste	Decays to acceptable levels during site occupancy	Segregated, minimum requirements
Class B Stable waste	Stabilized and decays to levels that do not pose a danger to public health and safety in 100 years	Covered to reduce surface radiation to a few percent of natural background.
Class C Intruder waste	Does not decay to safe levels in 100 years. Decays to acceptable safe levels in 500 years	Five meters below surface with natural or engineered barrier
Waste that does not meet Class C definition	Does not qualify for near surface disposal. Proposed disposal methods are considered on a case-by-case basis	Geologic

Table 2.7: Nuclear waste classifications under 10-CFR 61 rules [74]. The acceptable safe levels are defined as a whole body dose of less than 0.5 rem/y (about 5 times natural background radiation) given full exposure to the waste.

"cleared" [75]. In order for a material to be cleared the predicted effective dose to be incurred by any member of the public must be less than $10\mu Sv$ per year and the committed effective dose must be less than 1 Man.Sv per year [76]. A clearance index of less than unity is required in order for a material to be cleared. For a material containing N isotopes, each of which have an associated activity , A_i ($Bq\,Kg^{-1}$), and an IAEA clearance level, C_i, the CI is defined as:

$$CI = \sum_{i}^{N} \frac{A_i}{C_i}$$

At present, the only countries where clearance can be applied are Germany and Spain; Industries in some countries, such as the US, do not support clearance due to potential damage to the image of their products [77].

2.3 ICF Reactor Conceptual Studies

Several ICF reactor concepts have been published in the last 20 years. Each of which vary in terms of their drivers, targets, blankets, size and power output. In order to illustrate the various IFE reactor technologies that have been proposed, the SOMBRERO, HYLIFE and Prometheus designs are to be discussed in this section; however many other designs such as HIBALL, LIBRA, SOLASE, SIRIUS and OSIRIS also exist.

2.3.1 HYLIFE-II

The HYLIFE-II concept was progressively developed in the early to mid 1990's and is based on the earlier HYLIFE concept developed in the late 80's. The key features of the HYLIFE design

are the FLiBe jet array and coolant. Oscillating FLiBe jets are directed vertically down towards the target; A deflector is positioned between the jet nozzle and the target, causing a pocket to be formed in the FLiBe [33]. This pocket will expand as it falls towards the position of the target, allowing space for the target to be injected and irradiated. The 2m long deflector is protected from the intense neutron pulse due to the liquid FLiBe flow around it as it forms the pocket for the next target [34] . HYLIFE-II is a 1000 MWe IFE power plant, driven by a 6 Hz ion beam that yields 350 MJ per target [78]. Oscillating and stationary nozzles form a "pocket" or void within a liquid FLiBe flow, within which the target resides as it falls under gravity. The 10cm thick FLiBe jets are thick enough to attenuate the neutron pulse (approx seven, 14 MeV neutron MFP's). The liquid jets are used to protect the SS304 steel walls in order to achieve a long lifetime, low cost and low environmental impact [79]. Beyond the FLiBe jets, a 50cm blanket is contained with a 3cm SS304 wall where the remainder of the heat is absorbed and more tritium is produced. Sahin [80] claims that the addition of ThF_4 with percentages of 4% and 12% in the FLiBe can produce 450 M \$/year and 100M \$/year in revenue due to the increased energy multiplication. The increase in neutron number is also likely to increase tritium production. For the 1 GWe design, the blanket multiplication without additional fissionable material is expected to be 1.18, based on fusion and thermal power's of 2100 W and 2500 MW respectively [78]. With an expected lifetime of 30 years [81], the longevity of the structural SS304 is relatively high, which has the effect of increasing the availability and decreasing the cost of electricity.
Based on the TART-ACAB modeling of Reyes et al. [82] the waste disposal limits (WDR's) and clearance indexes (CI's) were evaluated for HYLIFE-II. After 1 year of cooling the concrete confinement building CI drops below unity, which is a significant positive considering the building accounts for ∼71% of the volume of waste. The work of Lee. et al [83] shows that the structural materials are classified as a mixture of C and A, while the coolant is classified as C and mixed.

2.3.2 Prometheus-H

The Prometheus-H conceptual design is a heavy-ion driven, 1000MW power plant design [84] developed by Waganer et al in 1994. In the same paper Waganer also proposed a laser driven design Prometheus-L with similar technologies as the H design. The target yield is significantly higher with an ion driver, requiring only a relatively low repetition rate of 3.54 Hz. The relatively high efficiency of LINAC's when compared to the lasers employed in other designs improves the overall energy multiplication of the system and also results in a lower cost of electricity. The structural materials, wall and some blanket components are composed of silicon carbide (SiC)

due to its high resistance to radiation damage, good fatigue characteristics and low activation [85]. The Prometheus-H design is an indirect drive design with a single beam LINAC as a driver which forms 12 beamlets, with 6 beamlets forming each 8.54° conical array. The first wall is comprised of porous SiC, with equatorial radius of 4.5m, covered by a 0.5 cm surface layer of liquid lead which protects the wall from the fusion micro-explosions, transporting target fragments away from the chamber and enhancing the vacuum seal in the chamber. In total, a 5cm channel of lead is used to cool the first wall. The lead coolant enters the chamber at the top and flows downward under the action of gravity at a rate of 54422 Kg/hr. Along its path, the lead absorbs approximately 40% of the fusion energy released, raising its temperature from 375 $°C$ at the inlet to 525 $°C$ at the outlet. A LiO_2 pebble bed breeder is situated behind the first wall which is cooled with helium that enters the blanket at 400 $°C$ and leaves at 650 $°C$. Tritium is produced in the blanket with a TBR of 1.2 (initially) and is removed from the blanket by the helium purge/coolant. The Prometheus-H design is preferable over Prometheus-L due to the significantly reduced number and size of ports required for incoming driver. The ion beam requires only two 2 cm diameter ports in the blanket, whereas the laser beams require 60 ports that range from 15 to 20cm in diameter. Thus, the H blanket design is less complex and allows for greater blanket volume.

Due to the use of SiC as the majority of the structural components, the Prometheus-H design is one of the most environmentally friendly concepts [86]. The structural components are a mix of class A and C, while the lead coolant is classified as C and mixed.

2.3.3 SOMBERO

The Sombrero conceptual design [87], devised in the early nineties, is a KrF laser driven IFE power reactor with a lithium oxide pebble bed tritium breeding blanket. The Sombrero chamber design, shown in figure 2.7, is comprised of 12 wedge shaped modules; each of which have their own inlet and outlet pipes. The inlet pipe supplies a steady flow of helium and LiO_2 particles of size 300-500 μm with a temperature of 550°C and void fraction of 40%. The helium gas aids in the flow of the pebbles and purges the tritium produced. The pebbles flow through the blanket due to gravity and exit the chamber with a temperature of 700°C at the first wall and 800°C at the rear of the blanket. Once the LiO_2 particles have exited the blanket they are transported to heat exchangers, with a flow rate of 2×10^7kg/hr, in a fluidized state by helium gas at 0.2MPa [88].

The Sombrero driver is a KrF laser which enters the reactor through 60 near symmetric ports

within the blanket, which subtend less than 0.3% of the solid angle. The blanket modules are 1m thick and contain layered LiO_2 channels and graphite, with the graphite thickness increasing towards the back of the chamber in order to decrease neutron leakage and maximize TBR and energy multiplication. Inside the chamber, 0.5 torr of xenon gas is used to reduce x-ray induced first wall damage. The maximum displacements per atom (dpa) and helium production in the graphite is 15.3dpa/FPY and 3770 He appm/FPY respectively, which is expected to produce a first wall lifetime of approximately 5 years. Dielectric final focussing mirrors (FFM) and grazing incidence metallic mirrors (GIMM) are located 50m and 30m away from the target respectively. The FFM is out of sight of the target while the GIMM is partly protected by neutron traps [89]. Beyond the rear of the blanket a 2.7m steel reinforced concrete shield protects the workers who are subject to a maximum 2.5mrem/hr dose rate. The Sombrero design is a relatively low activation design, as both the chamber and the shield would qualify for class A - low level waste disposal, while the lithium particles would qualify for class-C LLW disposal [90].

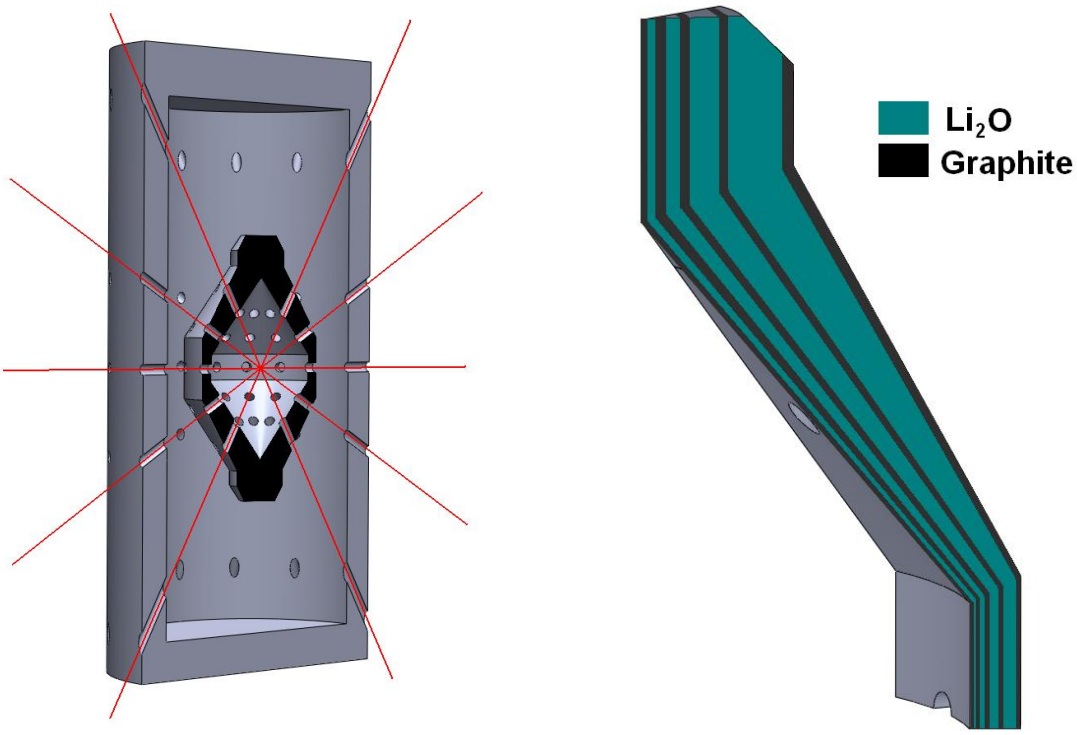

Figure 2.7: The Sombrero chamber [32].

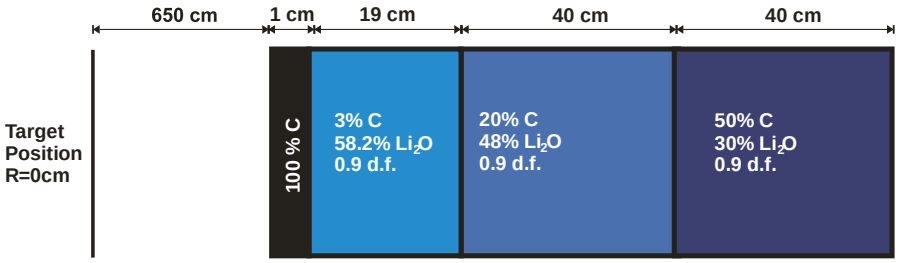

Figure 2.8: SOMBRERO blanket dimensions and material composition. Adapted from [89].

2.4 Burn-up Codes

When a material is irradiated with particles (such as neutrons, protons, deuterons etc) a number of reactions can occur. Depending on the nuclides which are being irradiated the nuclide may absorb the incoming particle, collide with the particle, causing it to scatter, or it may break up into two or more smaller atoms (fission) as a result of the interaction. The probability of absorption, scatter or fission is defined mathematically by the cross-section, σ, of a particular reaction. Although more than eighty reactions can occur within a reactor, the four main cross-sections of relevance for nuclear reactors are: absorption (σ_a), scatter (σ_s), fission (σ_f) and neutron multiplication (n,xn).

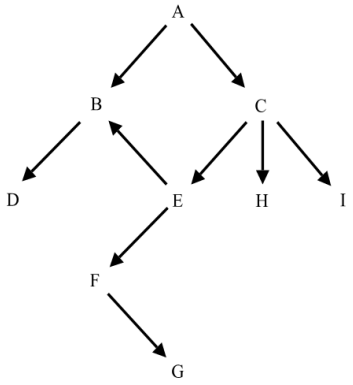

Figure 2.9: Hypothetical nuclide transmutation tree

Once a parent nuclide has undergone a reaction, the nuclide may be left in an excited state, transmutated into a different nuclide or may be converted into daughter nuclides. These daughter nuclides will have different reaction cross-sections to the parent nuclide, resulting in different types and rates of reaction. This phenomenon is shown in figure 2.9, whereby a hypothetical material composed of just one nuclide, A, is irradiated, producing nuclides B-I as a result. When the irradiation ceases, the cohort of nuclides contained in a material will continue to change as a result of nuclear decay. The rate at which a particular nuclide will decay into a more stable nuclide is dependent on the decay constant, λ, which is specific for that particular nuclide. When decay is the only nuclear process occurring, the decay pattern is monodirectional i.e. the arrows in figure 2.9 only point down. The mass of the daughter nuclides, as a result of decay, is always equal to or lighter than the parent atom. An activation code models the chains of reactions with respect to time by utilizing nuclear databases that define the cross-sections and decay constants for every nuclide.

An activation/burn-up code solves the Bateman equations [91]:

$$\frac{dN_i}{dt} = -\left(\lambda_i + \sigma_i^a \phi\right) N_i + \sum \left(\lambda_{ij} + \sigma_{ij}^a \phi\right) N_j + S_i \sum N_k \sigma_i^f \phi \tag{2.3}$$

Where N_i is the number density of nuclide i at time t, λ_i is the decay constant of nuclide i, λ_{ij} is the decay constant of nuclide j producing nuclide i, σ_i is the absorption cross-section of nuclide i, σ_{ji} is the reaction cross-section for nuclide j producing nuclide i, ϕ is the neutron flux density and S is a fission source.

Activation and burn-up codes generally perform the same functions and utilize the same mathematical methods. However, the term burn-up code originated from the fission industry where the codes calculate the depletion of fissile materials and the production of daughter nuclides. Many burn-up/activation codes exist, each of which solve eqn 2.3 with different computational methods. The most commonly used activation codes are:

- **FISPACT** [92] - An inventory code included in the European Activation System (EASY), produced by EURATOM/UKAEA. The code was originally written in the 1970's, however, many additional features have been added to new versions such as a new high-order numerical time-stepping methods. FISPACT has recently been re-written and is linked to the comprehensive EAF cross-section library which now includes very short lived nuclides which are of interest to IFE studies.
- **ACAB** [93] - Developed at the University of Madrid, the ACAB code can perform space-dependent inventory calculations allowing for multidimensional neutron flux distributions, produce uncertainty analysis and perform damage analysis. It relies on the Taylor series to compute the matrix exponential.
- **ALARA** [94]– Developed at the University of Wisconsin, Madison, USA. The code was written as part of a PhD project by Paul Wilson in 1999. This code is one of the most advanced in terms of its computational methods, although it does have the disadvantage of having no uncertainty calculations.
- **RACC** [95]- Developed to compute the radioactivity and radioactivity-related parameters (e.g. after heat, biological hazard potential, etc.) due to neutron activation within MCF and ICF reactor systems. This code solves the burn-up equations analytically, via the matrix exponential which is calculated using Schur decomposition.

In theory, the number of different nuclides produced during an irradiation is infinite. If the matrix method is used to solve the rate equations, the infinite amount of nuclides created translates to computing a matrix exponential of infinite size, and for numerical solution this translates to solving an infinite set of ODE's, both of which are obviously impractical. In order to eliminate this problem, nuclides with "negligible" contribution to the whole nuclide cohort should be truncated (i.e. removed from the system). Defining which nuclides have negligible contribution is not a trivial matter and can be approached in a number of ways. The matrix method of solution

causes the chain truncation to be more complicated due to the transfer matrix being stiff (fixing the amount of nuclides), whereas numerical methods can allow more nuclides to be added to the system as time evolves. Absolute value discrimination and chain length cut-off are the most common nuclide cut-off methods, although other methods exist.

Absolute Value Discrimination

This is the most simple technique that can be used to truncate a nuclide chain and simply consists of testing whether the number of a particular nuclide, N_i is above a threshold after a set time period; if it is not then that nuclide is destroyed.

i.e If the total number of nuclides in the cohort is 10^{24} then the absolute value discrimination could be defined as:

if $N_i < 10^{15}$, destroy nuclide N_i

The discrimination also needs to consider the relative cross-sections and radioactivity of the nuclide to be trunctated, in order to ensure that small build-up does not get neglected.

Chain Length Cuttoff

This method is based on limiting the number of nuclide generations in a single time-step. Thus, considering the absorption process, for each time-step, no more than M successive absorptions can take place. Hence, nuclides which are more than M generations away from the initial nuclide composition will not be included in the simulation. When considering decay processes, nuclides which are singularly the product of a decay which takes place on a time scale which is much larger than the time scale of the simulation must also be removed from the system.

2.4.1 Pulsing

The addition of neutron flux shaping, such as pulsing, to a burn-up calculation can increase the computational expense considerably. The ability to resolve the response of nuclides to a changing neutron flux is important for a burn-up code to be ICF compatible. Fully resolving neutron pulses such as those produced in an ICF reactor is practically computationally impossible with numerical time-stepping methods, as approximately 2 million pulses need to be resolved each year. Although methods such as the continuous pulse model can be used to reduce the computational expense, accuracy is always compromised when pulse resolution is reduced. Both the analytic method (matrix exponential) and the numerical methods have a computational expense which scales linearly with n, where n is the number of outputs. However, the analytic

method of solution can resolve a large number of pulses in blocks, which results in a weaker dependence on n when compared with the numerical solver. This statement is confirmed with the following proof.

In order to estimate the computational time required by each method, a basic floating point operation ("flop") is defined [96], which is the time taken to compute

$$A(i,j) = A(i,j) + T * A(i,k)$$

This flop involves a floating point multiplication, an addition and some basic storage operations. The number of flops needed for a matrix×matrix multiplication is Q^3, the number needed for matrix*vector is Q^2, where Q is the size of the matrix.

The analytical solution is defined as $N = N_0 exp(nAt_\Delta)\, exp(nBt_\theta)$, where n is the number of pulses between data output, t_Δ and t_θ are defined in figure 2.10, N and N_0 are the nuclide vectors at t and t=0 respectively, and A & B are the transfer matrices. Assuming the Taylor series expansion is utilized, the calculation of each matrix exponential requires "i" matrix multiplications. Hence, the number of flops required to compute two matrix exponential is $2iQ^3$. The multiplications within each exponent requires Q^2 flops. At each data output a matrix×vector calculation is required, taking Q^2 flops. Hence, the total number of flops, F, required by the analytical method after n pulses is:

$$F_{Analytic} = 2iQ^3 + nQ^2 \tag{2.4}$$

The numerical method is defined as a simple Euler method, $N_k^{t+1} = N_k^t + h * dt$, requiring one flop per nuclide per time-step. A full pulse requires q time-steps to resolve t_Δ and r time-steps to resolve t_θ. If the number of nuclides in the numerical system grows from Q_0 at t=0, to S after n pulses, and $f.Q = \overline{Q}$, where 0<f<1, then the number of flops required by the numerical time-stepping method to compute n pulses is:

$$F_{Numerical} = (f.Q)^2 (q + r)\, n$$

In order to define which method is more computationally efficient, the ratio of $F_{Analytic}$ and $F_{Numerical}$ is defined as:

$$R_F = \frac{F_{Analytic}}{F_{Numerical}} = \frac{2iQ^3 + nQ^2}{(f.Q)^2 (q + r)\, n}$$

The range of n, for which $F_{Analytic}$ is less than $F_{Numerical}$ (the range for which is $F_{Analytic}$ is more computationally efficient), is $R_F < 1$.

$$n > \frac{2iQ}{f^2\,(q+r) - 1} \tag{2.5}$$

Substituting values (which are strongly in favour of the numerical scheme) of i = 200, Q = 100, f = 0.25, q = 20 and r = 20, gives n > 27,000. Assuming that the frequency of the pulse is 6Hz, this suggests that if data outputs are required every 7.4 hrs or less then the numerical scheme is more computationally efficient, else the analytic method is more efficient. Substituting values which are more realistic, suggests that the numerical scheme is only more efficient when data outputs are required every few minutes. When burn-up codes are used in conjunction with flux updating depletion codes, every data output requires at least one lengthy MCNP radiation transport plus many burn-up calculations. Thus, the data outputs for the simulation of an ICF reactor are approximately one every day. This strongly suggests that a time-stepping would be an unwise choice as a numerical method for solving the rate equations for ICF applications.

2.4.2 Equivalent Steady State Approximation

In order to avoid the computational expense of solving the burn-up equation with a pulsed neutron source, the "equivalent steady state approximation (ESSA)" is used. This method approximates the pulses as a constant flux while preserving the total fluence and operation time. Sisolak et al. defined the scenarios [97] for which the ESSA can be used; these scenarios are defined here.

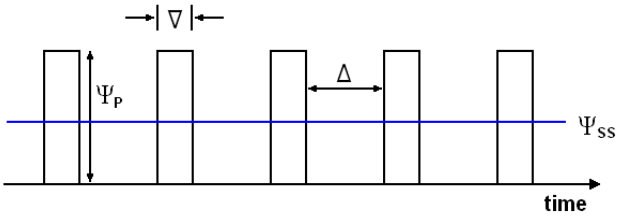

Figure 2.10: Definition of the pulse height, pulse duration, pulse dwell time and equivalent steady state height.

The relation between the equivalent steady state neutron flux, ϕ_{ESS} and the pulsed flux, ϕ_P, is as follows:

$$\phi_{ESS}\,(n\nabla + (n-1)\,\Delta) = \phi_P n\nabla \tag{2.6}$$

Given a stable nuclide with initial concentration $N_1(0)$ and a cross-section σ, which corresponds to a reaction which transmutates the nuclide into an unreactive radioactive daughter nuclide, $N_2(0)$, with a decay constant, λ. After the irradiation of n pulses of ϕ_P, the ratio of the daughter nuclide to the parent nuclide is

$$\frac{N_2^P}{N_1(0)} = \left[\frac{\sigma\phi_p\left(exp^{-\sigma\phi_p\nabla} - exp^{-\sigma\nabla}\right)}{\lambda - \sigma\phi_p}\right]\left[\frac{exp^{-n\sigma\phi_p\nabla} - exp^{-n\sigma(\nabla+\triangle)}}{exp^{-\sigma\phi_p\nabla} - exp^{-\sigma(\nabla+\triangle)}}\right] \tag{2.7}$$

The ratio of the parent to daughter nuclide concentrations after the equivalent steady state flux is

$$\frac{N_2^{ESS}}{N_1^{ESS}} = \left[\frac{\sigma\phi_{ess}\left(exp^{-\sigma\phi_{ess}(n\nabla+(n-1)\triangle)} - exp^{-\lambda(n\nabla+(n-1)\triangle)}\right)}{\lambda - \sigma\phi_{ess}}\right] \tag{2.8}$$

Substituting equation 2.6 and dividing equation 2.8 by equation 2.7 gives:

$$\frac{N_2^{ESS}}{N_2^P} = \left[\frac{n\nabla\left(\lambda - \sigma\phi_p\right)}{\left(n\nabla + (n-1)\triangle\right)\lambda - \sigma\phi_p n\nabla}\right]\left[\frac{exp^{-\sigma\phi_p\nabla} - exp^{-\lambda(\nabla+\triangle)}}{exp^{-n\sigma\phi_p\nabla} - exp^{-n\lambda(\nabla+\triangle)}}\right]\left[\frac{exp^{-n\sigma\phi_p\nabla} - exp^{-\lambda(n\nabla+(n-1))\triangle}}{exp^{-\sigma\phi_p\nabla} - exp^{-\lambda\nabla}}\right] \tag{2.9}$$

For n>>1, eqn 2.9 reduces to:

$$\frac{N_2^{ESS}}{N_2^P} = \left[\frac{\nabla\left(\lambda - \sigma\phi_p\right)}{\left(\nabla + \triangle\right)\lambda - \sigma\phi_p\nabla}\right]\left[\frac{exp^{-\sigma\phi_p\nabla} - exp^{-\lambda(\nabla+\triangle)}}{exp^{-\sigma\phi_p\nabla} - exp^{-\lambda\nabla}}\right] \tag{2.10}$$

The following section defines the scenarios for which the ESS can be used, based on equation 2.10 [97].

1. For $\nabla \gg \Delta$, $\frac{N_2^{ESS}}{N_2^P} \cong 1$ the ESS approximation is valid in this case.
2. For $\Delta \gg t_{1/2}, \nabla \gg t_{1/2}$, and $\lambda \gg \sigma\phi$, $\frac{N_2^{ESS}}{N_2^P} \cong \frac{\nabla}{\nabla+\Delta}$ the ESS approximation underestimates the pulsed result by a factor of $(\nabla+\Delta/\nabla)$. This result is applicable to short lived nuclides within experimental MFE devices due to their intermittent operating schedule.
3. For $\Delta \gg t_{1/2} \gg \nabla$ and $\lambda \gg \sigma\phi_P$, $\frac{N_2^{ESS}}{N_2^P} \cong \frac{1}{\Delta\lambda}$ the error associated with the ESS is applicable to ICF reactors where pulse width is greater than dwell time.
4. For $\Delta \ll t_{1/2}, \nabla \ll t_{1/2}$, and $\lambda \gg \sigma\phi$, $\frac{N_2^{ESS}}{N_2^P} \cong 1$, the ESS approximation is valid in this case.
5. For $\sigma\phi_P\nabla \gg \lambda\left(\Delta + \nabla\right)$, $\frac{N_2^{ESS}}{N_2^P} \cong 1$ the ESS approximation is valid in this case.

2.5 Radiation Transport

The simulation of radiation transport can essentially be dealt with in two ways; stochastic or deterministic methods. The simulation of neutron behavior can be achieved deterministically by solving the transport equation 2.11:

$$\begin{aligned} &\tfrac{1}{v(E)}\tfrac{\partial\varphi\left(r,E,\hat{\Omega},t\right)}{\partial t} + \hat{\Omega}\bullet\nabla\varphi\left(r,E,\hat{\Omega},t\right) + \Sigma_t\left(r,E,t\right)\varphi\left(r,E,\hat{\Omega},t\right) = \\ &\int_{4\pi}\int_0^\infty dE\Sigma_s\left(r,E'\to E,\Omega'\to\Omega,t\right)\varphi\left(r,E',\hat{\Omega},t\right) + S\left(r,E,\hat{\Omega},t\right) \end{aligned} \tag{2.11}$$

Where r is the position vector, v is velocity vector, Ω is the direction unit vector, φ is the angular neutron flux, Σ_t is the macroscopic cross-section, $\Sigma_s(*)$ is the double differential scattering cross-section and S is a source term. The transport equation is used in various branches of physics and frequently solved with deterministic methods due to their ability to achieve a high-order of accuracy. However, complex geometries make the use of deterministic methods unattractive, as such methods require a significantly larger amount of computational time when compared to statistical methods such as Monte Carlo(MC). Deterministic methods are often used to solve the Boltzmann equation for simple geometries (i.e. 1D/2D) often achieve orders of accuracy of $O(\Delta x^2)$ and $O(\Delta x^3)$. However, Monte Carlo (MC) methods only achieve $O(P^{1/2})$ (where P is the number of particles/histories in the MC simulation), hence there is a trade-off between solution accuracy and geometry complexity . Despite the potentially higher order of accuracy that can be achieved with deterministic methods, the MC method tends to be the method of choice for radiation transport due the higher rate of the MC convergence on the true solution when compared to deterministic methods.

The Monte Carlo method can be thought of as a numerical experiment where particle events are followed from their creation to their termination, via events such as absorption, scatter and escape. The outcome of a reaction is determined by randomly sampling probability density functions (pdf's). The MC method is conceptually quite simple and realistic, as the computational method involves tracking many particles in space, as they interact with their surroundings until the particles are terminated. A small number of the possible interactions include neutron scatter, neutron capture, photon scatter, photon capture, neutron multiplication & fission. Each particle being tracked can create further particles which also need to be tracked.

The physical assumptions upon which MC methods are founded are [98]:

- Static, homogeneous medium

- Time-independent
- Markovian – next event depends only on current (r,v,E), not on previous events
- Particles do not interact with each other
- Relativistic effects are neglected
- No long-range forces (particles fly in straight lines between events)
- Material properties are not affected by particle reactions

2.5.1 MCNP

Numerous Monte Carlo radiation transport codes exist that could be applied to fusion blanket modelling, such as MCNP, Fluka, Serpent and Geant. However, MCNP was chosen mainly due to its long-term presence in the nuclear industry and the extensive amount of testing/benchmarking that this code has been subjected to.

MCNP [98] is a general-purpose Monte Carlo N–Particle code that can be used for neutron, electron and photon transport, either individually or as coupled systems in a 3D geometry comprised of a set of user defined cells.

The operation of the MCNP program depends on the user defined input file which contains information regarding the radiation transport problem. The major components of the input file are [98]:

- Geometry specification
- Description of materials and selection of cross-section evaluations
- Location and characteristics of the neutron, photon, or electron source
- Type of answers or tallies desired
- Variance reduction techniques used to improve efficiency

2.6 Summary

This chapter covered the physics and technology of reactor blankets. The main functions of the blanket, such as tritium breeding, heat conversion, radiation shielding and the transmutation of waste were outlined, and the ways in which tritium is produced and lost within the blanket (and peripheral systems) were addressed. Neutron multipliers are an absolute requirement for a

tritium breeding blanket, as without them the losses in the system would cause a TBR < 1. Many designs exist which incorporate either berylium or lead in dry, wetted and liquid wall designs; none of which have attributes which make them a clear choice for application in a commercial fusion reactor. The classification of nuclear waste was discussed and the routes for disposal of materials for some reactor concepts were described. The liquid breeder concept is a promising technology due to the relatively low volume of nuclear waste that it produces and the potential online control of tritium production. The latter part of this chapter described burn-up codes and the neutron transport code, MCNP, both of which are powerful tools in the modeling of tritium production within blankets. However, both of which have their drawbacks: MCNP is able to resolve neutron properties within 3D space, but not temporally, and burn-up codes (such as FISPACT) can model transmutation and decay with respect to time, but with no spatial resolution.

At the heart of all fusion reactor depletion simulations is the calculation of reaction rates. These reaction rates are required in order to advance nuclide compositions with time, thus enabling the calculation of heating, power output, radioactivity, materials damage, gas production and many other attributes as a function of time. Due to the amount of nuclides to be tracked and the complexity of reactor components, overall the calculation of reaction rates can form the majority of computation time required for depletion analysis. Hence, an efficient method for calculating reaction rates is vitally important in the study of materials composition. The next chapter describes one of the most efficient methods for calculating reaction rates, the multi-group binning method, and the procedure used to optimize the energy binning structure, which it requires to operate.

CHAPTER 3

OPTIMISATION OF ENERGY BINNING STRUCTURE

Monte-Carlo (MC) codes are powerful tools when used to model neutron transport. The majority of MC codes utilize point-wise cross-section data which have been compiled directly from ENDF data. MC codes are computationally expensive due to a large proportion of the computational time being taken up by trudging through masses of point-wise cross-section data in order to calculate nuclear reaction rates. An alternative to calculating reaction rates, via the direct access of point-wise data, is the multi-group binning method. The optimization of this method is the focus of this chapter.

3.1 Theory

The performance, economic viability and safety of a fusion energy device are partly reliant on the material composition and its evolution with time. The material composition will change during the reactor's lifetime due to transmutation, activation and nuclear decay, which will have an effect on radiation protection, radioactive waste disposal and reactor performance calculations. The modelling of material properties within a radiation environment is often accomplished using Monte Carlo (MC) codes.

There are essentially two ways of calculating reaction rates within MC codes: multi-group binning (MGB) and Monte-Carlo estimators (MCE). Both the MGB and MCE methods are founded on the following definitions of particle flux. The average scalar particle flux, ϕ_V, within a cell of volume, V, given an angular vector flux, $\psi\left(\overrightarrow{r}, \hat{\Omega}, E, t, \right)$ is given by

$$\phi_V = \frac{1}{V} \int \int \int \int \psi\left(\overrightarrow{r}, \hat{\Omega}, E, t\right) dE\, dt\, d\Omega\, dV \tag{3.1}$$

Substituting the definition of the angular flux with its definition, $\psi = v\, n\left(\overrightarrow{r}, \hat{\Omega}, E, t\right)$, and integrating over the entire solid angle gives

$$\phi_V = \frac{1}{V} \int \int \int v\, N\left(\overrightarrow{r}, E, t\right) dE\, dt\, dV \tag{3.2}$$

The reaction rate, R, can then be calculated by substituting the microscopic cross-section into the reaction rate definition.

$$R = \frac{N_a}{V} \int \int \int \sigma v\, N\left(\overrightarrow{r}, E, t\right) dE\, dt\, dV$$

where N_a is the atomic number density. The Monte-Carlo estimator approach is the simplest to set up and most accurate method for calculating reaction rates within MCNP, however it is computationally expensive. For each reaction, a cross-section is found that corresponds to that energy of the particle, by searching through finely meshed ($\sim 10^3 - 10^5$ data points) point-wise cross-section data tables. After the search, an interpolation via Legendre polynomials is performed in order to calculate the cross-section at the exact energy of the reaction. A typical MCNP simulation requires several million or billions of particles to be tracked, thus the MCE approach to calculating reaction rates may result in a simulation time in the order of weeks/months for complicated geometries such as ITER.

The MGB method is based on the principle of substituting $N\left(\overrightarrow{r}, E, t\right) = \int n\left(\overrightarrow{r}, E, t\right) d\Omega$ into equation 3.1 and changing the integrating variable from velocity to position, $ds = vdt$. This allows the particle flux to be given in terms of the particle track length.

$$\phi_V = \frac{1}{V} \int \int \int N\left(\overrightarrow{r}, E, t\right) dE\, ds\, dV$$

Thus, for every particle which travels through and reacts within a cell, c, the distance travelled between subsequent reactions (track length), ds, is recorded in an energy bin, i, defined by the interval [E, E + dE]. At the end of the particle simulation, the track lengths are calculated for each energy bin within each cell.

$$\phi_c^i = \sum \frac{W^c T_l^i}{V_c}$$

Where W is a particle weighting used for improving statistics. The effective cross-section of a reaction, r, is given by

$$\overline{\sigma_r} = \frac{\sum \sigma_{i,r} \phi_i}{\sum \sigma_{i,r}}$$

The reaction rate can be calculated by convolving the multi-group cross-section and the neutron energy spectrum.

$$R = N_a \phi \frac{\int_0^\infty \sigma\left(E\right) \phi\left(E\right) dE}{\int_0^\infty \phi\left(E\right) dE} \tag{3.3}$$

This continuous energy definition of the reaction rate must be discretized in order to reduce the computational cost of the reaction rate calculations and also due to the discrete nature of the cross-section data. Hence, the reaction rate, as calculated by the multi-group method, is defined as:

$$R = N_a \phi \frac{\sum_{g=1}^{N} \sigma(E_g)\phi(E_g)}{\sum_{g=1}^{N} \phi(E_g)} \tag{3.4}$$

where $\sigma(E_g)$ and $\phi(E_g)$ are the average cross-section and spectra defined within the energy range E_g and E_{g-1}. E_0 is the minimum energy at which the cross- section data begins and E_N is the maximum energy at which the cross-section data is tabulated.

The discretisation of the energy grid and calculating the reaction rates outside of the MC routine significantly reduces the computation time of calculating reaction rates. However, it is the unionisation of the energy grids for all reaction rates which makes the largest difference to the computation time, as the unionisation allows each reaction rate to be calculated within the same energy loop within the code. The objective of this work is to produce an energy binning structure which results in a multi-group reaction rate definition that is statistically indistinguishable from the point-wise reaction rate. Given that the nuclear cross-section uncertainties are approximately 5%, the energy structure chosen must ensure the following requirement is fulfilled:

$$\left| 1 - \frac{\overline{\sigma_{MG}}}{\overline{\sigma_{MCE}}} \right| < 0.05 \tag{3.5}$$

3.2 Modeling

The optimum group structure was found using three phases of modeling, with each of the phases of calculation improving the convergence of the optimum solution in the $\{N_{slow}, N_{mid}, N_{fast}\}$ domain. In order to ensure the optimized structure to be found is capable of meeting the criterion set in equation 3.5 for all reactions, all three models focus on the reaction rates which require the most resolved energy structure. These correspond to reaction rates with substantial resonance

regions within the associated cross-section such as Ni-58 (n,γ), Cr-52 (n,γ), W-186 (n,γ), Fe-56 (n, n') and O-16 (n,α). Other fusion relevant materials, such as FLiBe and LiPb, are included in the model in order to create a generic fusion blanket neutron spectrum.
In order to match the neutronic processes taking place within a material which is under irradiation, the energy structure is to be split into three distinct regions:

- *Slow region* - Comprises of N_{slow} equal energy intervals in the range $E_0 <$ E $<$ 0.1 eV.
- *Mid region* - Comprises of N_{mid} equal lethargy intervals in the range 0.1 eV $<$ E $<$ 2 MeV.
- *Fast region* - Comprises of N_{fast} equal energy intervals in the range 2 MeV $<$ E $< E_N$.

The energy binning structure has been defined as N_{slow}: N_{mid} : N_{fast}. Each of the model geometry definitions described in subsequent sections were defined using MCNP [98] syntax. In conjunction with the VESTA [99] depletion code, these geometry definitions were then used to perform multiple transport calculations. For each model, the point-wise method was used to determine reaction rates and many energy structures were utilized to compute the reaction rates using the multi-group method. A comparison of the point-wise and multi-group reaction rates was then made using equation 3.5. A simple preliminary calculation was performed in order to produce a theoretical estimate of N_{mid}, thus reducing the range of the search space during transport calculations.

3.2.1 Preliminary Calculations and simulations

In order to make a first estimate of the distribution of the reaction rate as a function of energy, a MCNP simulation of the spherical model specified in figure 3.1 and table 3.1 was performed. 10^7 particles were used in the MCNP simulation ensuring all statistical checks were met.
The preliminary results shown in table 3.2 suggest that the optimization of the mid-energy region will result in the most significant overall gain in optimization. Despite the relatively low proportion of reactions occurring in the fast region, this region will require a significant number of energy bins in order to accurately integrate near the threshold regions of endothermic reactions. A basic preliminary calculation was used to broadly define the number of groups that are needed in the mid-energy region.
The mid energy group, which is divided into N_{mid} equal lethargy groups, is defined as:

$$E_k = E_{g-1} exp\left(\frac{k}{n_{mid}} ln\left[\frac{E_g}{E_{g-1}}\right]\right) \tag{3.6}$$

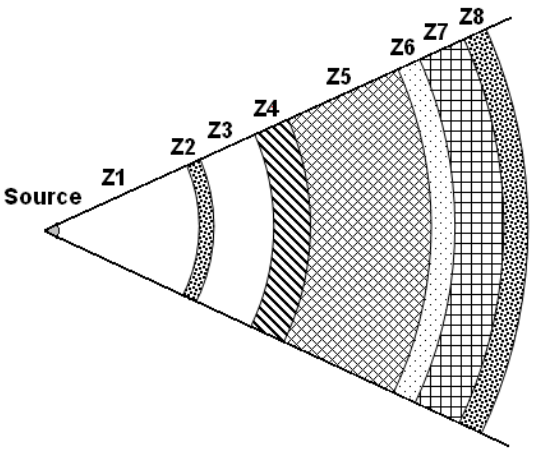

Figure 3.1: Phase 1 model - A spherical model containing concentric shells of materials specified in table 3.1 (not to scale).

Cell	Material	Radial width(cm)	Nuclide	Fraction*
1	void	580	-	-
2	LiPb	5	^{6}Li	0.03400
			^{7}Li	0.13600
			^{204}Pb	0.01162
			^{206}Pb	0.20003
			^{207}Pb	0.18343
			^{208}Pb	0.43492
3	FLiBe	5	^{19}F	0.57142
			^{9}Be	0.14285
			^{6}Li	0.05714
			^{7}Li	0.22857
4	Tungsten	5	^{186}W	1.000000
5	Nickel	5	^{58}Ni	1.000000
6	Chromium	5	^{52}Cr	1.000000
7	Beryllium	5	^{9}Be	1.000000
8	Oxygen	5	^{16}O	1.000000
11	void	-	-	-

Table 3.1: Phase 1 model geometry and material specifications. *Nuclide proportions are specified by number (as opposed to mass) fraction.

Material	Reaction Rate %		
	Slow	Mid	Fast
O-16	1.993	94.917	3.0898
Ni-58	0.10515	98.56147	1.33351
Cr-52	0.47922	96.8701	2.6507
W-186	0.0001	94.5205	5.4792

Table 3.2: Total reaction rate percentage breakdown for materials present in model 1.

Material	Reaction Rate %		
	Slow	Mid	Fast
O-16	5.5825	92.0326	2.3853
Ni-58	2.1554	96.1802	1.6643
Cr-52	0.0035	95.9482	4.0481
W-186	9.8486	81.932	8.2199
Fe-56	0.0004	93.6996	6.3000

Table 3.3: Total reaction rate percentage breakdown for materials present in model 2.

Where $k = 1..n_{mid}$, E_{g-1} is the lower bound of the energy group, E_g is the upper bound of the energy group and k is an index defining the boundaries of the interval within the group structure. Rearranging equation 3.6 for n_{mid} gives:

$$n_{mid} = \frac{k.\, ln\left[E_g/E_{g-1}\right]}{ln\left[E_k/E_{g-1}\right]} \tag{3.7}$$

The lethargy spacing of the energy intervals result in the final energy interval, $k = n_{mid}-1$, being the smallest energy interval within the specified group. Thus, in order to accurately integrate under the cross-section, the energy range of the narrowest resonance peak should specify the energy range of the final energy interval. Setting $k = n_{mid} - 1$ and $E_k = E_g - \triangle E$ in equation 3.7 gives:

$$n_{mid} = \left(1 - \frac{ln\left[\{E_g - \triangle E\}/E_{g-1}\right]}{ln\left[E_g/E_{g-1}\right]}\right)^{-1} \tag{3.8}$$

Averaging over the very fine structure found within the resonance regions, the macro-structure of the (n,γ) cross-sections oscillations in the region near 2 MeV for isotopes of interest are: 10 keV for Ni-58, 20keV for Cr-52, 50 eV for W-186, 6 keV for Fe-56 and 20 keV for O-16. A 50 eV resolution would require several million bins, which is likely to negate the efficiency gains achieved by using the MG method. Substituting $E_{g-1} = 0.1\,eV$, $E_g = 2\,MeV$ and $\triangle E = 10KeV$ suggests that $n_{mid} > 3354$.

The ideal group structure was found using three phases of optimization; Thus, the $n_{mid}^{initial} > 3354$ criterion provided a starting point for the $n_{mid}^{optimum}$ search space in the first phase of optimization.

Material	Reaction Rate %		
	Slow	Mid	Fast
O-16	0.00100	96.2355	3.7633
Ni-58	0.00231	97.5840	2.4137
Cr-52	0.00096	91.9316	8.0675
W-186	0.00189	95.7883	4.21008
Fe-56	0.00243	94.8596	5.13820

Table 3.4: Total reaction rate percentage breakdown for materials present in model 3.

The upper energy region is divided into equal energy bins, hence the calculation of the number of bins required is trivial, giving $n_{fast} \sim 1000$.

3.2.2 Phase 1 Model

The spherical model used to create a generic fusion neutron spectrum has been designed using fusion relevant materials. Conceptually, a sphere with a 14.1MeV neutron source is a good representation of a fusion reactor and is acceptable for this study given that the this study is interested in the relative differences in reaction rates rather than the absolute values. Each zone within the sphere will have a unique neutron spectrum which will be utilised to calculate reaction rates in that particular zone. Hence, the material in zone 8 will be subjected to a neutron spectrum which is softer than the spectrum of zone 2. In order to test the sensitivity of reaction rates to spectrum changes the materials will be placed in different zones in later stages of modelling. The low-, mid-, high-energy contributions to the reaction rate will change from being dominated by mid-high energy regions in zone 2 to being dominated by low-mid energy regions in zone 8. Hence, many variations of spectra will be tested in order to ensure that the final optimised energy structure is suitable for all fusion applications.

The VESTA depletion code (to be described in Chapter 4) was used to calculate the reaction rates within cells 4, 5, 6 and 8 of the model specified in figure 3.2 and table 3.1.

A first wall radius of 580 cm was chosen as it produces a first wall flux of approximately $5\text{MW}/m^2$, which is around the upper limit of the FW loading. 5-8cm material thicknesses produce a combination of harder and softer neutron spectra to be convolved with cross-sections. The total width of the blanket was considered. Thus, a combination of 5 and 8 cm width shells produced overall blanket widths which fall into the lower and upper range of realistic blanket thicknesses. ITER and DEMO walls will be thicker than the walls in the spherical model. However, 72 cm radial thickness was considered to be a large enough, due to the change in thermal flux at larger thicknesses having no significant further affect on the reaction rates. Cross-sections

with significant thermal regions, such as $^6Li(n,\alpha)^3H$ do not require fine grids because their cross-sections do not exhibit significant resonances.

Tables 3.2, 3.3 and 3.1 show that the majority of the reactions occur within the mid-energy range, thus increasing the number of bins in the low and high energy regions will make little difference to the accuracy of the MGB reaction rate calculations. The theoretical number of mid-energy groups, as calculated in section 3.1, should be a minimum of 3354. Therefore, the neutron spectra to be tested in the initial search stage are 4000:N:4000, where N is 2000, 4000, 8000, 16000 and 32000. 4000 bins were chosen for the low and high energy regions in order to ensure that the high accuracy in these ranges, resulting in the search being constrained to the mid-energy region.

3.2.3 Phase 2 Model

In order to ensure MG reaction rates are calculated using a broad range of (fusion relevant) neutron spectra the positions of materials present in phase 1 of the modelling were altered. In addition to this, some other fusion relevant materials have been added to the model. The phase 2 model is specified by table 3.5. The neutron spectra formats chosen to be implemented in the second phase of optimisation are 500:N:1000, where N is 4000, 8000, 12000, 16000 and 20000. The VESTA default 43000 energy structure was also implemented for comparison.

3.2.4 Phase 3 Model

The heterogeneous material structures were transformed to a single homogeneous structure for the third stage of optimization. The neutron spectrum within this homogeneous material (specified in table 3.6) can be considered to be a generic fusion spectrum. The neutron spectra formats were the same as those used in phase 2.

3.3 Results and discussion

The error ratios of the phase 1 search for the optimum number of mid-energy groups, shown in figure 3.2, indicates that at least 20,000 bins are required in order to achieve the target of $> 95\%$ accuracy. Due to its larger average cross-section and finely structured resonance when compared to nickel and chromium, tungsten benefits the most from higher number of bins. The binning structure of the first phase of optimization was reduced from 4000:N:4000, for N [2000, 32000], to 500:N:1000 for the second phase.

The changing of materials positions and the addition of iron, water and oxygen at this stage

Cell	Material	Radial width(cm)	Nuclide	Fraction*
1	void	580	-	-
2	LiPb	8	^{6}Li	0.03400
			^{7}Li	0.13600
			^{204}Pb	0.01162
			^{206}Pb	0.20003
			^{207}Pb	0.18343
			^{208}Pb	0.43492
3	FLiBe	8	^{19}F	0.057143
			^{9}Be	0.228571
			^{6}Li	0.142857
			^{7}Li	0.571429
4	Tungsten	8	^{186}W	1.000000
5	Nickel		^{58}Ni	1.000000
6	Chromium	8	^{52}Cr	1.000000
7	Beryllium	8	^{9}Be	1.000000
8	Oxygen	8	^{16}O	1.000000
9	Iron	8	^{56}Fe	1.000000
10	Water	8	^{1}H	0.66667
		8	^{16}O	0.33333
11	void	-	-	-

Table 3.5: Phase 2 model geometry (figure 3.1) and material specifications. *Nuclide proportions are specified by number (as opposed to mass) fraction .

Cell	Material	Radial width(cm)	Nuclide	Fraction*
1	void	580	-	-
2	Mix	72	^{186}W	0.020455057
			^{58}Ni	0.006818352
			^{52}Cr	0.006818352
			^{9}Be	0.057955994
			^{16}O	0.022727818
			^{56}Fe	0.020455057
			^{19}F	0.231823977
			^{204}Pb	0.006600165
			^{206}Pb	0.113648296
			^{207}Pb	0.104218515
			^{208}Pb	0.247110723
			^{6}Li	0.034091761
			^{7}Li	0.081820227
			^{1}H	0.045455705
3	void	-	-	-

Table 3.6: Geometry (figure 3.1) and material specifications of the phase 3 homogeneous model. *Nuclide proportions are specified by number (as opposed to mass) fraction .

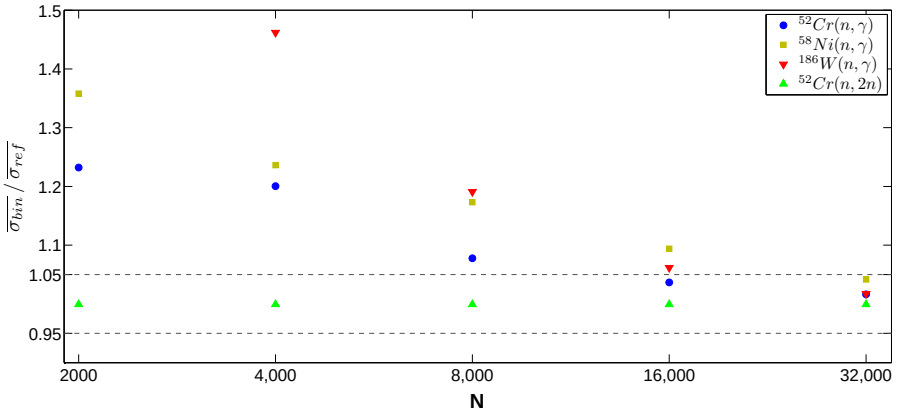

Figure 3.2: Phase 1- The ratio of (n,γ) reaction rates calculated by the binning method, implementing an energy structure of 4000:N:4000, and the point-wise method for Cr-52, Ni-58 and W-186.

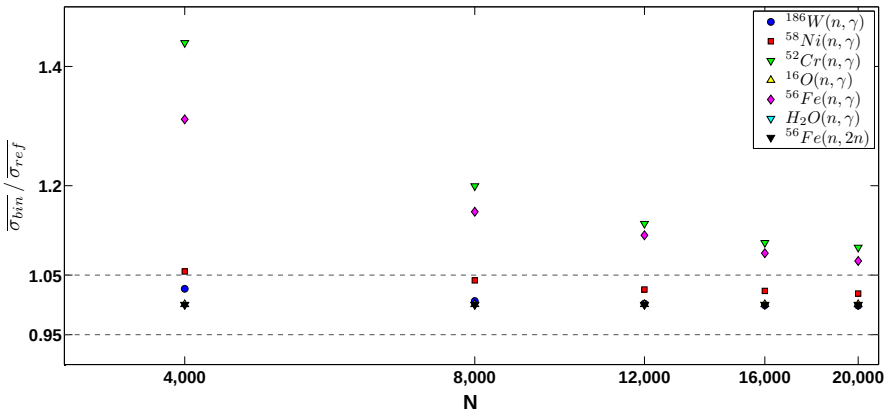

Figure 3.3: Phase 2- The ratio of (n,γ) reaction rates calculated by the binning method, implementing an energy structure of 500:N:1000 for Cr-52, Ni-58 and W-186, Fe-56, O-16 and H_2O.

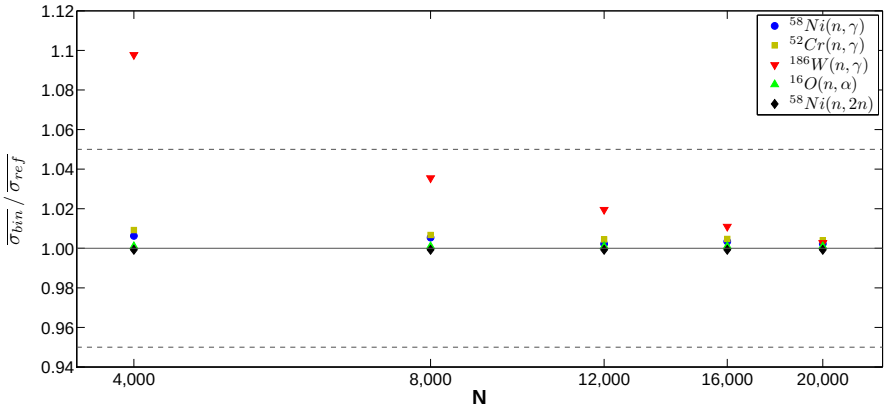

Figure 3.4: Phase 3- The ratio of (n,γ) reaction rates, in the homogeneous material, calculated by the binning method, implementing an energy structure of 500:N:1000 for Cr-52, Ni-58 and W-186, Fe-56, O-16.

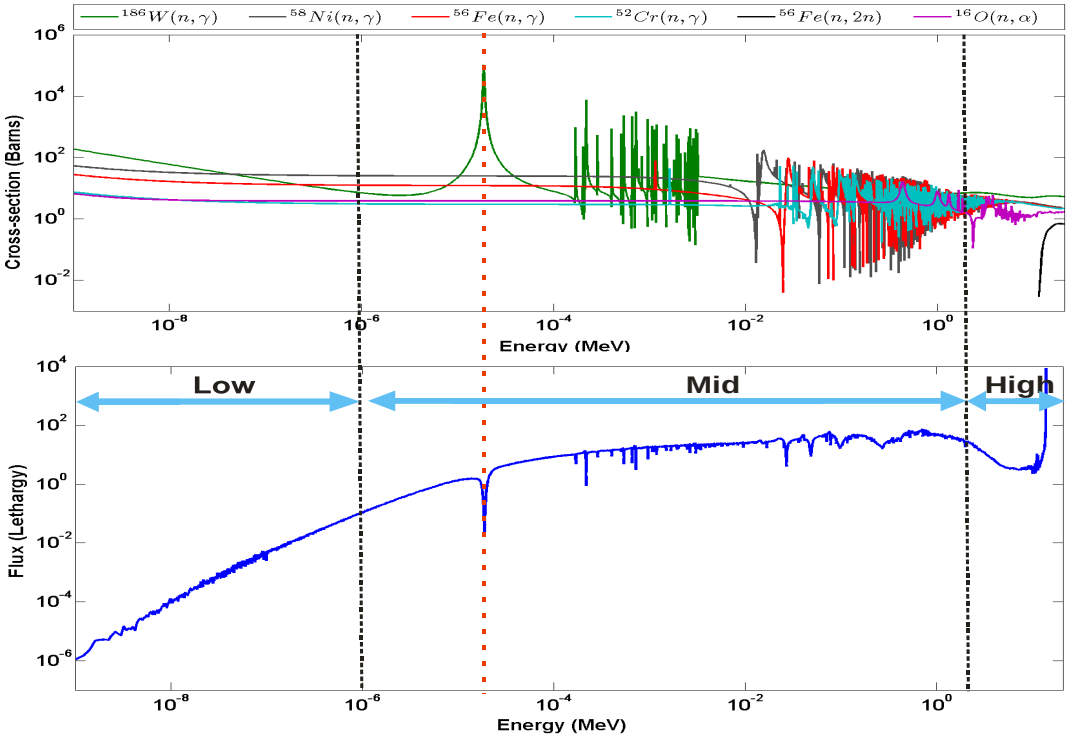

Figure 3.5: Comparison of MCNP generated neutron spectra within homogeneous cell of Phase 3 and ENDF nuclear cross-sections. The black dashed lines correspond to the boundaries of the low-mid and mid-high energy regions of the group structure used to tally the neutron spectra.

significantly altered the rates at which the error ratios converge to zero. Figure 3.3 shows that Fe-56 and Cr-52 require more than the 20,000 bins as suggested in phase 1, however this is likely to be due to the increased thickness of the FLiBe and LiPb.

Figure 3.3 also shows that the relatively low number of bins in the high-energy range has resulted in a slow rate of convergence for Fe-56(n,γ) and Cr-52(n,γ) reactions.

For phase 2, the Fe-56 and Cr-52 rate of convergence is very low at high number of bins, suggesting that both Fe-56 and Cr-52 are unlikely to converge to with 95%. This, along with the data in table 3.3, strongly suggests that the binning structure of the high energy region is the limiting factor. A comparison of Cr-52 in phase 1 and 2 clearly illustrates the effect of breeding blanket materials on the rate of activation. The radial width of the LiPb and FLiBe tritium breeders in phase 2 are double that of phase 1, thus the spectrum which is convolved with the Cr-52(n,γ) cross-section is softer and has a higher neutron population in the Cr-52(n,γ) resonance region. As a result, the under-resolved resonance region has a greater contribution to the reaction rate, which then leads to higher error.

The homogeneous material utilized in the final stage of optimization produces a generic fusion neutron spectrum which reduces the effect of the material positioning on the neutron energy

z (cm)	***Experiment***		***multi-group***		***Error***	
	Rate	***Error***	***Rate***	***Error***	E/M	***Error***
$^{58}Ni(n,2n)^{57}Ni$						
5.0	1.49E-5	4.0	1.49E-5	9.11E-8	0.998	0.041
15.0	8.15E-7	4.5	1.07E-6	1.13E-8	0.761	0.061
25.0	7.19E-8	5.5	6.05E-8	1.17E-9	1.189	0.049
$^{27}Al(n,\alpha)^{24}Na$						
5.0	4.45E-5	4.0	4.58E-5	2.79E-7	0.972	0.042
15.0	2.72E-6	5.0	2.88E-6	3.08E-8	0.945	0.054
25.0	2.53E-7	6.0	2.29E-7	4.53E-9	1.105	0.057
35.0	2.78E-8	6.5	2.43E-8	9.82E-10	1.144	0.067
$^{56}Fe(n,p)^{56}Fe$						
5.0	4.56E-5	5.0	4.48E-5	2.69E-7	1.017	0.050
15.0	2.79E-6	5.0	2.84E-6	2.99e-8	0.981	0.052
25.0	2.62E-7	5.5	2.20E-7	4.31E-9	1.190	0.049
35.0	2.91E-8	6.4	2.11E-8	7.96E-10	1.382	0.053
$^{58}Ni(n,p)^{58}Co$						
5.0	1.58E-4	4.5	1.69E-4	1.03E-6	0.935	0.049
15.0	1.16E-5	5.5	1.43E-5	1.52E-7	0.811	0.069
25.0	1.14E-6	5.5	1.16E-6	2.24E-8	0.985	0.059
35.0	1.35E-7	5.5	1.22E-7	4.88E-9	1.107	0.061
$^{197}Au(n,\gamma)^{198}Au$						
5.0	6.23E-4	4.0	6.87E-4	5.22E-6	0.907	0.045
15.0	2.98E-4	4.0	2.92E-4	4.15E-6	1.019	0.042
25.0	1.03E-4	4.0	9.01E-5	2.27E-6	1.143	0.041
35.0	2.84E-5	5.5	2.50E-5	1.14E-6	1.137	0.060
$^{55}Mn(n,\gamma)^{56}Mn$						
5.0	1.67E-5	5.0	2.83E-5	2.04E-7	0.589	0.086
15.0	8.74E-6	5.0	1.25E-5	1.61E-7	0.700	0.074
25.0	3.30E-6	5.5	3.93E-6	9.54E-8	0.840	0.072
35.0	1.04E-6	6.4	9.61E-7	3.88E-8	1.082	0.070

Table 3.7: Activation reaction rates measure experimentally [100] compared with reaction rates calculated using point-wise and multi-group methods.

distribution for any one material. Figure 3.4 shows that tungsten requires more than 6000 bins, while the other materials have converged to within 5% error with less than 4000 bins.

The dominance of the mid-energy region on the reaction rate can be clearly explained by figure 3.5. The neutron spectra tallied within the homogeneous material falls away faster in the thermal regions than the rise of the cross-sections in the same region. Thus, the convolved spectra and cross-section results in a relatively low effective cross-section value in the thermal region. The major resonances of tungsten (5 eV- 35 eV), oxygen (280 keV - 15 MeV), nickel (10 keV - 6 MeV), iron (200 keV - 8 MeV) and chromium (20 keV - 7.5 MeV) are also evident in the neutron spectrum.

All three stages of the MCNP simulations used 10^7 particles, both for the multi-group binning

and the point-wise estimators. This ensured the statistical checks were met. However, when the multi-group binning model is utilised an increase in the number of bins within an energy range decreases the bins size. Hence, fewer particles are tallied per bin which results in larger uncertainties per bin. Nevertheless, the larger uncertainties do not increase the total reaction rate uncertainty as the uncertainties are re-normalised in the convolution process.

3.3.1 Benchmarks

The evaluation of the optimised energy format has been performed by comparing reaction rates computed with the MG method with empirical reaction rates from the FNG - W [100] SINBAD[1] benchmarks. An approximate FNG[2] source description [101], based on the beam specified in [102] and defined using SDEF (MCNP source definition) cards, was implemented instead of the SINBAD source. This benchmark study measured reaction rates of many materials (in the form of thin foils, which were subject to 14MeV neutron irradiation) in order to validate cross-sections for the European Fusion File (EFF).

The results based on the 10^{-11}eV : 0.1 eV: 2 MeV: 19.6 MeV macro energy grid structure suggest that a group structure of 1000:16,000:1000 is optimal. However, an increase of the low-mid boundary from 0.1 eV to 1 eV, whilst maintaining the same lethargy range in the mid group, reduces the number of bins in the mid range by approximately 2000. Thus, the optimization found the energy binning format which is appropriate for MC fusion modelling to be 1000:14,000:1000 with an energy grid specified by 10^{-11}eV : 1 eV: 2 MeV: 19.6 MeV. This optimum format, named FOMG (Fusion Optimised Multi-Group), will be evaluated using a SINBAD (Shielding Integral Benchmark Archive Database) benchmark in this section.

A 16,000 bin structure has significantly more data points than the PENDF data files accessed by neutron transport codes, such as MCNP, during run time. For example, the number of point-wise data components are Cr-52 (10,938), Fe-56 (10,097), H-1 (200), Ni-58 (15,962), O-16 (976) and W-186 (8,786). The significant decrease in computational power is achieved by only accessing each of the PENDF (Pointwise Evaluated Nuclear Data File) files once at the end of the radiation transport simulation. As opposed to accessing and interpolating data from these files for every particle interaction that occurs. In addition to this, the FOMG structure is intended to be used as a unionised grid. Thus, the effective cross-section for each material can be calculated within the same loop of the code.

[1] Shielding Integral Benchmark Archive and Database
[2] Frascati Neutron Generator

Comparisons of experimentally found and VESTA (multi-group) reaction rates, computed using JEFF 3.1 cross-sections, were attained using the ratio of experimental (E) and multi-group (M) reaction rates, defined as E/M. The agreement of experimentally found and multi-group reaction rates for foils situated close to the neutron source are generally convincing due to many E/M ratios being within the bounds of 5% experimental error. E/M values for foils further away from the neutron source (25 cm +) are generally less satisfactory due to the discretised nature of the SDEF neutron source rather than the method of reaction rate calculation.

3.4 Conclusions

The multi-group group method for calculating reaction rates within Monte-Carlo codes can significantly reduce computational expense when compared to the standard point-wise estimator approach. This chapter outlined a method used to optimise the energy binning structure required by the multi-group binning method in order to further reduce the computational cost. The optimisation aimed to minimize the number of energy bins while ensuring the accuracy of the method was not compromised. Thus, the binning structure to be considered optimal is the structure with the least number of bins whilst achieving an accuracy of >95%. The method for optimizing the structure focussed on nuclides and reaction rates which are particularly relevant to fusion (such as Ni-58 (n,γ), Cr-52 (n,γ), W-186 (n,γ), Fe-56 (n, n') and O-16 (n,α)) which also have fine structure within their cross-section. Thus, these reaction rates are the most difficult to compute with the multi-group method.

The FOMG structure was implemented in order to calculate reaction rates which were measured during the SINBAD FNG-W benchmark experiment. Overall, the agreement of the experimental and multi-group reaction rates was tolerable. However, the user-defined neutron source implemented in the modelling introduced some inaccuracy to the measurement.

The optimal binning structure, named FOMG (Fusion Optimised Multi Group) is split into three distinct sections.

- The low-energy region is defined in the range $10^{-5} eV \leq E_L < 1\, eV$ with 1,000 equally spaced energy bins, each of which have an energy width of 1 meV
- The mid-energy group is defined in the range $1\, eV \leq E_L < 2\, MeV$ with 14,000 equal lethargy bins, each of which have a lethargy width of 1.036×10^{-3}.
- The high-energy group is defined in the range $2\, MeV \leq E_H < 20\, MeV$ with 1,000 equally spaced energy bins, each of which have an energy width of 17.6 keV.

A 16,000 bin structure has significantly more data points than most, but not all, of the directly accessed PENDF data files accessed by neutron transport codes, such as MCNP, during run time. For example, the number of some point-wise data components are Cr-52 (10,938), Fe-56 (10,097), H-1 (200), Ni-58 (15,962), O-16 (976) and W-186 (8,786). The significant decrease in computational power is achieved by only accessing each of the PENDF files once at the end of the radiation transport simulation. As opposed to accessing and interpolating data from these files for every particle interaction that occurs. In addition to this, the FOMG structure is intended to be used as a unionised grid. Thus, the effective cross-section for each material can be calculated within the same loop of the code. An equivalent method, applied to a LWR system, led to an energy binning structure of 43,000 groups.

Examples of fission and fusion depletion calculations exist which use a low number of bins (VITAMIN-J [175 bins], WIMS [69 bins]). However, these often include an additional weighting parameter for each energy bin. These weighting parameters are optimised over a number of reaction cross-sections or for a set of important reactions. Thus, binning structures with a relatively low number of bins will undoubtedly suffer from self-shielding/dilution effects when calculating reaction rates which involve many cross-sections with significant resonances.

While the FOMG structure can be applied directly to the modelling of any fusion device, the primary component of this paper is the description of a method which can be used to optimise the energy binning structure. Thus, the binning structure provided can be used as a starting point for further optimisation given a specific reactor geometry.

It is worth noting that the FOMG group structure could be used by a modern inventory code such as EASY-II [103].

3.5 Summary

This chapter has described and implemented a method used to optimise the multi-group binning method used to calculate reaction rates using Monte Carlo (MC) simulation. This method involved preliminary analytical calculations and MC simulations. These were followed by three stages of successive optimisation which lead to the creation of the FOMG (Fusion Optimised Multi-Group) energy structure with 16,000 bins. This structure can be used to calculate reaction rates within materials irradiated by neutrons generated by fusion reactions. This method could be utilised in order to further optimise the energy structure for particular reactor geometries.

The backbone of this thesis is the computation of tritium inventory and nuclide depletion within reactor models. The next chapter will introduce the concept of a depletion linker code, which

couples a burn-up code with a particle transport code. The efficient calculation of reaction rates, via methods such as MG, is vital to the calculation of tritium production and burn-up of nuclides to be finely resolved both temporally and spatially. The theory of the FATI depletion code will be outlined and some of the functionality will be described. The final part of the chapter is dedicated to benchmarking of the FATI code with the VESTA depletion code, which has been thoroughly tested and bench-marked.

CHAPTER 4

FATI

In the first part of this chapter, the general theory behind depletion codes will be addressed which is followed by the description and functionality of the FATI (Fusion Activation and Transport Interface) depletion code. The final part of the chapter is dedicated to benchmarking the FATI code via comparisons of nuclide inventories with a well-tested and benchmarked depletion code, VESTA. The production of the FATI code and its application to the simulation of fusion blanket behavior forms the centerpiece of this thesis.

4.1 Depletion code theory

Radiation transport codes and burn-up codes are important tools within reactor analysis, however they are both to some extent limited. Burn-up codes such as FISPACT and ORIGEN are able to calculate nuclide inventories with time, but with no spatial dependence, for a given initial nuclide composition and specified neutron source. On the other hand, radiation transport codes have the ability to resolve reaction rates and neutron spectra spatially, but not temporally. The primary function of a depletion code is the calculation of nuclide inventories with time and space (reactor component) by combining the functionalities of burn-up and radiation transport codes. This is achieved by solving radiation transport and burn-up problems in a manner which is similar to solving simultaneous differential equations. Firstly, a radiation transport run is performed to calculate reaction rates and neutron fluxes within each component of the reactor. For each reactor component, a set of reaction rates and/or fluxes are passed to the burn-up code to advance the nuclide composition with time as a result of neutron irradiation. Following burn-up runs for selected components in the reactor, the new nuclide compositions are then passed back to the radiation transport code and the cycle is repeated until a required period of time has elapsed. The coupling can be performed by utilizing time-stepping routines with a specified order of accuracy, depending on the computational power and accuracy required. The

simplest time-stepping routine for coupling the transport and burn-up equations is the forward Euler method.

$$\underline{\Phi}_c^n = \mathbf{M}\left(\underline{N}_c^n\right)$$

$$\underline{N}_c^{n+1} = \mathbf{B}\left(\underline{\Phi}_c^n\right)$$

Where the operator, M, is the Monte Carlo operator which returns a set of reaction rates and/or neutron spectra, $\underline{\Phi}_c^j$, given a specified nuclide set, $\underline{N}_c^j$, relating to cell, c. The operator, B, is the burn-up operator, which advances a given nuclide set, $\underline{N}_c^n$, forward in time.
This first-order method is acceptable providing the time-steps are small. However, second-order methods such as the mid-point method or predictor-corrector can be implemented in order to achieve greater accuracy.

Predictor-Corrector	**Mid-point**
$\underline{\Phi}_c^{k1} = \mathbf{M}\left(\underline{N}_c^n\right)$	$\underline{\Phi}_c^n = \mathbf{M}\left(\underline{N}_c^n\right)$
$\underline{N}_c^{k1} = \mathbf{B}\left(\underline{\Phi}_c^n, \underline{N}_c^n, \triangle t\right)$	$\underline{N}_c^{n+1/2} = \mathbf{B}\left(\underline{\Phi}_c^n, \underline{N}_c^n, 1/2\triangle t\right)$
$\underline{\Phi}_c^{k2} = \mathbf{M}\left(\underline{N}_c^{k1}\right)$	$\underline{\Phi}_c^{n+1/2} = \mathbf{M}\left(\underline{N}_c^{n+1/2}\right)$
$\underline{N}_c^{n+1} = \mathbf{B}\left(\frac{1}{2}(\underline{\Phi}_c^{k1} + \underline{\Phi}_c^{k2}), \underline{N}_c^n, \triangle t\right)$	$\underline{N}_c^{n+1} = \mathbf{B}\left(\underline{\Phi}_c^{n+1/2}, \underline{N}_c^n, \triangle t\right)$

The first set of reaction rates calculated by the mid-point rule will be under-estimated while the second set will be over-estimated. Thus, the average of the two sets of reaction rates is considered to be a good approximation. An alternative to the averaging of reaction rates, is the predictor-corrector algorithm which calculates reaction rates half-way through the time-step and completes a burn-up step for a whole time-step based on the half-step reaction rate.
Third- and fourth-order methods can be implemented, however higher-order methods are not commonplace for two reasons:

- The increased computational cost of completing more than two Monte Carlo runs per time-step is not guaranteed to increase the accuracy of the solution to an extent that is statistically significant. This is due to the limitation of the Monte Carlo calculation which

computes its solution with an order of accuracy of 1/2. Therefore, the order of accuracy of the whole scheme will never exceed O(1/2).

- The second, most problematic effect of higher order methods is the increased computational cost of performing several Monte Carlo runs per time-step. The Monte-Carlo runs are often computationally expensive and account for more than 95% of the computational power of the depletion analysis. Depletion analysis based on second order methods can take several weeks to run on modern computer clusters, hence a further increase in computational cost is, in many scenarios, prohibitively expensive. Currently, both FATI and the benchmarking code, VESTA, implement the forward Euler method. The option to select the order of accuracy/numerical method is planned for both codes.

The generation of cross-sections within Monte-Carlo (MC) depletion codes can be accomplished via two methods [104]: the "standard" pointwise estimator approach of tallying the reaction rates in the MC code and the "multigroup" approach which uses the average neutron spectrum tallied by the MC code, in a predefined group structure, to calculate reaction rates. The point-wise calculation of all reaction rates within every cell of a MC method is very time consuming. Calculation of a single neutron spectrum for a cell is relatively fast when compared to the tallying of reaction rates via point-wise estimators, hence the multigroup method is significantly faster than the standard method. However, the multigroup method is not completely consistent with the standard method; as a result, some codes such as MCNPX [98] and MCOR [105] use a combination of both standard and multigroup approaches. The standard approach is implemented for "important" reactions and the multigroup approach is implemented for the remainder of reactions. For principal reactions, such as (n,g), (n,2n), (n,3n), (n,p), (n,α) and fission [106], MCNPX calculates reaction rates, via the point-wise method, and passes the rates to the CINDER burn-up code. For other reactions, a 63 group neutron spectrum for each cell is passed to CINDER where the cross-sections are calculated externally to MCNPX. MCOR operates in a similar manner, where the reactions of 88 of the most important isotopes are calculated directly in MCNP and the remainder are calculated externally by ORIGEN.

4.2 FATI

An important question which needs to be answered is "why write a new activation-radiation transport coupling program when others already exist?". In order to answer this question, the scrutinisation of current depletion methods must be performed

MCNP burn-up limitations:

- The burn-up feature allows a particular material to be burned. Materials specified in a material card will very often be linked to many cells and in many different regions. Hence, the nuclide inventory of a particular cell cannot be known exactly unless the MCNP input file is modified such that the same material is duplicated in the materials card and each cell points to a different material number. The duplication of materials definitions is unnecessary and can potentially introduce human error.
- Neutron energies span several orders of magnitude yet the MCNP code models the radiation transport with only 69 energy groups. The energy binning resolution can be several orders higher in activation codes such as VESTA. Hence, the use of activation codes with higher energy resolution would result in lower uncertainties in the output data.
- The MCNP algorithm only captures daughter nuclides of the nuclides specified within the materials card and not the whole chain. This is a serious limitation as many secondary and loop reactions take place which could not be modeled with the MCNP burn-up functionality.
- MCNP utilizes the CINDER activation code which models the burn-up using a Markovian chain model. Although, this model is relatively simple and quick to solve it has the serious limitation that it cannot model reaction loops.
- Only fission neutron sources (KCODE) can be used with the BURN keyword; user defined sources such as those needed in fusion neutronics cannot be used in conjunction with BURN.

The MOCUP & Monteburns codes are generally very comprehensive in terms of their functionality, however the additional text based input parameters needed for the operation of the programs add unnecessary complication which could introduce human error. In addition to this, the current depletion codes were designed for fission analysis which require different operational parameters to be monitored. For instance, the effective multiplication constant (k_{eff}) and ^{235}U burn-up is of interest for fission but not for fusion, whereas tritium breeding ratios and inventories are important for fusion, but not fission.
The objective is to write a radiation transport-activation coupling code, called FATI, which does not suffer from the limitations/weaknesses mentioned above.

4.2.1 FATI Functionality & Input Files

The program has been designed to allow most MCNP input files as an input and require as little additional information to the MCNP input file as possible. Other programs of similar functionality require comments in the MCNP input file (MOCUP) or lengthy input files (MONTEBURNS). FATI does not require comments in the MCNP file and allows the user to specify the simulation parameters via easy to use, windows based forms. However, a text based input file can also be used is the user prefers.

FATI (Fusion Activation and Transport Interface) is a depletion code, written in C++, that interfaces MCNP5/X with FISPACT. The intended primary application of FATI is the simulation of nuclide burn-up within fusion blankets, hence specific features such as the calculation of tritium inventories and tritium breeding rates are built into the code. The code requires a MCNP input file, which requires no modifications, and three short input files. The FATI preprocessor restructures the MCNP input file such that the output can be easily read and processed by the main FATI passing routine. The core feature of FATI is the cyclic automatic execution of a MCNP input file, processing of the MCNP output, writing and execution of several FISPACT input routines, calculating important reactor properties (nuclide inventory, tritium breeding rates etc) and feeding transmutated nuclides back into MCNP. This automated cyclic routine can determine the tritium breeding rates, tritium inventory, nuclide inventory as a function of time over the lifetime of the reactor. Another feature of FATI is the automated nuclide and tritium controllers which allow the removal and addition of specific nuclides in order to maintain a specified tritium breeding rate/inventory. The FATI code utilizes the MATLAB engine to automatically produce charts which can be modified and/or saved in several formats via the well-known MATLAB interface.

The multi-group binning method is FATI's default method of synchronisation of MCNP and FISPACT reaction rates, which involves the passing of a 351 group (Tripoli ++) neutron spectrum from MCNP to FISPACT per burn cell. The FISPACT code then collapses each neutron spectrum with EAF cross-sections to produce many effective cross-sections which can then be substituted directly into the burn-up equations. The multi-group binning method is well known to be the fastest method of calculating reaction rates, however this method can suffer with significant inaccuracy when the multi-group energy structure has an insufficiently fine structure to match that of the cross-section it is being collapsed with. Therefore, FATI can force reaction rates of particular importance (user specified) to be calculated by the standard reaction rate

method, whereby MCNP calculates several rates directly.

The control features of FATI were developed specifically for fusion systems. A list of parameters and functions can be found in Appendix A, however the main functions are:

- **Extract:** The extract feature allows specified nuclides, N_i, to be removed from the burn cells if their number density is above a pre-defined threshold, T_i. Nuclides with number densities above this threshold will then be reduced according to:

$$N_i^{new} = \left\{ \begin{array}{cc} N_i^{old} & N_i^{old} \leq T_i \\ R_i \left(N_i^{old} - T_i \right) & N_i^{old} > T_i \end{array} \right\}$$

Where R_i is a constant which specifies the proportion of the excess which is to be removed.

- **Fill -** A complimentary feature to Extract is the Fill feature. In order to conserve mass, a specified material's composition can be specified which replaces the extracted material.
- **Tank -** A FATI feature which is particularly useful for fusion depletion is the tank, a virtual cell which stores materials which are to be added/removed from the blanket. The initial tank contents can be specified in the FATI input file; the contents of which will be changed based on the removal/filling procedure specified.
- **Tritium controller:** The tritium controller adjusts the lithium content within the blanket in order to stabilize tritium tank inventory at a specified level. This controller is described in detail in Chapter 5.
- **CP model** - In order to reduce the computation cost of exact pulse modelling, the continuous pulse model can be used within FATI. The continuous pulse duration and number of final short pulses can be specified in the input file

Some of the system features of FATI are:

- **Spectrum output** - The neutron spectrum of every burn cell within the model can be viewed either as a function of time or cell.
- **Nuclides output** - The tracking of the nuclide inventory for each cell within the model can be approached in two ways: Store all data and use data mining to retrieve required data, or specify at the outset which nuclides are of interest. The second option has been adopted for FATI in order to reduce the amount of data to be stored.

- **Rate transfer** - Both methods of reaction rate transfer are available in FATI. The default method of rate calculation is multigroup, however any reaction rate can be calculated via a point-wise estimator approach if the user prefers.
- **TBR:** The tritium breeding ratio is calculated automatically for every time-step using two methods of calculation. Firstly, a pointwise estimator approach in MCNP and secondly via a multigroup method implemented in FISPACT.

A windows based front end for FATI has been created which allows the user to view FATI, FISPACT and MCNP input/output files, and also create the FATI parameters. Thus, the operation of the program is relatively simple due to the use of common controls and form layout. Another convenient feature of FATI is the ability to automatically produce MATLAB generated charts of tritium breeding rates, nuclide inventories and neutron spectra, via a simple Windows form and the utilization of the MATLAB libraries. For verification purposes, all MCNP and FISPACT input and output files are stored in a directory allocated to each FATI run. The FATI program also serves as a MCNP and FISPACT input file editor where the file can be run and the output viewed via the windows menu. The operation of FATI is specified by the files "PARAM_INPUT" and "FILES" - both of these files can be altered manually or via the FATI v2 program which allows the user to browse and select the file required.

4.2.2 FATI Procedures

The FATI program operation, defined schematically in figure 4.1, has been considerably simplified by introducing two pre-processing features to the MCNP input file:

1. Immediately introduce a one-to-one relation between the materials and the cells - In a typical MCNP simulation many cells within a MCNP file will have the same materials composition, hence many cells will point to a single material. This is also the case for a FATI simulation for t = 0; however, after the first FISPACT burn-up all of the cells will have an unique materials composition. Hence the many-to-one relation between material and cell becomes one-to-one after the first time-step. In order to reduce the variability and complexity of the MCNP input file throughout the FATI run time, the MCNP input file cell-material relations are transformed to one-to-one from the outset. This results in invariable surface and cell cards throughout the FATI run. The cell-material-nuclides data relations are are formally illustrated in figure 4.2.
2. Split the MCNP input file into three components - As mentioned in section 2.5.1, the

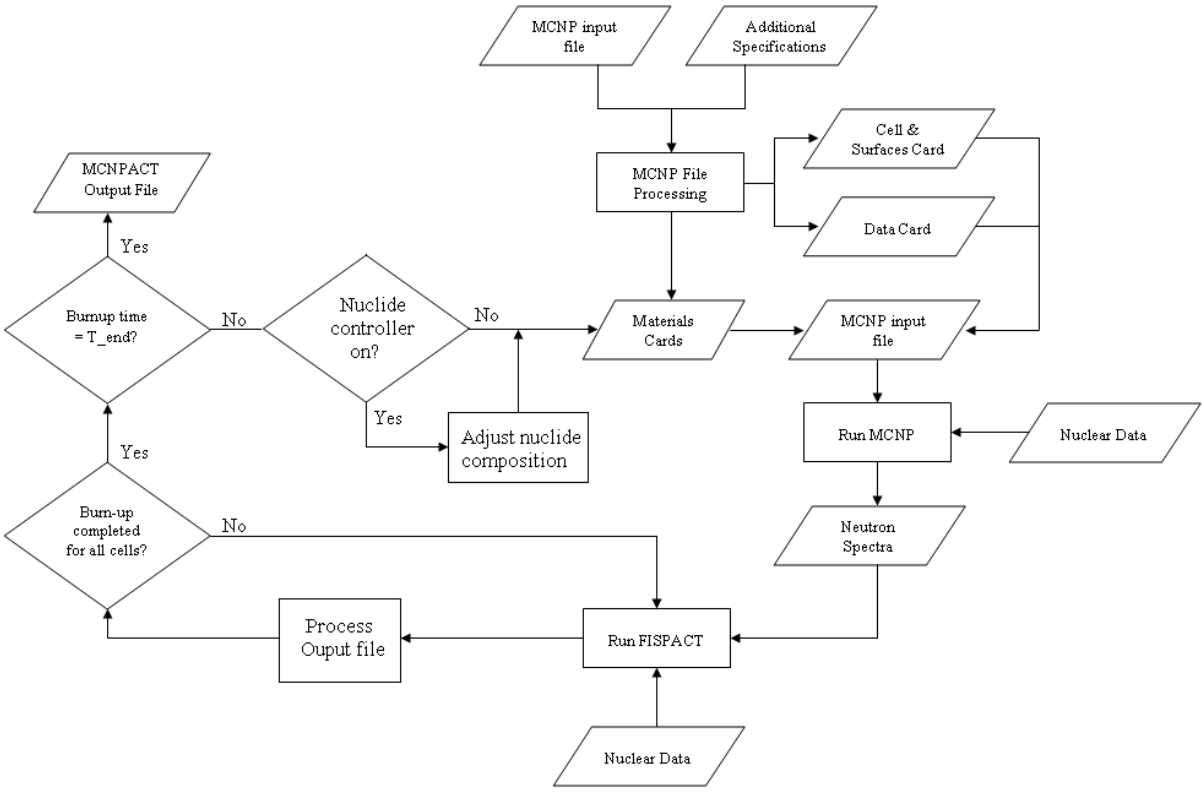

Figure 4.1: FATI Flowchart. Firstly, the FATI code reads a user defined specification file (Additional specifications), which is then used to extract appropriate data from the MCNP input file. This data is then used to recreate a materials card which is written in a form which can be easily adjusted in future procedures. The new materials card is then recombined (MCNP input file) with other parts of the MCNP input file and is executed (Run MCNP). For each cell within the MCNP input file that has been selected to be burnable, a neutron spectrum (Neutron spectra) is passed to the FISPACT burn-up code (Run FISPACT) along with the materials composition for that cell. The nuclides names and number density format (Alphanumeric isotope and number of atoms/cc) are then converted to MCNP format (ZAID and fraction by number). If the nuclide controller is switched on then the material composition for each cell will be adjusted according to the Additional specifications file. The materials for each cell are then used to recreate a new MCNP input file and the cycle is repeated until a predefined number of iterations have been completed.

MCNP file is essentially divided into surface cards, cell cards and data cards. After the cell-material relations have been changed by process 1, the cell and surface cards are written to file as a single block and the data card is split into two sub-cards containing the materials and physics blocks. The cell-surface and physics block remain unchanged throughout the running of the program (with the exception of when the density update is enabled). However, the materials block will change at every run. Each MCNP input file is unique and is assembled using the invariable cell-surface block, variable materials block and the invariable physics block.

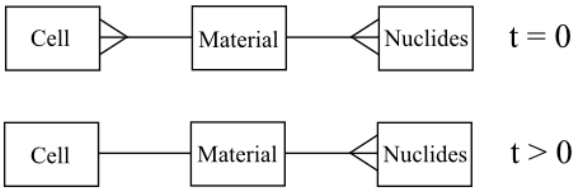

Figure 4.2: FATI data relations

4.2.3 FATI Limitations

At present, the FATI program has some limitations, some of which will hopefully be removed in later versions. The limitations include:

- **Limited Nuclide Data** - Some nuclides produced as a result of burn-up in FISPACT are not present in the MCNP xsdir file. MCNP crashes when it cannot recognize a ZAID[1], hence this problem has been solved by removing the nuclide in question and throwing a warning message to screen and the FATI output file. These nuclides with missing data generally exist in very low numbers, hence they should not have a significant impact on the reliability of the simulation.
- **ICF Incompatible** - The current version of FISPACT(2005) has a minimum time resolution of one second, therefore it is not ICF compatible. The next version of FISPACT 2 will be ICF compatible and will replace v2005 as the activation code of choice when released.
- **Geometry Specification** - some geometry specification keywords are not supported by FATI. These keywords include those that appear in the second column of the cell card such as “like” and some universe keywords.

4.3 Optimisation of run time and accuracy

The sensitivity of material burn-up has been determined using three fusion reactor properties: spectral sensitivity, tritium self-sufficiency time and EUROFER transmutation. Each of these models rely on the reactor model shown in figure 4.3 and table 4.4. The isotopic compositions used in the model are: 40% Li-6 : 60% Li-7, natural composition for lead and the EUROFER composition is defined in reference [107]. The irradiation scheme is based on the equivalent steady steady (ESS) model, with a 1.5GW thermal power produced by a mono-energetic 14.06 MeV point isotropic neutron source. The simulation irradiation period is 5 years, which is

[1]Used to specify nuclide proton and nucleon numbers with many areas of nuclear data. i.e. 26056 specifies Fe-56

accounted by 60 individual monthly irradiation periods. The simplified blanket is composed of EUROFER steel, which contains a lithium-lead eutectic ($Li_{17}Pb_{83}$) tritium breeding material.

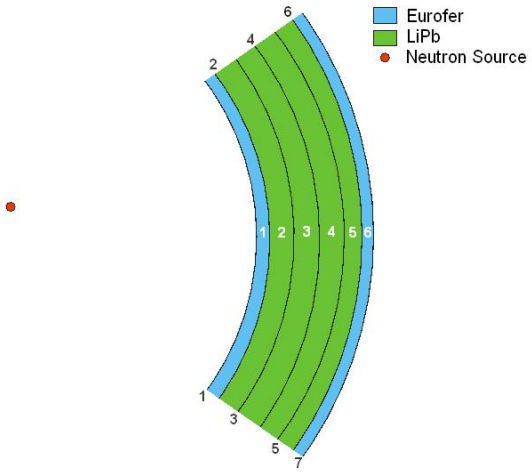

Figure 4.3: MCNP model of a simplified fusion reactor used for benchmarking / numerical testing purposes. The model consists of a sphere containing four layers of LiPb eutectic encased by EUROFER steel. The material and geometry specification are listed in tables 4.4 & 4.3.

4.3.1 Spectral sensitivity

The sensitivity of burn-up to spectral change was determined using two stages of modelling. Firstly, the burn-up of a simplified reactor model was computed using a single time-interval of two years. The neutron spectrum before, ϕ_{start}, and after two years of burn-up, ϕ_{end}, were recorded for each of the four cells. Secondly, these two neutron spectrum's were separately used as an input to the FISPACT code, whereby the burn-up of each of the 2192 isotopes within the EAF2005 database were individually modeled. The percentage differences in the material number density due to ϕ_{start} and ϕ_{end} were then computed, and are presented in section 4.

4.3.2 Tritium self-sufficiency time

Assuming a control system is not used to purify/alter the nuclide composition of the lithium breeding material (as would be the case for a solid breeder), the tritium self-sufficiency time (TSST) of a blanket can be defined as the time taken for the fusion reactor to cease producing enough tritium to sustain the reactor and for all excess tritium produced to be consumed. This is defined schematically in figure 4.4. The FATI code was used to calculate the sensitivity of TSST as a function of depletion step-size. This consisted of performing several individual depletion calculations implementing time-steps ranging from one day to 2 years. The FATI tritium controllers were switched off during these calculations, however the tritium was removed

from each cell after every burn-up calculation [2]. All of the tritium removed from the blanket was added to a tank, which was subject to a decay calculation at each time-step. Based on solution convergence as the time-step approaches zero, the 1 day time-step size is taken to be an accurate solution. TSST's produced utilizing larger time-steps are then compared to this accurate solution. A convergence ratio is used to define the accuracy of the TSST solution given a time step of $\triangle t$. The convergence ratio, R, is defined as:

$$R = \frac{TSST(\Delta t)}{TSST(\Delta t = 1\ day)}$$

The TSST has been extensively studied by Abdou [108] and others during the 1980's. However, fully-linked transport-burn-up calculations for fusion blanket studies have only recently been performed due to the increase of available computational power. The treatment of TSS within this study neglects some engineering aspects of tritium breeding such as fractional burn-up within the plasma, residence times of tritium within compartments, tritium leakage etc which were accounted for in Abdou's paper. However, the most important aspect of this study is effect of changing neutron spectra with time, which has not been accounted for in the mathematical and computational methods developed in the 1980's and early 1990's.

4.3.3 EUROFER Transmutation

EUROFER is a low activation steel designed for the fusion devices. Common steels have traces of many elements mixed within the iron matrix in order to improve materials parameters, such as ductility and fracture toughness, and corrosion resistance. However, many of these trace elements absorb neutrons; resulting in daughter nuclides that are radioactive. The EUROFER steel is composed of alternative and a reduced number of trace elements, in order to reduce dose rate and nuclear activity during and after fusion plant operation.

The method implemented for spectral sensitivity was applied to the transmutation of nuclides within EUROFER steel. However, both parent and daughter nuclides are measured in this study.

4.4 Results

The neutron spectrum for cell 3 is shown in figure 4.5. Over a period of two years the magnitude of the neutron flux increased by approximately 4%, with the thermal region of the spectrum showing the most prominent increase.

[2] Given that every step of the burn-up is approximately one day, this assumption links up well with the fission practice of adding boron to coolant on a daily basis in order to control K_{eff} via neutron poisons.

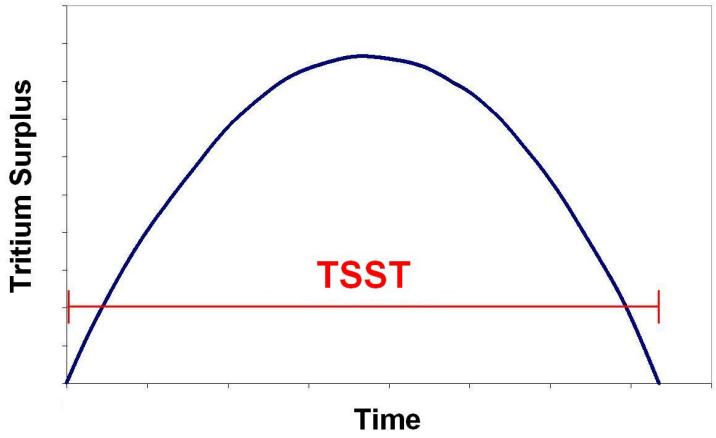

Figure 4.4: Tritium blanket lifetime: The time taken for the tritium surplus produced by a blanket to rise to a maximum value and fall to zero; After (or preferably shortly before) this period the blanket must be replaced. At the start of the reactors lifetime the TBR is greater than unity, which leads to a fast increase in the tritium surplus in the fist few years. As the lithium depletes, the amount of tritium being produced decreases and the TBR approaches unity (this corresponds to the apex of the curve). Once the TBR goes below unity the tritium surplus reserve must be used in order to sustain the reactor and the surplus reduces until the blanket is replaced.

4.4.1 Spectral sensitivity

The difference in material burn-up for fusion relevant isotopes within EAF2005 is shown in table 4.1. Other than ^{3}He, $^{180/181}Ta$ and ^{10}B, the difference in parent nuclide burn-up rates are statistically insignificant when compared to variations and uncertainties within cross-sections and the uncertainty associated with numerical and statistical methods. However, these result only show the effect of the parent nuclide, a significant difference in the rate of burn-up is evident with the daughter nuclides. A fusion specific example is shown in table 4.2, whereby the difference in burn-up of parent and daughter nuclides of EUROFER steel is shown.

4.4.2 EUROFER transmutation

As with the previous results, parent nuclide transmutations show little sensitivity to neutron spectrum changes in term of percentage change. However, this is not the case for daughter nuclides. The daughter products found in the $W(n,\gamma)(\beta^{-})Re(n,\gamma)(\beta^{-})Os(n,\gamma)(\beta^{-})Ir(n,\gamma)(\beta^{-})Pt$ reaction chain show the most significant dependence on the neutron spectrum distribution, where the difference are in the order of hundreds of percent. Daughter products found in the $Mo(n,\gamma)(\beta^{-})Tc(n,\gamma)(\beta^{-})Ru(n,\gamma)(\beta^{-})Rh(n,\gamma)(\beta^{-})Pd$ reaction chain also show significant changes in rate of burn-up when irradiated by new and aged neutron spectra. The production of gases within the steel were virtually unaffected by changes in the neutron spectrum. Other

nuclides found in the initial composition and post-irradiation of EUROFER show little change given the change in neutron spectrum shape and magnitude over the two year period.
In order to ensure important daughter nuclides are accurately modeled within depletion codes a time-step interval between radiation transport calculations should be less than one month.

Isotope	N_{Diff} (%)	Isotope	N_{Diff} (%)
^{6}Li	-2.221	^{28}Si	-0.0012
^{7}Li	-0.0007	^{29}Si	-0.0071
^{9}Be	0.0009	^{30}Si	-0.1181
^{186}W	-0.5894	^{54}Fe	-0.0622
^{184}W	-0.7393	^{56}Fe	-0.0190
^{183}W	-2.0299	^{57}Fe	-0.1062
^{182}W	-0.9286	^{50}Cr	-0.1377
^{16}O	-0.0002	^{52}Cr	-0.0189
^{53}Cr	-0.1713	^{63}Cu	-0.2708
^{54}Cr	-0.0081	^{65}Cu	-0.1079
^{185}Re	-3.608	^{46}Ti	-0.0188
^{187}Re	-3.550	^{47}Ti	-0.1549
^{58}Ni	-0.0453	^{48}Ti	-0.0655
^{60}Ni	-0.0371	^{49}Ti	-0.0296
^{61}Ni	-0.1488	^{50}Ti	-0.0017
^{12}C	-0.0002	^{51}V	-0.1023
^{180}Ta	-7.3552	^{3}He	-10.149
^{181}Ta	-3.5199	^{209}Bi	-0.0170
^{180m}Ta	-8.4108	^{210}Bi	0.00557
^{10}B	-8.9660	^{55}Mn	-0.2417

Table 4.1: Percentage differences, for cell 5, between the initial and partially burned neutron spectrum's for some fusion relevant isotopes. $N_{Diff} = 100 * (N_D^{\phi_{start}} - N_D^{\phi_{end}})/\phi_{start}$

4.4.3 Tritium self-sufficiency time

The effect of variable neutron spectra on tritium breeding is significant. The effect of subtle changes in tritium breeding ratio are shown to be significant in figure 4.6. This figure shows the tritium surplus over time for a number of time intervals. At the end of every interval the neutron spectrum is updated (seen as discontinuities in figure 4.6). As the time interval is reduced, the TSST converges on a time of 7.4 years. For this spherical model, a single pass burn-up calculation drastically underestimates the tritium self-sufficiency time of the blanket while time-step intervals over 2 weeks in duration cause errors which are greater than errors associated with cross-sections and other sources of uncertainty/error implemented within the computational method of burn-up. Figure 4.8 shows the tritium self-sufficiency times as a function of time-step and an extrapolated lifetime for infinitely small time interval. This extrapolated lifetime suggests that a single day interval produces a TSST which is accurate to within 1%. A tritium self-sufficiency time convergence test is shown in figure 4.7, which warrants the validity of the

C:/TimeStepping/FLUX_COMP.eps

Figure 4.5: Neutron spectra within cell 3 (of model shown in figure 4.3) at t = 0 and t = 2 years.

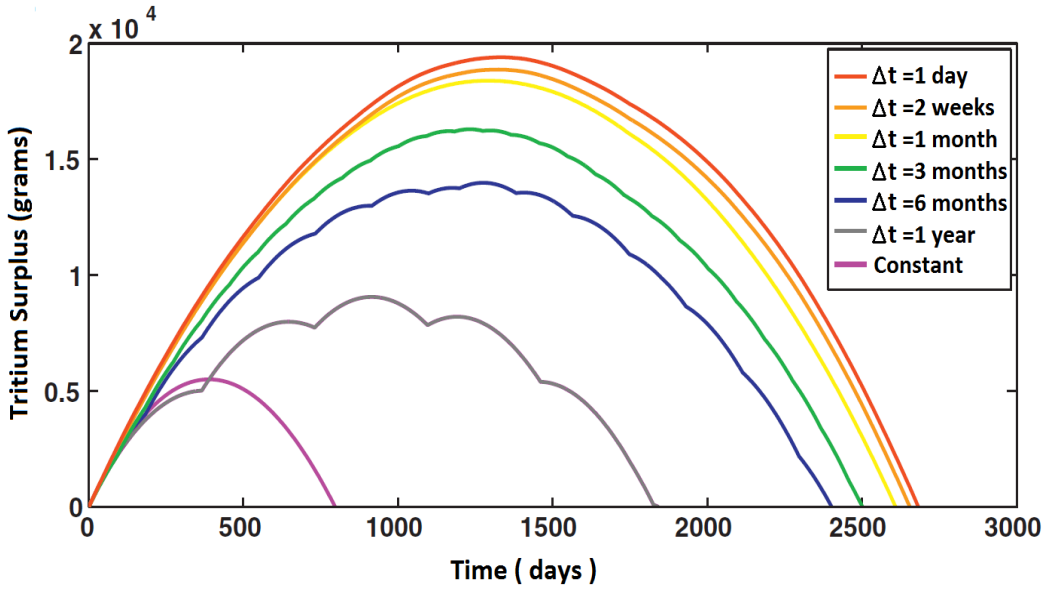

Figure 4.6: A comparison of tritium inventories for several time-step intervals ranging from one day to 2 years.

Element	N_{init}	N_{diff} (%)	Element	N_{init}	N_{diff} (%)	Element	N_{init}	N_{diff} (%)
H	-	0.0809	Si	2.682E21	0.000	Cu	2.362E20	0.2345
He	-	-0.4046	P	2.355E20	-0.0453	Nb	4.709E19	0.0369
Li	-	-14.674	S	2.400E20	-0.0052	Mo	2.350E20	0.1122
Be	-	-0.1678	Ti	4.691E20	0.0065	Fe	4.180E24	0.000
B	4.658E19	1.2434	V	9.395E21	-0.1071	Ta	3.287E21	2.7032
N	1.409E21	-0.0235	Cr	4.227E23	0.000	W	5.167E22	0.2596
O	4.690E21	0.000	Mn	1.879E22	0.1295	Re	-	-19.592
Sc	-	0.1332	Rh	-	-74.39	Pd	-	-203.96
Al	4.696E20	0.0090	Co	2.340E20	-2.175	Lu	-	3.7
Ru	-	-26.98	Y	-	0.3205	Os	-	-50.57
Tc	-	-17.29	Mg	-	-0.073	Pt	-	-503.88
Mo	-	0.1122	Hf	-	1.8145	Ir	-	-196.24

Table 4.2: Percentage differences, for cell 3, between the initial and partially burned neutron spectrum's for isotopes found in EUROFER steel. $N_{Diff} = 100 * (N_D^{\phi_{start}} - N_D^{\phi_{end}})/\phi_{start}$

extrapolation. The calculated TSST convergence is shown in figure 4.7. It clearly shows that time-step sizes of less than 100 days result in a solutions which are greater than 90% accurate. This significant difference in TSST's for single and multiple time-steps has also been shown by Aures [109], where the tritium breeding capability of a HCPB DEMO model was analysed. This study included a comparison of the TSST for a single time-step calculation and a one year time-step calculation. The single time-step model calculated a TSST that is approximately 75% less than the 1 year TSST calculation. However, figure 4.6 suggests that the calculated TSST could be increased if Aures reduced the time-step from 1 year to less than 1 month.

Although the increase of the TSSL, as a result of decreasing the time-step, is purely due numerical convergence the result can be interpreted in term of the neutronics. Each neutron-transport run, which has an updated materials set, will calculate a new neutron spectra with a more prominent thermal region. This is due to the burn-up of lithium, within the blanket, which will result in fewer neutrons being absorbed over time. Thus, the number of neutrons will increase with time, especially in the lower part of the neutron spectrum where the neutrons were more likely to be absorbed at the start of the calculation.

4.5 FATI Benchmarking

The FATI code, which interfaces MCNP and FISPACT, was benchmarked against the VESTA depletion code - A Monte Carlo depletion interface code, developed at IRSN, which has the potential to link any MC transport code and burn-up code. The current version supports MCNPX & MORET5 as the transport codes and ORIGEN 2.2 & PHOENIX as the burn-up codes, with support for other Monte-Carlo codes and burn-up codes in development. VESTA and FATI

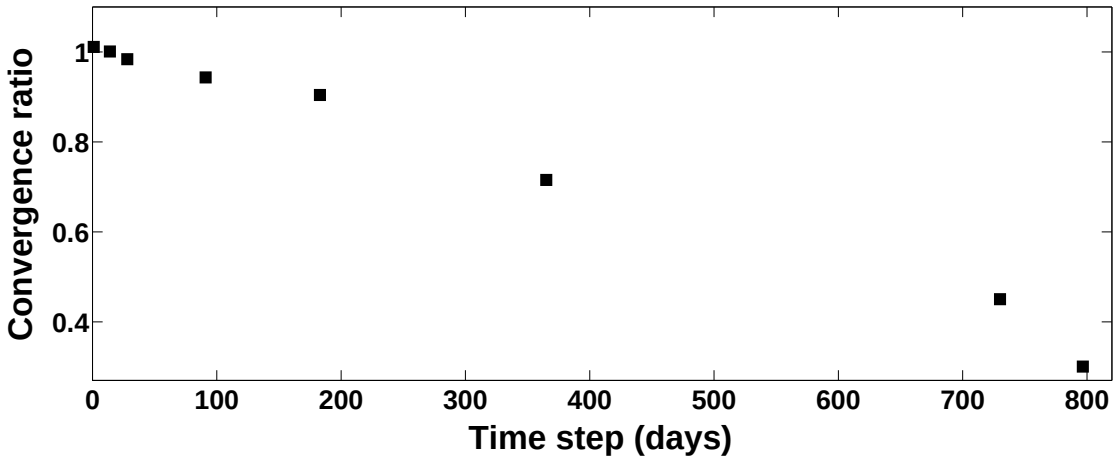

Figure 4.7: TSST's convergence for several time-step intervals ranging from one day to 2 years.

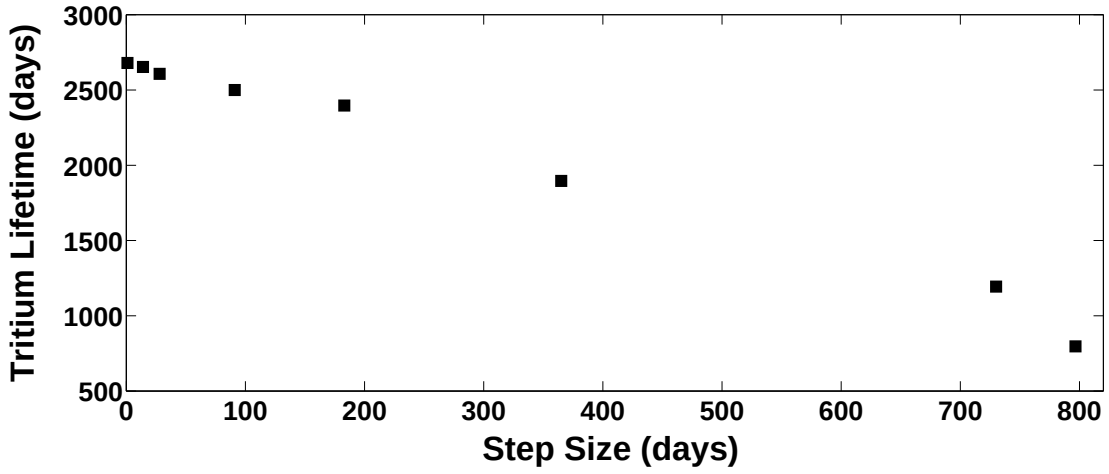

Figure 4.8: TSST's convergence for several time-step intervals ranging from one day to 2 years.

operate in a broadly similar manner, however they differ with respect to:

- Solution of burn-up equations - FATI utilizes FISPACT as the burn-up code, which solves the Bateman equations numerically. VESTA utilizes the PHOENIX code which solves the equations using the matrix exponential method.
- Energy group structure - VESTA allows for any user defined energy group structure to be implemented for multi-group reaction rate calculations and has a default group structure of 43,000. FATI allows for only the group structures defined in the EASY-2007 package (69, 100, 172, 175, 211, 315, 351 groups)
- Input file - The VESTA input file consists of a single file which includes both the MCNP input and the VESTA instructions. FATI separates its input files from the MCNP input.
- Output - The VESTA code outputs in human readable format (xml), whereas FATI links to the MATLAB engine which allows graphs to be produced from a menu and then saved in MATLAB format.
- Nuclide output - The VESTA code writes all nuclide number densities to file and implements data mining in order to retrieve the required number densities. FATI requires the user to specify which nuclides are of interest in the input file, thus reducing output file size.
- FATI - In order to simulate the removal and addition of nuclides within liquid blankets, the FATI code incorporates a "tank" which stores surplus nuclides before and after removal from the blanket. VESTA does not have this feature.
- Tritium control - The production of tritium in a controlled and predictable manner requires the application of control theory. FATI implements simple control theory which adds and removes lithium and other materials in order to maintain a predefined tritium surplus. VESTA does not implement control theory however it allows for many other system configuration changes such as geometry, material position, temperature and density.
- Tritium monitoring - FATI tracks the TBR and tritium cumulative surplus inventory with time.
- Cross-sections - The VESTA code allows the temperature to be specified and cross-section files to be chosen. FATI accesses a single temperature cross-section file and has no cross-section options.
- Irradiation profile - VESTA allows for any user defined irradiation profile, whether pulsed and/or continuous. FATI allows for a continuous or pulsed irradiation followed by an

optional single pulsed irradiation, allowing for the implementation of the continuous pulse model.

- Flux normalisation - VESTA incorporates many flux normalisation options, such as single source, single power or powers for each material. However, FATI implements a single normalisation, constant flux source, which is sufficient for pure fusion applications.

4.5.1 Test model

The nuclide production, nuclide inventory, TBR and neutron spectra of a simple spherical IFE fusion reactor were examined using the depletion codes FATI and VESTA. The reactor model, as specified in figure 4.3 and tables 4.3 & 4.4, was designed purely for benchmarking purposes and has no practical or engineering significance. The irradiation scheme is based on the equivalent steady steady (ESS) model, with a 1.5GW thermal power produced by a mono-energetic 14.1MeV point neutron source. The simulation period is 5 years, which is accounted by 60 individual monthly irradiation periods. The simplified blanket is composed of EUROFER steel, which contains a lithium lead eutectic ($Li_{17}Pb_{83}$) tritium breeding material.

EUROFER element	%
B	0.00100
C	0.11000
N	0.03000
O	0.01000
Al	0.01000
Si	0.05000
P	0.00500
Cr	9.00000

EUROFER element	%
Mn	0.40000
Fe	88.96300
Co	0.00500
Ni	0.00500
Cu	0.00500
As	0.00500
Nb	0.00100

EUROFER element	%
Ti	0.01000
V	0.20000
Sn	0.00500
Ta	0.07500
S	0.00500
Mo	0.00500
W	1.10000

Table 4.3: EUROFER initial composition. EUROFER is a steel with low impurity content which is designed to have low activation.

Cell	Material	Composition	Radial width (cm)
1	void	-	578
2	EUROFER	ref [107]	2
3	LiPb	Natural Pb 40%^{6}Li, 60% ^{7}Li	12
4	LiPb	Natural Pb 40% 40%^{6}Li, 60% ^{7}Li	12
5	LiPb	Natural Pb 40% 40%^{6}Li, 60% ^{7}Li	12
6	LiPb	Natural Pb 40% 40%^{6}Li, 60% ^{7}Li	12
7	EUROFER	ref [107]	2
8	void	-	-

Table 4.4: MCNP cell material.

4.5.2 Results

The nuclide production, nuclide inventory, TBR and neutron spectra of a simple spherical inertial fusion energy reactor were examined using the depletion codes FATI and VESTA. Table 4.5 shows the number density percentage differences for MCNP cell 3 and 6. Figures 4.10 and 4.14 show the percentage differences of number densities between the two codes. For cell 3, the ^{7}Li burn-up difference is effectively zero, while the FATI's ^{6}Li burn-up is monotonically underestimated up to approximately 1.6%. For cell 6, the lithium isotopic errors increase almost linearly up to approximately 0.6%. Given the exponential nature of the solution and the difference in cross-section values within different databases is around 5%, the difference in the number densities is relatively small.

Figures 4.12 and 4.13 show the percentage differences over a period of five years. The major differences in number densities of H and He isotopes is due to alternative methods of gas treatment within FISPACT and PHOENIX. The FISPACT gas production is generally higher due to the FISPACT including the daughter isotope and the by-product in the inventory calculation. For instance, the $^{6}Li(n,t)^{4}He$ reaction is treated as a producer of both tritium and helium by FISPACT, however PHOENIX does not include the tritium by-product in the inventory. Also, production of gases is highly dependent on reaction within the thermal energy regions when compared with other reactions. Thus, the treatment of thermal cross-sections within VESTA

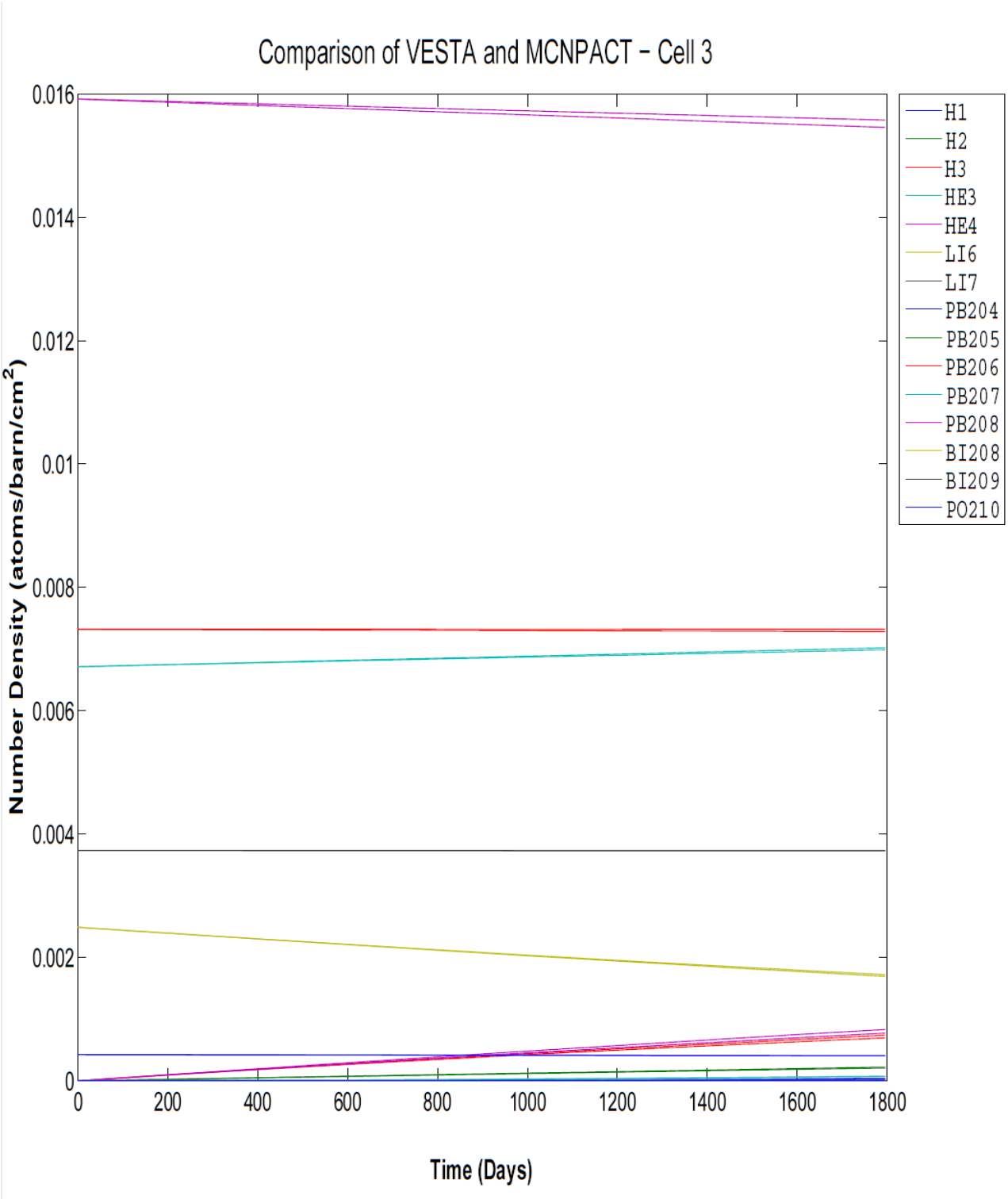

Figure 4.9: A comparison of VESTA-FATI number densities for MCNP cell 3. FATI and VESTA calculated number densities of specific isotopes are shown in the same colour. Thus, due to the similarity of the results, some lines are indistinguishable. Depletion calculation performed for 5 years.

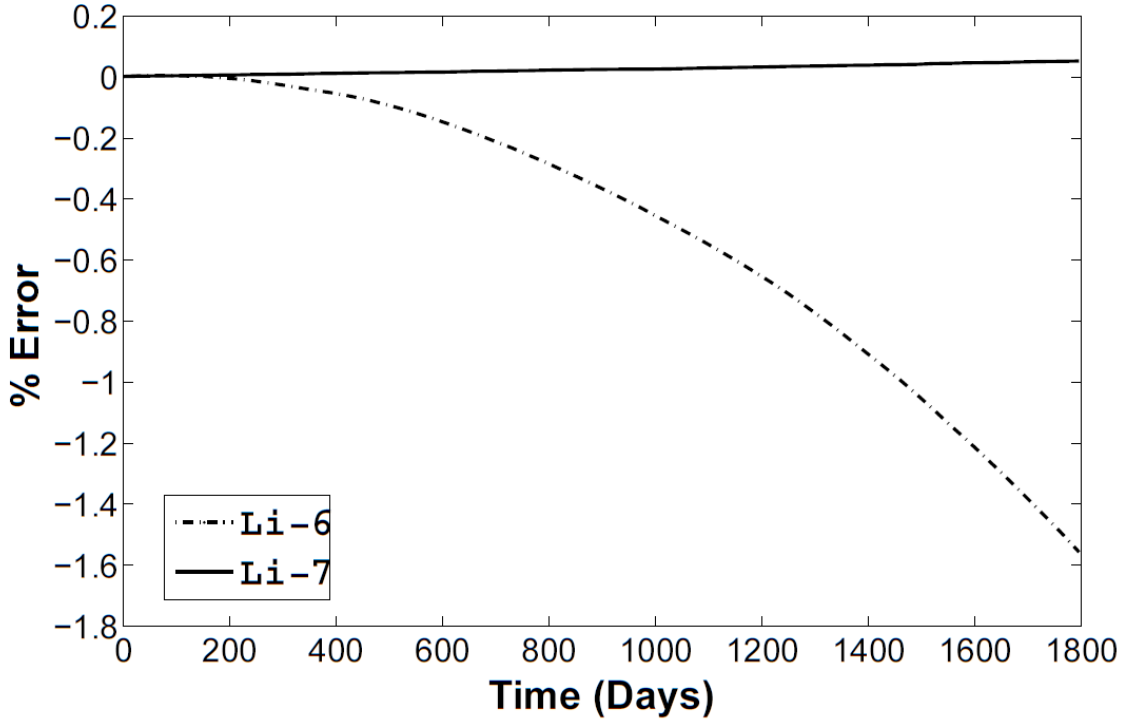

Figure 4.10: VESTA-FATI percentage variation of lithium number densities for MCNP cell 3. Depletion calculation performed for 5 years.

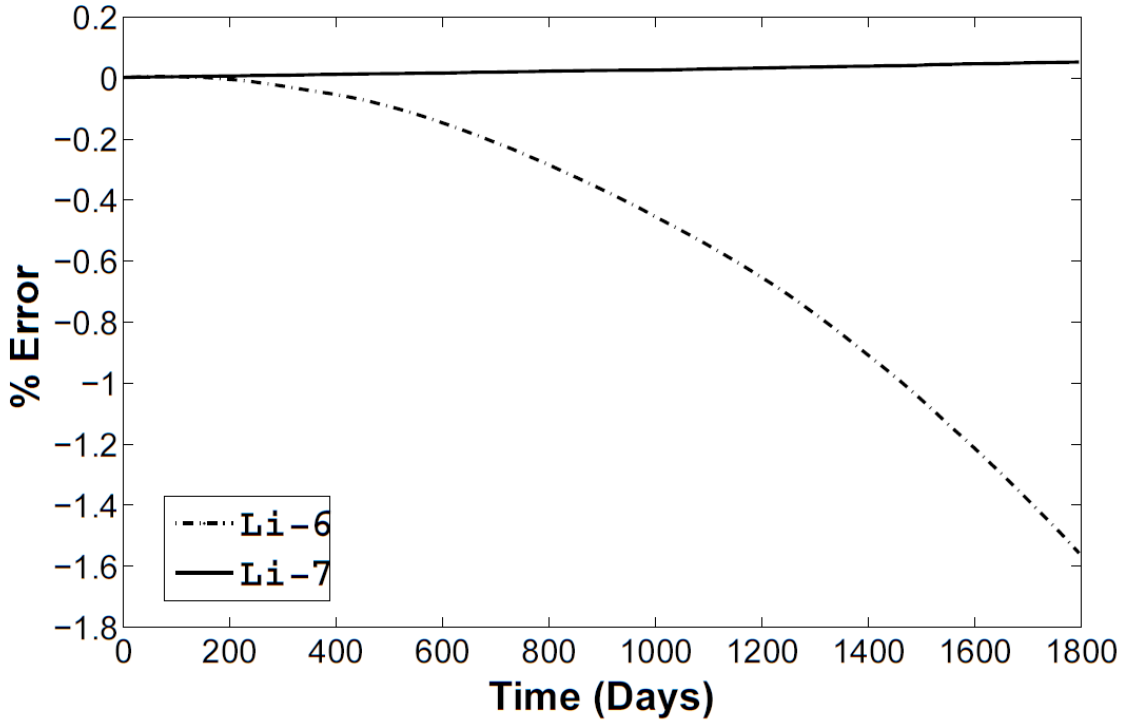

Figure 4.11: VESTA-FATI percentage variation of lithium number densities for MCNP cell 6. Depletion calculation performed for 5 years.

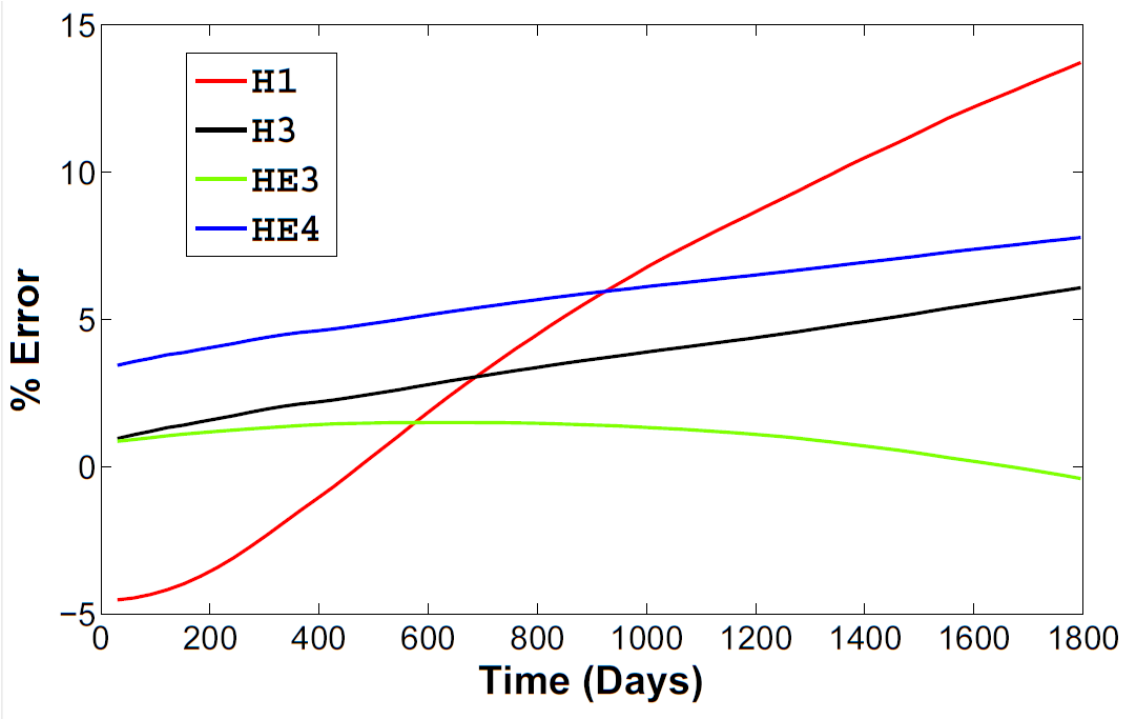

Figure 4.12: VESTA-FATI percentage variation of gas number densities for MCNP cell 3. Depletion calculation performed for 5 years.

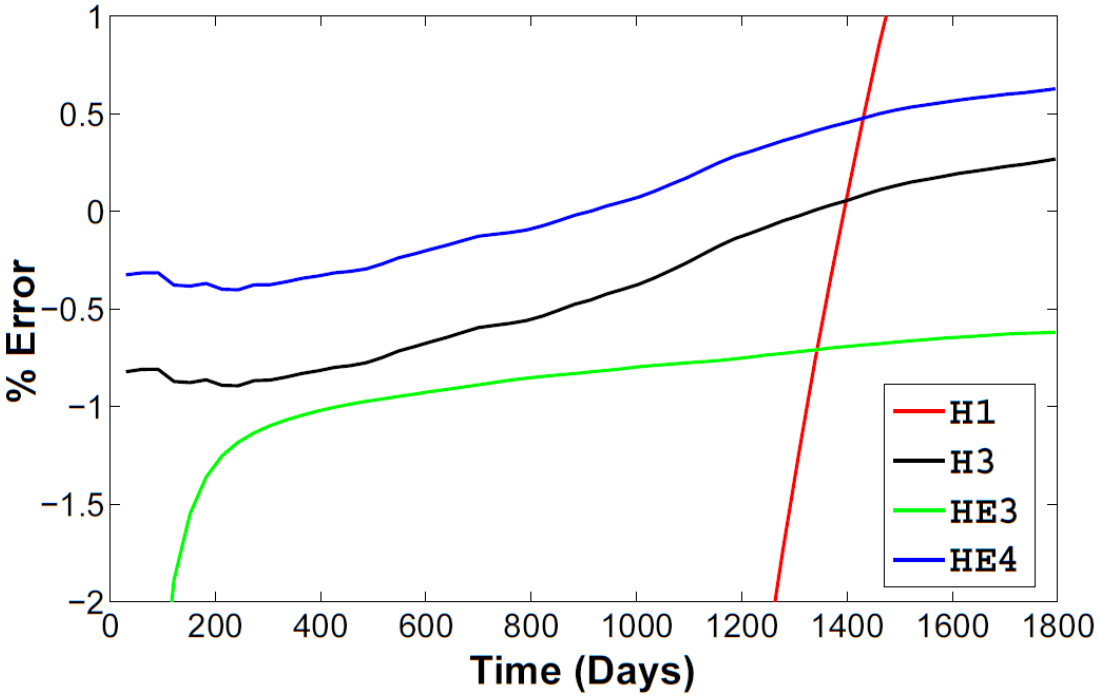

Figure 4.13: VESTA-FATI percentage variation of gas number densities for MCNP cell 6. Depletion calculation performed for 5 years.

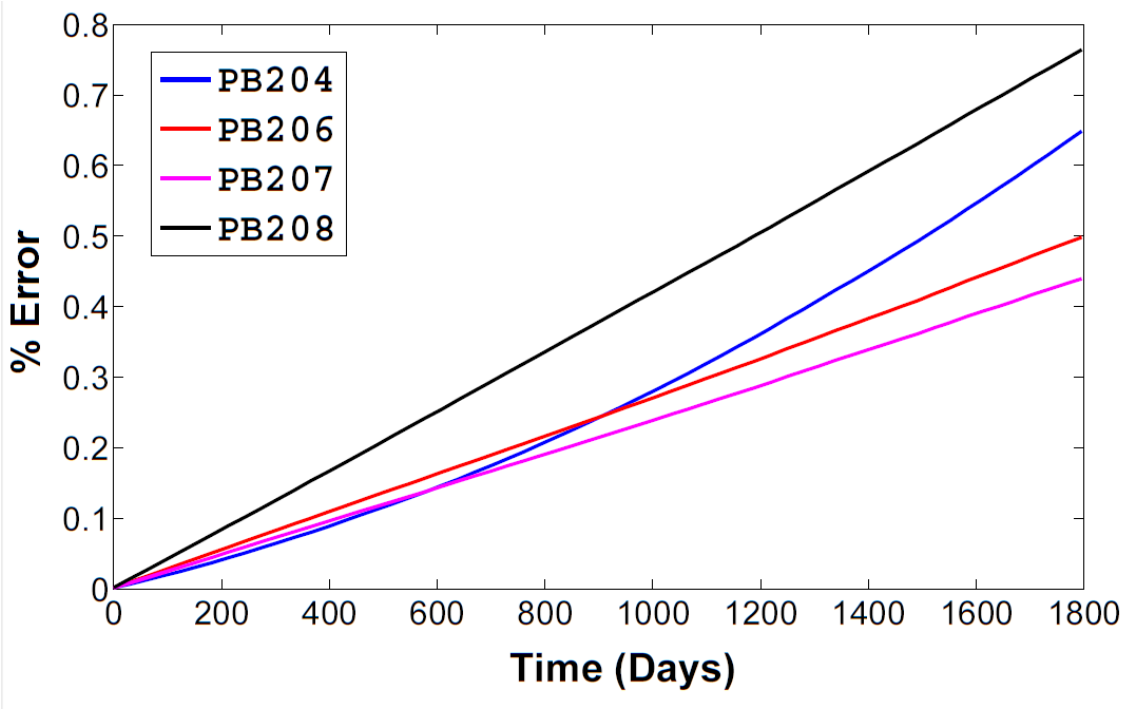

Figure 4.14: VESTA-FATI percentage variation of lead number densities for MCNP cell 3. Depletion calculation performed for 5 years.

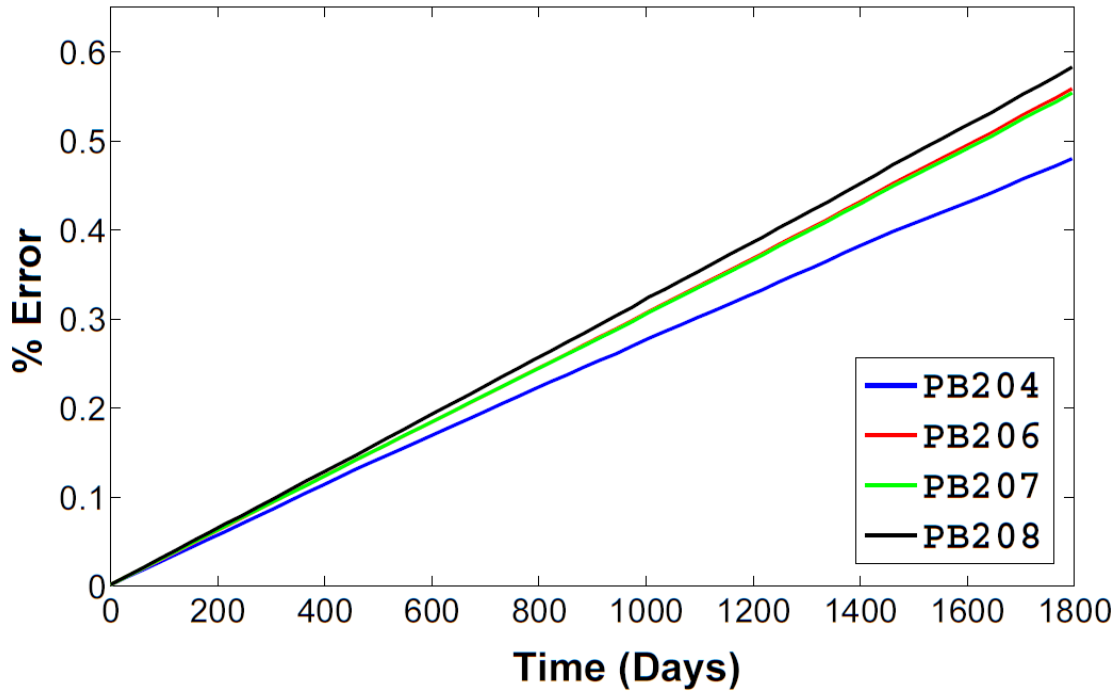

Figure 4.15: VESTA-FATI percentage variation of lead number densities for MCNP cell 6. Depletion calculation performed for 5 years.

Time	^{1}H	^{2}H	^{3}H	^{3}He	^{4}He	^{6}Li	^{7}Li	^{204}Pb	^{205}Pb	^{206}Pb	^{207}Pb	^{208}Pb	^{209}Bi
0	0	0	0	0	0	0.0016	0.0019	0.0016	0.0	0.0016	0.0016	0.0019	0
1	-1.915	1341	2.044	1.352	4.476	-0.0365	0.0102	0.0729	-5.4142	0.0922	0.081	0.1396	-6.4371
2	3.212	1279	3.081	1.491	5.415	-0.2118	0.0193	0.1745	-5.7038	0.1896	0.167	0.2936	-7.2445
3	7.409	1217	4.044	1.261	6.236	-0.5154	0.0284	0.3053	-6.0086	0.2886	0.2547	0.4482	-8.082
4	10.74	1156	5.008	0.624	6.998	-0.9512	0.0399	0.4643	6.3239	0.3915	0.3464	0.6052	-8.8997
5	13.72	1096	6.070	-0.4103	7.777	-1.557	0.0523	0.6485	6.6465	0.4982	0.4396	0.7641	9.7277

Time	^{1}H	^{2}H	^{3}H	^{3}He	^{4}He	^{6}Li	^{7}Li	^{204}Pb	^{205}Pb	^{206}Pb	^{207}Pb	^{208}Pb	^{209}Bi
0	0	0	0	0	0	0.0016	0.0019	0.0017	0.0	0.0016	0.0016	0.0019	0
1	-100.0	2246	-0.8493	-1.069	-0.3616	0.1161	0.1023	0.0958	-1.736	0.1041	0.1040	0.1081	-4.734
2	-26.61	2213	-0.5964	-0.8891	-0.1278	0.2392	0.2143	0.1963	-1.586	0.2148	0.2148	0.2250	-6.197
3	-6.605	2175	-0.3031	-0.7831	0.1380	0.3567	0.3279	0.2935	-1.365	0.3269	0.3254	0.3432	-7.374
4	0.4737	2142	0.0829	-0.6847	0.4768	0.4677	0.4410	0.3902	-1.053	0.4418	0.4394	0.4620	-8.643
5	3.675	2107	0.2676	-0.6204	0.6277	0.5864	0.5548	0.4800	-0.7875	0.5585	0.5539	0.5828	-9.926

Table 4.5: Relative error, E_{Rel}, between VESTA and FATI calculated number densities, N_i, for MCNP cells 3 (top) & 6 (bottom) for a period of 5 years. $E_{\%} = 100 * (N_{MCNPACT} - N_{VESTA})/N_{VESTA}$.

(tabulated data) and FATI (probability tables) will account for some of the differences. The accurate calculation of gas production is important for materials damage in structural components and calculations related to gas separation in the tritium extraction systems. Gas production has a low priority for fission burn-up codes such as VESTA, as gas production has little effect on the fission multiplication constant. The $\sim 10\%$ difference of ^{209}Bi is highly likely to be due to the very fine energy group structure used by VESTA to calculate reaction rates. FISPACT implements a 175 group structure, which is too coarse to accurately decipher the very fine resonance region found in the $^{208}Pb(n,\gamma)$ reaction cross-section which spans five orders of magnitude. This error will then lead to an underestimation of the production of ^{209}Pb, which then beta decays to ^{209}Bi.

The difference in lead isotope number densities are shown in figures 4.14 and 4.15. Both figures shown that all lead errors rise linearly with time at a rate averaging 0.1% per year.

The differences in the Li, Pb and Bi number densities produced by VESTA and FATI can be attributed to dissimilar cross-section data used by each code for some reactions. The burn-up codes used by FATI and VESTA were FISPACT and PHOENIX, respectively. The FISPACT code sources cross-section data from the EASY-2007 database, while PHOENIX sources data from ENDF/B-VII 03C. The MCNP calculations initiated in the FATI code used the 70C cross-sections at 293K (ENDF/B-VII.0 - created by NJOY 99.259), while the MCNP calculations initiated by VESTA used the 03C cross-sections (ENDF/B-VII.0 - created by NJOY 99.248) at 300K. Another factor which is likely to contribute to the slight variation in the number densities produced by each code is the energy binning format. Although each code implements the multi-group binning approach in order to calculate the reaction rates, the FATI binning implements the EAF 175 group structure, while VESTA implements a finely structured 43000 binning structure. The variation of the methods used by FISPACT (numerical time-stepping) and PHOENIX (matrix exponential) to solve the burn-up equations may introduce differences in number density for two reasons. Firstly, the time-stepping method solves a limited number of differential equations due to nuclide truncation whereas the matrix exponential method solves the burn-up equations for all nuclides in the ENDF database. The signatures of the numerical method, such as truncation error, can also cause the weak solution to deviate from the true solution.

4.6 Conclusions

Three aspects of time-dependant spectra effects were presented in section 4.3: a comparison of new and aged neutron spectra on all EAF2005 isotopes; tritium breeding rates and blanket

lifetime; transmutation products within EUROFER steel.

The comparison of individual burn-ups for new and aged neutron spectrum irradiations were used to exemplify, and maximise, the difference in burn-up rates at the start and middle of the blanket's lifetime. Thus, if little difference in burn-up rate is found in this given case the implementation of fully resolved variable spectrum irradiation would result in no additional gain in accuracy. The results of the individual burn-up of all EAF2005 database nuclides showed that the majority of fusion relevant parent isotopes were not sensitive to small changes in neutron spectrum profile.

The study of the convergence of tritium breeding ratio and tritium blanket lifetime showed that the time-stepping with an interval less than 1 month, is essential in order to accurately study tritium production within lithium blankets. The change in TBR's using different time-step intervals is small, however the overall effect on the tritium blanket lifetime is significant given the difference between the single pass and time-stepped lifetimes varied by 70%.

Overall, this study of nuclide depletion within fusion blankets has shown that nuclear reaction rates can change significantly over time and that a single-pass burn model of depletion can underestimate daughter nuclide production by several hundred percent in some cases. Thus, a time interval of one month or less is suggested for depletion studies concerned with tritium production and/or radiation protection studies.

In essence, reaction cross-sections which have a strong 1/v form in the thermal region will require modelling with multiple time-steps. Fissile materials certainly fit into this category. Thus, when modelling fission-fusion hybrids the accuracy of reaction rates would benefit from multiple time-step modelling.

A comparison of nuclide densities over a period of five years has shown that VESTA and FATI produce similar inventories for non-gas nuclides, with associated differences which are well within MCNP and burn-up code standard deviations. The comparisons highlight the differences in gas nuclide treatment between the PHOENIX and FISPACT burn-up codes.

For a simple spherical breeding blanket where the breeding material is lithium-lead eutectic, the differences between the FATI and VESTA lithium and lead nuclide inventories after a period of five years are less than 1%. Gas production rates are generally higher, especially for deuterium, for FISPACT, due to inclusion and omission of gas by-products by FISPACT and PHOENIX respectively. Minor differences in nuclide number densities can be attributed to: the 7K temperature difference in which cross-section data was compiled; the differences in energy group structure required to calculate reaction rates; the variation of energy group structure and the

variation of the methods used to solve the burn-up equations.

4.7 Summary

Both MCNP and FISPACT are both very useful tools in the study of fusion blanket neutronics. However, they are limited to the study of neutron transport or transmutation in either space or time. The study of fusion blanket behaviour requires the knowledge of transmutation in both space and time. Hence, MCNP and/or FISPACT alone cannot be used to study tritium breeding and activation within specified components within a fusion blanket. This problem has been overcome with the development of a depletion linker code, called FATI, which couples MCNP and FISPACT. The code facilitates the calculation of all nuclide production, as a function of time, within any specified MCNP cell. This is achieved by cyclically executing a particle transport run in MCNP, then passing reaction rates and/or neutron spectra to FISPACT for every cell within the MCNP model. Thus, for a MCNP model with n cells of interest, each time-step requires a single MCNP run and n FISPACT runs. The centrepiece of this chapter was the benchmarking of FATI against VESTA. The differences in nuclide number densities over a period of five years was found to be within 1% for the majority of non-gas nuclides, which demonstrates that FATI can be used to simulate blanket behaviour. The differences in the gas production is significantly different, however the reason for this is well understood and can be attributed to the methods used to solve the burn-up equations.

Transmutations within liquid metal blankets will have a negative impact on the tritium breeding capability and the radiological safety of the blanket. Thus, liquid metal blankets will require purification in order to remove dangerous radioactive transmutation products and replenish depleted lithium. The amount of purification required is not well understood and requires detailed modelling. In the next chapter, the FATI depletion code is used in conjunction with a simulated tritium controller in order to model the addition/removal of lithium from the blanket.

CHAPTER 5

TRITIUM BREEDING CONTROL AND IMPURITY REMOVAL

5.1 Impurity extraction and breeding control

The use of liquid metal as coolant/breeding material within IFE blankets is highly likely due to the reduced materials damage [110], reduced radioactive waste for disposal [111], increased availability [112] and online tritium breeding control [26] when compared with solid breeders. The likely candidates for cooling and breeding tritium are FLiBe ($Li_2\,Be\,F_4$) and LiPb (17:83), each of which will burn-up at different rates and produce varying amounts of impurities. The rate at which tritium is to be produced in the blanket must be controlled with precision in order for IFE to become a reliable source of electricity. Hence, a credible control system must be employed in order to manage the production of tritium via the online control of ^6Li ,^7Li and Pb ratios and also control the level of impurities, such as gases and transmutation products, within the liquid metals. Despite the complex nature of radiation transport and nuclide burn-up, this study has empirically found that the TBR and impurity levels are not highly non-linear and can be controlled with rather elementary control theory. The focus of this chapter is the use of control theory applied to the management of tritium production within liquid metal breeding blankets.

In addition to the extraction of hydrogen and helium isotopes from the liquid metal, an additional purification system is needed in order to extract chemically active and hazardous isotopes generated from the transmutation of lead [113]. Such isotopes include bismuth, which produces polonium mainly via $^{208}Pb(n,\gamma)^{209}Pb(\beta)$ $^{209}Bi(n,\gamma)^{210}Bi(\beta)^{210}Po$. However, the $^{209}Pb(n,\gamma)^{210}Pb(\beta)^{210}Bi(\beta)^{210}Po$ reaction chain has a minor contribution, producing the hazardous alpha emitting radio-isotope ^{210}Po which could be inhaled or ingested in the event of accidental release. Other radioactive isotopes which may need to be extracted from the liquid LiPb are the impurities: ^{204m}Pb, ^{203}Pb, ^{203}Tl and ^{203}Hg [114].

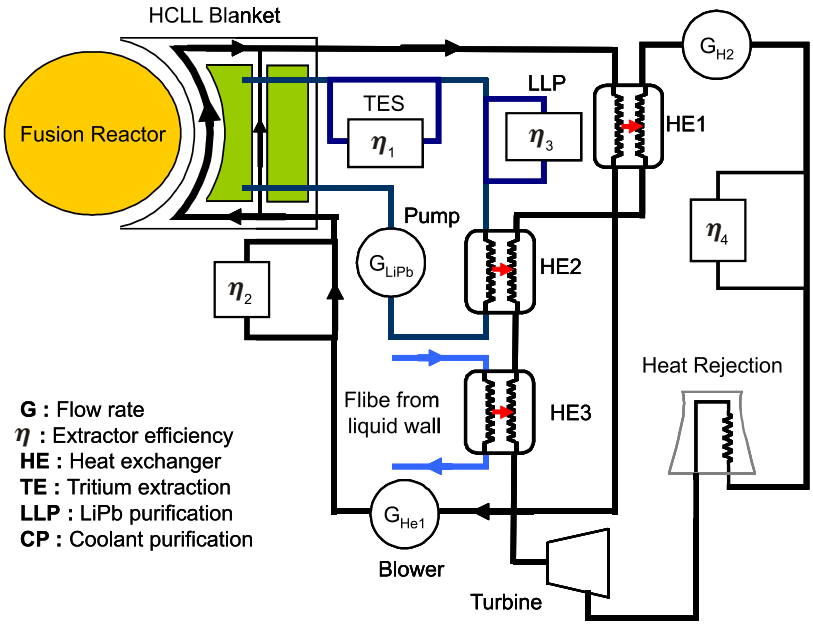

Figure 5.1: The purification and heat extraction system for a helium cooled lithium lead blanket that contains a FLiBe first wall. Adapted from [115]

An issue which was of concern for the modelling of the control system was the distribution of gases throughout the pipes/modules within the tritium breeding components. The simulation of a breeder which has large isotopic concentration gradients would need some aspects of fluid dynamics to be added to the FATI code. However, as a result of high temperature gradients, the upward flow of helium bubbles and convection currents, the tritium concentration within each loop of the blanket can be considered to be homogeneous [49].

Another issue which had to be addressed was the temporal nature of the tritium breeder controller to be used; continuous or discrete. For modelling purposes, if the time required by the controller to purify the liquid breeder, to within acceptable levels, is significantly less than the time-step between consecutive MCNP runs then a discrete controller would be preferable. However, if the purification time is of the same order as the time-step then a continuous controller would be necessary, which would require the development of a new burn-up code. Hence, a discrete controller is preferable due to the limited access to the FISPACT burn-up FORTRAN code and a discrete controller could be implemented between burn-up runs, whereas a continuous controller would have to be implemented in parallel with the burn-up code. Assuming a cold trap is used to purify the liquid alloy, the continuous/discrete issue was addressed by Riemann [56], where the time taken to purify metals was measured to be in the order of hours and a bi-daily purification was suggested. The periodic implementation of the purification allows for

a large enough concentration of tritium to build-up and increase the efficiency of the process. Given that the FATI time-step is in the order of days, the discrete controller is satisfactory.

5.2 Control systems

The main objective of using a control system is the management of actuators in order to achieve the required output response. In order to gain control of the TBR, a closed loop control system is required (as shown in fig 5.2). In a closed loop control system the process output is fed back to the input where it is to be compared to the desired input. The difference between the desired output and the measured output is then used as an input to the controller, which implements a mathematical model designed to govern the actuator in order to achieve the desired output response. The ideal controller has the ability to respond quickly to a sudden change in process output and maintain a steady-state output when the process output is equal to the desired output. This can be achieved by selecting an appropriate mathematical model and fine-tuning the model with appropriate control constants.

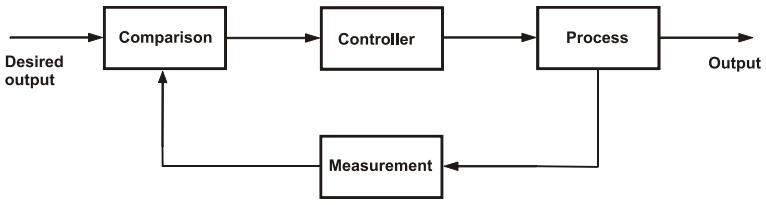

Figure 5.2: Closed loop feedback.

5.2.1 PID controller

The PID (Proportional Integral Derivative) controller is one of the first control strategies to be implemented and is generally accepted to be the most commonly used feedback method [116, 117, 118]. Since feedback controllers first emerged in the 1940's the PID controller has been implemented in various systems which include pneumatic and vacuum devices, analogue electronics and microprocessors.

The output of the PID controller, u(t), is given by:

$$u(t) = K_P e(t) + K_D \frac{de(t)}{dt} + K_I \int_0^t e(t').dt'$$

where e(t) is the error, defined by the difference between the desired output, y(t), and the controller output, u(t), $e(t) = u(t) - y(t)$. The parameters K_P, K_I and K_D are user defined constants relating to the coefficients of the proportional, integral and differential parts of the

controller equation. K_P determines the strength of the response to the error. If K_P is too low, the system will not return to the set point (e = 0) fast enough, too high and the system will oscillate around the set point. K_D and K_I act as damping and driving forces, respectively, that help to settle the error on the set point.

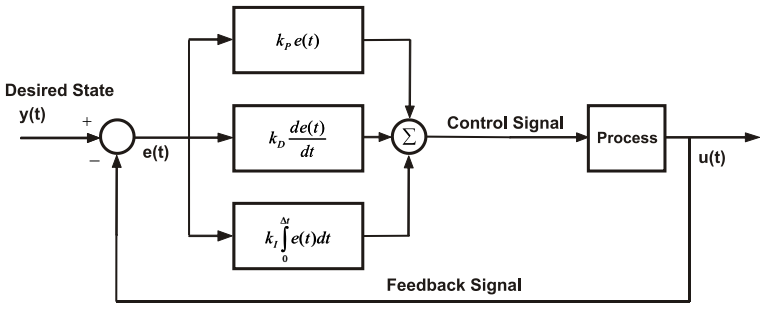

Figure 5.3: PID controller block diagram

The PID control parameters (K_P, K_D, K_I) need to be chosen carefully for many reasons which include:

- Reducing output oscillation in order to minimize the amount of work that needs to be done by the purification system.
- Ensuring that enough tritium is always being produced in order to match/exceed the tritium consumption of the fusion reactor.
- Ensure that too much tritium is not produced, resulting in the contravention of health/safety or tritium licensing rules.

The methods used to determine the control constants can be separated into two categories: Online and Offline. Many online methods exist which include, but are not limited to:

- Trial and error - This is the most simple method of finding the optimum coefficients for the PID. A few simple calculations of required response for a particular error value can determine the starting point for the parameter search. Further perturbation of the coefficients are based on the human observation of properties, such as overshoot or under-damping, of the controller response to the dynamical system.
- Perturbation - This method involves the perturbation of the desired state, u(t), in a predefined manner and measuring the properties of the controller response. Given rules, such as those specified by Ziegler-Nichols [119] or Cohen-Coon [120], the optimum coefficients can be calculated.

- Fuzzy logic - Fuzzy logic is based on the concept of multiple state logic, as opposed to standard binary logic. Fuzzy logic [121, 122] can be used to define which state of operation the PID is to respond to considering the dynamic state of the system. It is particularly applicable to PID controller in which the system dynamics are non-linear, however the TBR response to Li6:Li7 ratio can be considered to be linear, hence the implementation of this method could be considered to be an over-engineered solution.

Due to the long time scales of the tritium production and usage, both in real time and in simulation, online methods of control constant choice are not ideal. Therefore, the control constants must first be calculated analytically and trialed. The perturbation method of Ziegler-Nichols [119], the most employed PID design technique in industry [123], will be used to set the PID control constants for the tritium controller.

The Ziegler-Nichols tuning method [124] comprises of setting the differential and integral coefficients to zero, then gradually ramping the proportional coefficient until the system begins to oscillate. This value, known as the ultimate gain of the controller, K_U, defines the point whereby the controller is marginally stable. Thus, if the proportional coefficient is increased any further, the system will become unstable. The oscillation of the system response is given by f_0. For a PID controller, the Z-N method states that the coefficients should be set to $K_P = 0.6K_U$, $K_I = 2f_0$ and $K_D = 0.125/f_0$. Other similar methods exist which specify alternative coefficients and allow the controller designer to specify the overshoot percentage, however these methods are not required due to the proof of concept nature of this work.

5.3 PID tritium breeding controller

The tritium controller, as implemented in FATI, allows the user to specify the fraction of tritium to be produced in each cell. Thus, the feature allows for several tritium control lines within each blanket system and varying lithium concentration depending on the position and volume of the cell in the blanket. The tritium production target for cell 'i', ${T^i}_{target}$, with a production fraction, f_i, given a total tritium usage, T_{total}, is simply defined as

$$ {T^i}_{target} = f_i T_{total} = f_i \frac{P_f}{E_n} $$

where $\sum f_i = 1$, P_f is the fusion power of the reactor and E_n is the average energy released per fusion neutron. Once the tritium production target has been defined for each cell, the nuclide composition must be changed in order to produce a quantity of tritium which equals ${T^i}_{target}$

in the next time period. For liquid lithium-lead, the ratio of lithium to lead must be kept at a constant 17:83 ratio in order to ensure eutecticity. In a similar way, the ratio of lithium to beryllium and flourine must be set at 2:1:4 to ensure the chemical and physical properties of FLiBe are maintained. Hence, maintaining the correct TBR by altering of the neutron multiplier concentration is not possible for LiPb or FLiBe. As a result, the ratio of ^6Li : ^7Li is the only mechanism by which tritium production can be controlled.

$$R = \frac{N_{Li6}}{N_{Li6} + N_{Li7}}$$

The adjustment of the ^6Li enrichment [26] can be accomplished by employing techniques such as cold traps [125]. A conventional controller, as described in the previous section, varies the control parameter with an infinite scale. However the control parameter, R, is defined in the interval [0,1]. This issue is resolved by introducing a transfer function, F(O), which maps the output of the PID controller, $r^{\infty}{}_{PID}$ to the interval [0,1], creating a variable $R^{[0,1]}{}_{PID}$ which represents Li6:Li7 ratio. In order to ensure controller stability and convergence the transfer function must satisfy the following conditions:

$R \longrightarrow 1$ as $r \longrightarrow \infty$	This ensures that the ratio never exceeds the maximum physical bound of the ratio
$R \longrightarrow 0$ as $r \longrightarrow -\infty$	This ensures that the ratio never exceeds the minimum physical bound of the ratio
$R = R_S$ for r =0	The controller returns no change if the error is zero (current ratio = set point ratio)
$\frac{dR}{dr}\|_{R=R_s} = 0$	The phase plot of the controller must point towards and converge on the set point.
$\left\|\frac{dR}{dr}\right\| < \infty \; \forall r.$	The transfer function must be continuous in order to maintain controller stability.

The transfer function, shown in figure 5.4, is analytically defined as:

$$R = \left\{ \begin{array}{cc} 1 - (1 - R_s)\exp\left(-r^2/\sigma_+\right) & r > 0 \\ R_s \exp\left(-r^2/\sigma_-\right) & r \leq 0 \end{array} \right\}$$

Hence, the procedure for updating the lithium enrichment ratio, R, for each cell (or group of cells) is as follows:

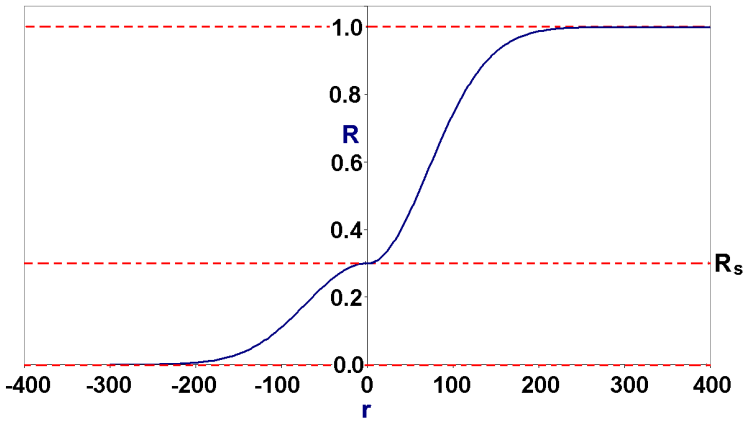

Figure 5.4: Transfer function - mapping ${r^{\infty}}_{PID} \rightarrow {R^{[0,1]}}_{PID}$

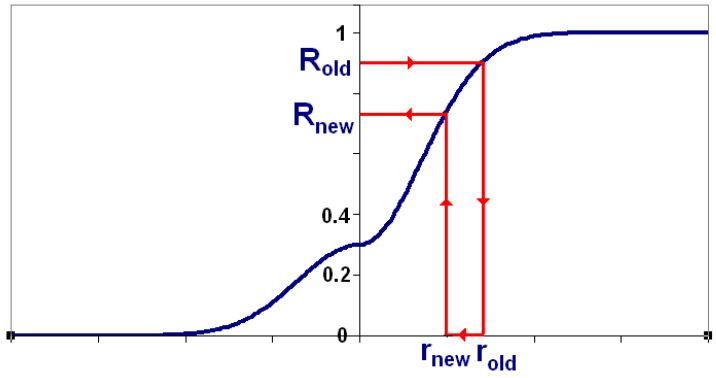

Figure 5.5: Mapping of PID output to Li ratio.

1. Map to current Li6:Li7 ratio, ${R^{[0,1]}}_{old}$, to the infinite range, ${R^{\infty}}_{old}$ using the inverse of the transfer function.

$$ {r^{\infty}}_{old} = F^{-1}({R^{[0,1]}}_{old}) = \left\{ \begin{array}{ll} \left(-\sigma_{+} ln\left[\frac{1-R_{old}}{1-R_s}\right]\right)^{1/2} & R_{old} > R_s \\ -\left(-\sigma_{-} ln\left[\frac{R_{old}}{R_s}\right]\right)^{1/2} & R_{old} \leq R_s \end{array} \right\} $$

2. Calculate the increment in R^{∞}_{old} using PID theory:

$$ \text{Let } E = {T^{i}}_{target} - {T^{i}}_{measured} $$

$$ \triangle r^{\infty} = AE + B\frac{dE}{dt} + C\int_0^{\triangle t} E.dt $$

$$ {r^{\infty}}_{new} = {r^{\infty}}_{old} + \triangle r^{\infty} $$

3. Map the new ratio to the [0,1] interval

$$ R^{new} = \left\{ \begin{array}{ll} 1 - (1 - R_s)\exp\left(-r^2/\sigma_{+}\right) & r > 0 \\ R_s \exp\left(-r^2/\sigma_{-}\right) & r \leq 0 \end{array} \right\} $$

This procedure is illustrated in figure 5.5.

5.3.1 Control constant definition for tritium controller

The tritium controller error is defined as the difference between the desired tritium inventory in storage and the actual tritium amount in storage. Due to the low tritium inventory at the start

of the reactor's operational lifetime the error will be very large. This will result in the controllers ability to maintain numerical stability for only impractically small $\triangle t$. Desired values of $\triangle t$, required for accuracy and computational efficiency, will result in considerable overshoot and high amplitude oscillations in the controller response; this poses a serious risk to controller stability and convergence. The overshoot and oscillation cannot be tolerated in either a research or commercial fusion reactor due to the possibility of exceeding tritium inventory limits specified by the nuclear safety regulators.

This problem can be solved in many ways such as:

1. Limiter - Introducing an error limiter which, as the name suggests, limits the error or the output of the controller to within specified bounds. This could be achieved by mapping the the error or the output to within a specified range using the arctan function. Thus, the output is linear for small errors and converges to a maximum value for high errors. This method has been tested, within this work, but is not consistently stable.

2. Variable control constants - This method is based on using proportional, differential and integral functions of the error rather than predefined constants. These functions could specify that the proportional coefficient be small for larger errors and increases as the error decreases. The differential coefficient could start relatively high and decrease as the error converges to zero. The amount of functions and methods used to vary the PID coefficients with time are plentiful, however this method is considered to be an over-engineered solution to a relatively simple problem.

3. Ramping - In order to reduce the difference between the desired and the actual tritium inventory, the desired tritium inventory can be increased with time such that the final tritium inventory of around 20 kg can be achieved in a controlled manner. A linear ramping function has been tested and works satisfactorily, however it still introduces some oscillations. An exponentially converging function ensures stability and further reduces oscillations in the controller response.

5.4 Modelling tritium control within a LiPb blanket

The main objective of this research is to essentially prove the principal that standard control theory can be applied to regulate the tritium breeding capability and inventory of fusion reactor blankets. Hence, the model used to test the tritium breeding controller is simple in geometry but

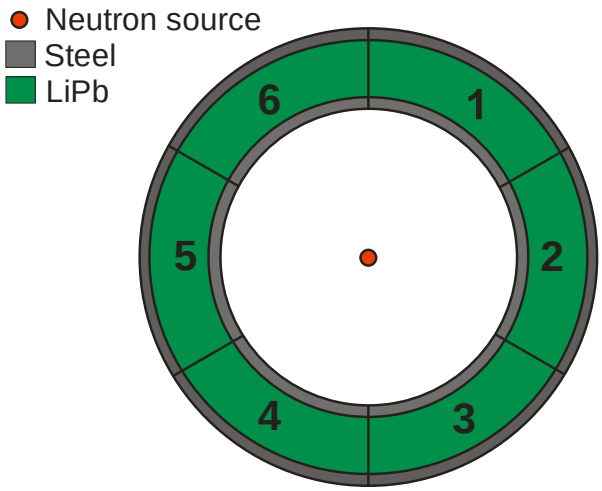

Figure 5.6: Plan view of the spherical segment reactor model.

nevertheless clearly demonstrates, by means of simulation, that a conventional PID controller is capable of managing tritium production in a safe and reliable manner.

5.4.1 Model

Two reactor models will be used to demonstrate the capabilities of the FATI + tritium controller. The first model comprised of a spherical reactor with a self-cooled lithium lead (SCLL) blanket. The blanket comprises of four concentric and individually controlled tritium breeding compartments, each comprised of pure LiPb (17:83) at start-up. In order to ensure that the blanket manufactures enough tritium at the early crucial stage of the reactors lifetime and to demonstrate the controllers capability of managing tritium the Li-6 enrichment is set to 41% at start-up. Preliminary MCNP calculations show that this enrichment results in an initial TBR of 1.09.

The second model is a hollow sphere composed of six 60^o vertically mounted blanket segments, as shown in figure 5.6.

The primary purpose of using the LiPb in its eutectic form is that the material can remain in the liquid state whilst at the lowest possible temperature. Thus, departing from the 17:83 ratio, required for eutecticity, will result in the temperature of the LiPb needing to be increased which will lower the thermal efficiency of the blanket. Therefore, the method of choice for modifying the tritium breeding capability of the blanket is the control of the Li6:Li7 ratio.

The tritium surplus inventory of a commercial fusion power plant is likely to be in the order of 20Kg, while the start-up inventory will be in the order of 100's of grams. Hence, the controller must be able to steadily increase the surplus inventory, by ensuring that the TBR is greater than unity, until the required tritium surplus requirement has been met. The initial difference

between the start-up inventory and the required inventory is large, which with a simple error definition would cause large, and potentially dangerous, overshoot of the tritium surplus. This problem will be eliminated by gradually increasing the required tritium surplus with time in order to ensure that the error does not become too large to cause instabilities in the controller.

$$T^{PID}_{target}(t) = max\,(\,f\,(t),\, T_{target})$$

where T_{target} is the site tritium surplus target, f(t) is a function that ramps up from zero to after a specified time and T^{PID}_{target} is the PID controller target for time = t.

5.4.2 Results - Sectored Spherical Model

Figure 5.7 shows the lithium mass density, within sector 3, as a function of time with the lithium ratio controller in operation. Over a period of approximately one year the lithium mass density converges towards approximately 4.2×10^{-3} atoms/barn/cm of ^{7}Li and 2×10^{-3} atoms/barn/cm of ^{6}Li. The ^{6}Li and ^{7}Li densities are inversely proportional, ensuring that the total lithium density is kept at a constant 17%. The attenuation of the lithium density oscillations is slightly under-damped as further optimization of the PID control constants are required. The total and differential tritium breeding ratios within each of the sectors, shown in figure 5.9, correlate strongly with the ^{6}Li mass density. The TBR oscillations are relatively slow to converge to the required TBR of approximately 1.0, however these oscillations cause less than a 6% overshoot of the tritium surplus inventory, shown in figure 5.8, and reduce to within 3% after 3 months. The PID control constants are not fully optimized, however the results of the sectored spherical blanket model clearly show that a simple PID controller is capable of managing the production of tritium within a Li-Pb tritium breeder.

The number densities of the core LiPb isotopes are also shown in figure 5.7. This figure shows that the lead isotopes are not affected by changes in the ^{6}Li :^{7}Li ratio and that a stable ratio of ^{6}Li,^{7}Li and Pb is found within approximately one year.

A comparison of the tritium and helium-4 production, shown in figure 5.10, indicates that the majority of ^{4}He produced is due to the $^{6}Li(n,\alpha)$ and $^{7}Li(n,n'\alpha)$ reactions due to the strong correlation. The constant ^{4}He offset is mainly due to the $Pb(n,\alpha)$ reactions, although other (n,α) reactions make a small contribution to the helium inventory.

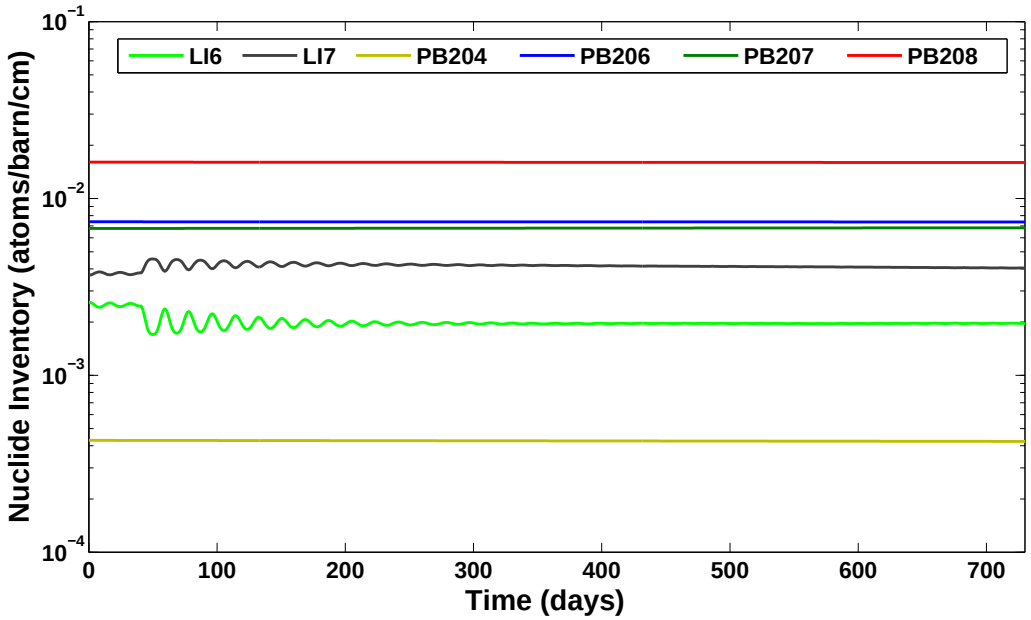

Figure 5.7: A comparison of the primary nuclide densities as a function of time for cell 3 of the segment model.

5.4.3 Results - Concentric Spherical Model - Individually Controlled

Whilst the rotational symmetry of the sectored model resulted in linear tritium breeding dynamics, thus enabling the linear PID controller to be applied successfully, the concentric model introduces coupling between the tritium breeding cells. This can reduce the PID controller's ability to manage the tritium breeding in a way which is practical in terms of operational efficiency/management. However, figure 5.12 shows that the tritium excess can be steadily increased to the required level and stabilised with an acceptable overshoot ($< 8\%$). The differential tritium production, shown in figure 5.11, is stable for all cells however this is not expected for all models/operational scenarios due the non-linear coupling of tritium production for neighboring cells. The differential tritium production within each cell, shown in figure 5.11, shows more non-linearity when compared to its sector model equivalent in figure 5.9.

5.4.4 Conclusion

In order to breed tritium in an efficient and safe manner, a liquid metal breeding blanket will require control theory to adjust the rate at which tritium is being bred. Due to the materials properties of the most common liquid breeders, FLiBe and LiPb, the only variable that can be used to modify the TBR is the ^{6}Li :^{7} Li ratio. In conjunction with the FATI code, two simple spherical models of fusion reactor blankets have been used to demonstrate that a discrete PID controller can effectively govern the rate at which tritium is being produced. In order to

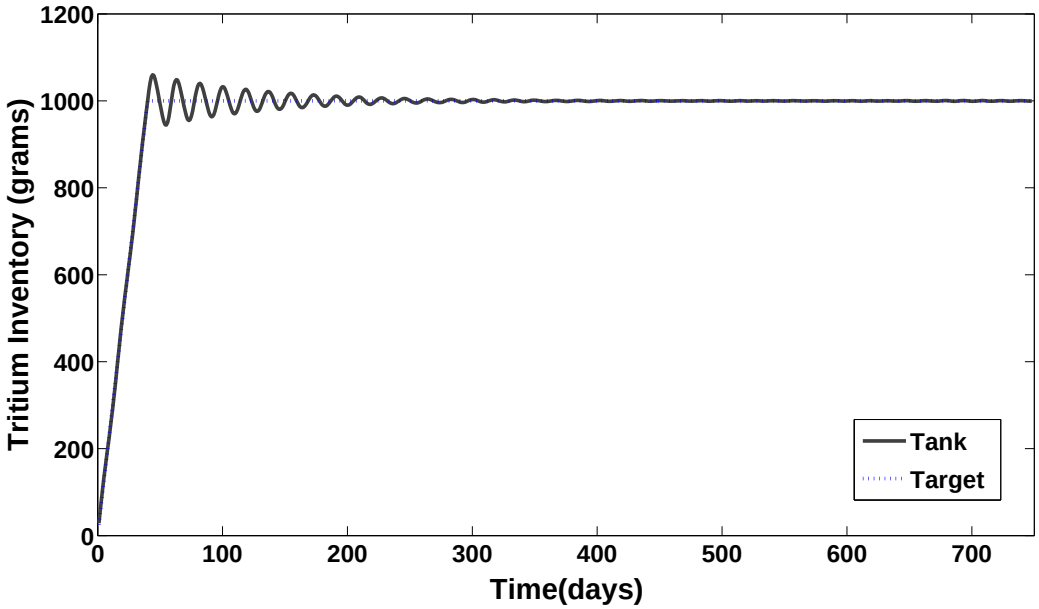

Figure 5.8: Tritium excess inventory with tritium breeding control (sectored model). The tritium tank target increased linearly from 0 to 1Kg over a period of 60 days.

reduce oscillations and overshoot of the controller, a ramp function was implemented to gradually increase the tritium surplus inventory to the required level. For blankets which contain buried layers of tritium breeding cells, evidence of non-linearity of the TBR has not been demonstrated. It is expected that the non-linearity will not be strong for real reactor models where the cells with be distributed in the angular rather than the radial dimensions. However, the exact nature of the non-linearity is currently under investigation. The effect of tritium control on materials damage and radiation protection will be addressed in future work.

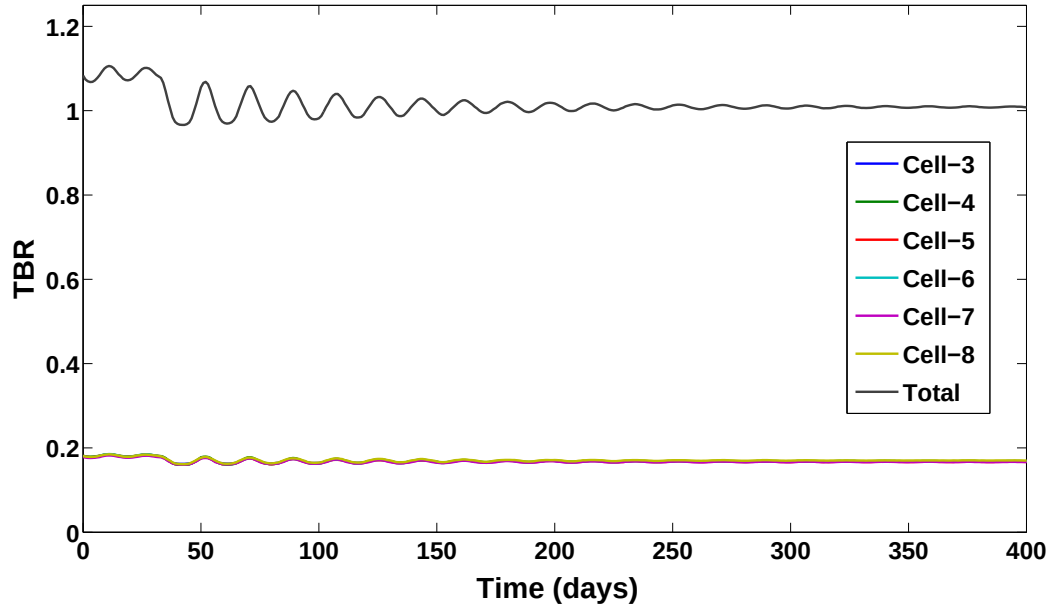

Figure 5.9: Total and differential tritium breeding ratios.

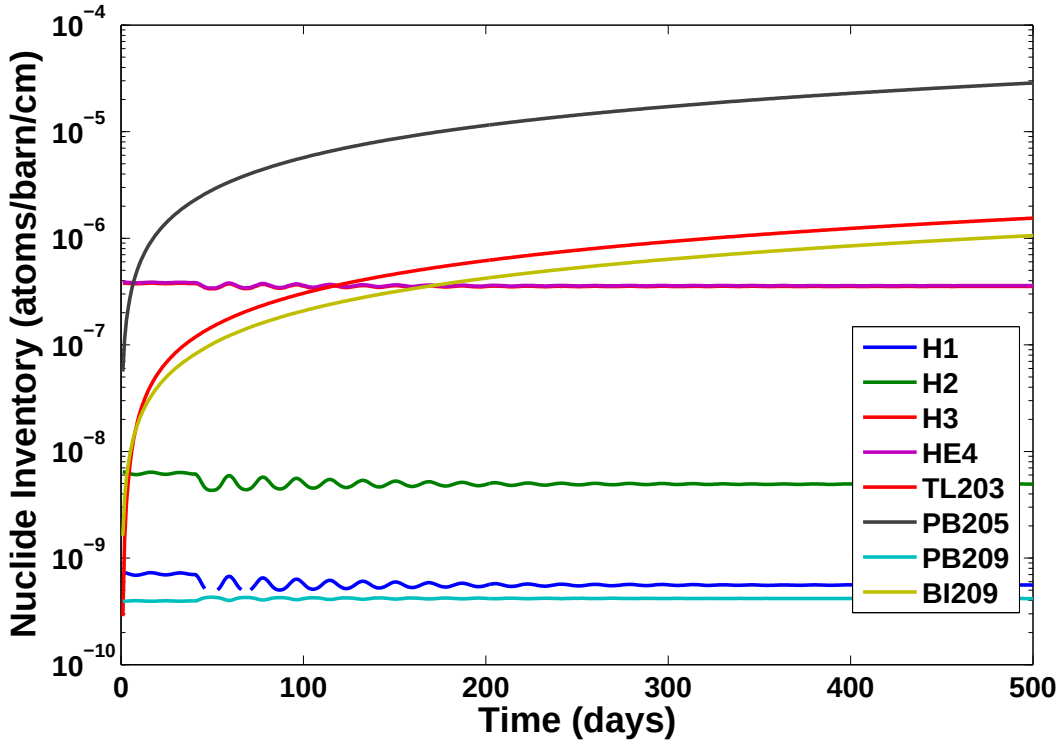

Figure 5.10: A comparison of the daughter nuclides as a function of time for cell 4 of the segment model.

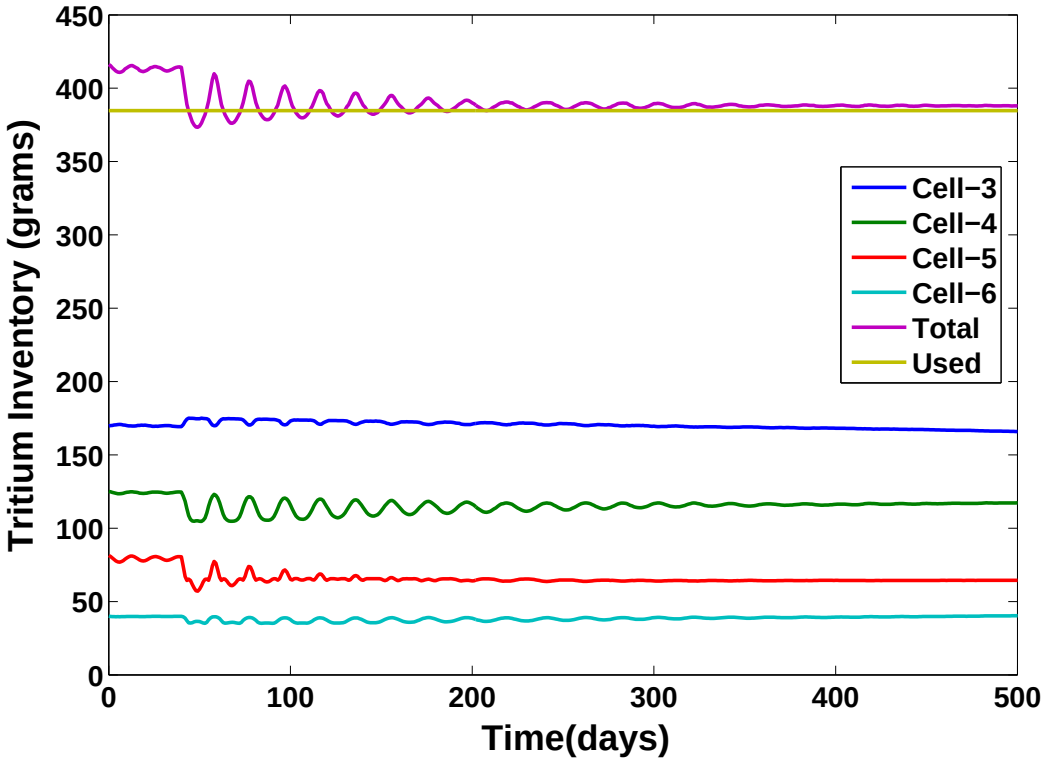

Figure 5.11: Differential tritium production with tritium breeding control (Concentric model).

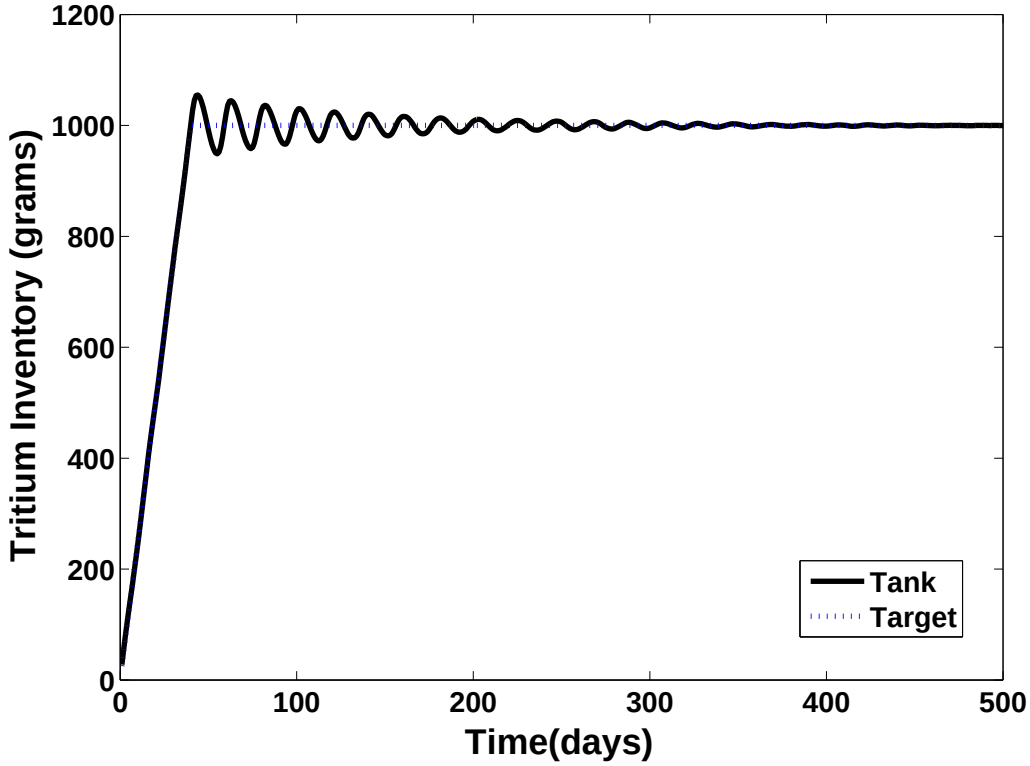

Figure 5.12: Tritium excess inventory with tritium breeding control (Concentric model).

CHAPTER 6

CONCLUSION

6.1 Introduction

The content presented in this thesis is centered around fusion research, with an emphasis on blanket modelling. As the rate of consumption of energy monotonically increases, the need to find new high energy density sources for the production of electricity becomes evermore important. Fusion energy can contribute significantly in this effort. The current routes to commercial fusion are based on the concepts of magnetic and inertial fusion, both of which rely on the reaction between deuterium and tritium to produce heat in the form of fast neutrons. The deuterium fuel required for the reactor is relatively easily extracted from sea water. However, tritium does not naturally occur on earth, hence the manufacture of tritium in sufficient quantities is vitally important to the development and success of fusion as a commercial power source.

Chapter 2 described the physics and technology of breeding blankets - the primary candidate for the production of tritium. This device surrounds the fusion reactor core and mainly comprises of lithium, an element which produces tritium when bombarded by neutrons. The neutrons released by fusion reactions in the core react with the lithium in the blanket, producing tritium which can then be extracted from the blanket and used to fuel the reactor. In order to boost the amount of tritium being produced a neutron multiplier, such as beryllium or lead, is utilized in order to increase the neutron flux within the blanket. Tritium breeding blankets can generally be split into the category of solid or liquid breeders. The solid breeders are technologically simpler than liquid breeders and have a fixed lifetime based on the amount of lithium within the blanket. However they need to be replaced every 5 - 10 years and, over the period of the reactor's lifetime, produce a larger amount of nuclear waste which needs to be geologically disposed. Liquid blankets allow the online adjustment of ^{6}Li :^{7} Li ratio, thus reducing the overall amount of tritium to be stored on-site and reducing the amount of tritium losses due to beta decay.

The fourth chapter is dedicated to the FATI depletion code; A code which can model the rate

of burn-up of nuclides within the blanket and other structural components. This code links the burn-up and particle transport codes, FISPACT and MCNP. The FATI code combines the capability of MCNP to calculate reaction rates as a function of space, with the ability of FISPACT to calculate nuclide inventories with time. This results in a depletion code which can calculate the production of nuclides within specified blanket components as a function of both time and space. The code was benchmarked against a similar code, VESTA (developed at IRSN) which was primarily intended for fission applications. Over a time period of 5 years, the codes were found to compute nuclide number densities which are within 1% for the majority of fusion relevant elements, such as lithium and lead. Due to the difference in the ways in which the burn-up equations are solved in VESTA and FISPACT, the gas production nuclides deviated from 0.41% to 2107 %. The gas production, as calculated by FISPACT, was higher than that of VESTA due to VESTA removing reaction by-products from the burn-up equations to be solved. Hence, the gases produced by (n, p), (n, d), (n, t) and (n, α) are not included in the VESTA nuclide inventory. This a clear example of why a fusion specific burn-up code is required. Gas production will be higher in fusion devices when compared to fission. Calculating gas production is not a priority in the fission industry, where the accurate calculation of K_{eff} takes precedence, whereas it is very important for fusion. Gas production is relatively low, however gas production in structural components could change engineering parameters, which could then compromise reactor safety and operation.

Radiation transport calculations are computationally expensive, therefore the minimisation of reaction rate calculations via Monte-Carlo simulations is desirable. Thus, time intervals between Monte-Carlo simulations should be as large as possible. Thus, Chapter 3 also addresses the effect of neutron spectra on nuclide burn-up on parent and daughter nuclides found in EUROFER steel and the tritium self-sufficiency time of a blanket. Using a spherical reactor geometry with lithium-lead tritium breeding material, a neutron spectrum is computed at time = 0 and time = 2 years after a detailed depletion calculation using 1 day time intervals. These two spectra are then used to calculate reaction rates for every isotope listed within the EAF2005 database using the FISPACT code. The results show that the difference in nuclide number densities are less then 10% for all nuclides within the database and less then 2 % for all fusion relevant nuclides. Using the same methodology as the first model, EUROFER parent and daughter nuclide number densities produced by each neutron spectra are compared. This study found that the change in burn-up for parent nuclides is statistically insignificant. However, the difference in daughter nuclide production is significant, especially for Rh, Ru, Re, Os, Pt and Ir where the differences

range from 20% to 200%. Thus, in order to model the metallurgical properties of steels within fusion blankets over time, a multiple transport-burnup depletion code (such as used by FATI, VESTA or MONTEBURNS) must be implemented. The final part of this convergence study focussed on the effect of the time-step interval (used to update neutron spectra) on the tritium self-sufficiency time of a blanket. The FATI depletion code modelled the same geometry as in part 1 of the study, however time-steps ranging from 1 day to approximately 800 days were used to predict when the blanket would cease to be able to breed enough tritium to sustain the fusion reactor. The single time-step model (i.e. where a constant neutron spectrum is used for the entire simulation) underestimated the tritium self-sufficiency time of the blanket by approximately 70%. Only time-steps less than 1 month produce a lifetime which is within 5% accuracy. Hence, this work suggests that spectra time-stepping is important in the modelling of tritium production with solid breeders.

The default method used by FATI and VESTA to calculate reaction rates is the multi-group binning (MGB) method. The neutron spectrum within each cell of the reactor model is calculated by MCNP and is then passed to the burn-up solver (FISPACT) where the spectrum is convolved with a cross-section of each reaction of interest. The convolution produces a set of reaction rates which can be directly substituted into the burn-up equations, which can then predict the evolution of the number densities of various isotopes over time. Chapter 4 describes this method of reaction rate calculation as well as the more accurate and computationally expensive point-wise estimator (PE) approach. The optimization of the multi-group binning method is then optimized by developing a multi-group binning format which calculates reaction rates to within 5% of the PE whilst employing the minimal number of energy bins as possible in order to reduce computational cost. The theoretical number of bins required for a specific level of accuracy was used as a starting point for a four-stage process of successively reducing the number of potential energy group formats which can be considered to be optimal. The energy group format found, named FOMG (Fusion Optimized Multi-Group), was bench-marked against empirically determined reaction rates from the FNG-W experiments (SINBAD). For foils close to the neutron source, the reaction rate differences were less than 5%. Thus, the agreement of reaction rates were satisfactory. However, the agreement was sub-optimal for foils further away from the target, which is highly likely to be due to the SDEF definition used to define the FNG neutron source.

The final chapter was dedicated to the application of control theory to managing tritium breeding rates. The control theory required to govern tritium breeding rates was introduced and the stability of the schemes was evaluated. Due to the nature of the control variable, $^{6}Li :^{7} Li$, the

controller required an additional transfer function in order to map the standard PID controller output to a ratio and visa-versa, whilst maintaining controller convergence. Given a required tritium inventory of 20 Kg, the PID controller was found to be suitable for meeting this requirement, however the immediate aim of meeting the 20Kg requirement caused severe overshoot of the tritium inventory which is likely to, in practice, result in the contravention of site tritium handling rules. This problem was overcome by implementing linear and exponential ramps which gradually increase the tritium inventory requirement to the specified level, thus ensuring that error never becomes excessive. For a sectored spherical tritium breeding blanket model, the PID controller developed (which is implemented within FATI) was able to increase the tritium surplus inventory to the required level and continuously maintain an average about that required level. Once the measured surplus inventory matched the required inventory a small overshoot evolved (< 10 %) which then forms an exponentially decreasing oscillation centered upon the desired level. For the sectored model the tritium production rates were spread equally between each of the breeding cells. Despite the concentric model meeting the tritium breeding requirements, the concentric nature of the model could potentially introduce coupling between the controller input/outputs, causing the breeding cell nearest to the neutron source to become dominant and cause other TBR solutions to become degenerate.

6.2 Future Work

The development and benchmarking of FATI, presented in chapter 3 of this thesis, could be extended/ improved by: Comparing the FATI and VESTA extraction of specific nuclides from the fusion model; Introducing additional keywords to be allowed in the FATI input MCNP file, such as “LIKE” and “BUT”; Convert the serial FATI code to MPI format, enabling the execution of the code on faster machines; Introduce power output options, such as cell power loads, thus allowing the modelling of fission and fission-fusion hybrids; Add nuclear heating as an optional output; Calculating the energy multiplication factor as a function of time; Allowing the specification of nuclear data files and temperature in a similar manner to VESTA.

The development of the “Fusion Optimised Multi-Group” (FOMG) binning format has limited scope for improvement due to the generalized nature of the optimization, for which measuring the effectiveness of the optimization is difficult and not well defined. In addition to this, the benefits of further optimization, in terms of computational time, is small considering the time required for a Monte-Carlo simulation is in the order of hours and the time required for multi-group binning is in the order of seconds. Thus, further research would be superfluous and, in some

ways, would only result in a superficial additional optimization. However, the optimized energy format is for a generalized fusion reactor geometry and materials, hence the same methodology could be applied to a real reactor geometry when precise modelling is required. The FATI code enables-multiple particle activation and interfaces well with FISPACT 2, which can now model proton, deuteron, helium-3 and triton activation. Hence, an optimal energy bin structure could be found for each particle type in order to reduce the computational time required for light ion activation.

The tritium breeding control work, presented in chapter 5, paves the way for further, in-depth simulations and models of tritium breeding control. The model used to demonstrate the controller concept was relatively simple. Hence, the application of the controller to a rigorously designed IFE reactor model would be an obvious next step in the development of appropriate control systems required for fusion blanket systems. In addition to this, the option of mixing of liquid metals would be a beneficial feature to add to FATI, as reactor blankets are likely to have several liquid metal lines leading to and from individual components within the blanket, which may be connected externally to the blanket. The application of control theory to the efficient removal of impurities could also be an interesting area of research. The coupling of tritium breeding cells could potentially pose a problem for the linear PID controller. Thus, more sophisticated non-linear controller may need to be developed for blanket geometries which include buried cells.

APPENDICES

Appendix A - Mathematical Methods

The burn-up equation (eqn 2.3) has been studied for over a century, hence many methods of solution exist. The most well known is the Bateman solution [91](eqn 6.1), which is a particular solution of the rate equations when no external radiation is present. i.e the rate of change is governed by nuclear decay only.

$$N_i(t) = N_i(t_0)\exp^{-\lambda_i t} + \sum N_j(t_0)\left[\sum \frac{P_{k+1}\left(\exp^{-\lambda_k t} - \exp^{-\lambda_i t}\right)}{\lambda_i - \lambda_k}\prod \frac{P_{l+1}}{\lambda_l - \lambda_k}\right] \tag{6.1}$$

This method is adequate for solving the rate equations for post-shutdown calculations and off-modes during operation. However, more versatile methods such as the numerical solution, matrix exponential method or chain model are able to solve the rate equations when radiation is present and the equations become highly coupled.

A1.1 - Numerical ODE solvers

The most widely used methods of solving ODE's are based on iterative time-stepping techniques, such as Euler, predictor-corrector and Runge-Kutta. The solution at t+Δt, F(t+Δt), is found by advancing the solution at time t, y(t), using an appropriate numerical method. The most simple method for solving an ODE, $\dot{y} = f(t, y)$ is the forward Euler method

$$y_{n+1} = y_n + \Delta t * f(t_n, y_n) \tag{6.2}$$

For systems of equations of the form, $\dot{y_i} = f_i(t, y)$, where the set of functions $f_i(t, y)$ are of a similar order of magnitude this method can be both fast and sufficiently accurate. A problem arises when the set of functions $f_i(t, y)$ span many orders of magnitude, resulting in very small time-steps having to be taken in order to maintain numerical stability. Thus, a large number of time-step advancements must be computed.

FISPACT [92] (pre v2005) used a variant of the Euler method whereby an exponential step length was used [126], as shown in eqn 6.3. This method, as with other numerical methods, suffers with time-stepping restraints. This problem is solved by assuming that some nuclides are stable, thus relaxing some restrictions on the system.

$$y_{n+1} = y_n + \frac{(e^{\Lambda_i \Delta t} - 1)}{\Lambda_i} * f\,(t_n, y_n) \tag{6.3}$$

The new version of FISPACT now implements several high order numerical time-stepping methods.

A1.2 - Matrix Exponential

The nuclide rate equation can be written in matrix form.

$$\dot{N} = AN \tag{6.4}$$

where N is a column vector and A is a matrix. The solution of eqn 6.4 takes the same form as the scalar equivalent [127].

$$N(t) = exp(At)N_0 \qquad N_0 = N(0) \tag{6.5}$$

At the heart of this solution is the exponential of a matrix, which falls into the category of functions of matrices. The computation of the matrix equivalent of f(λ), where f is a complex valued function of a complex variable, is required. The matrix equivalent, f(A), where A is a $n \times n$ matrix, can be defined by non-rigorous means by directly substituting A for λ in the function f. This results in the scalar function f(λ) = λ^2 + 3 λ + 1 being defined as a matrix function by f(A)= A^2 + 3A + I. A number of rigorous definitions exist which define the function of a matrix, none of which are ideal, as suggested by the paper titled "Nineteen dubious ways to compute the exponential of a matrix" [96]. The most efficient/accurate methods (based on [96, 128]) are described in the following section. The two most common approximation methods for computing the matrix exponential (ME) are the Taylor series and the Padé approximation, both of which have an increased computational efficiency when implemented in conjunction with the scaling and squaring algorithm. Approximation methods generally involve the reduction of the complexity of the problem, whilst maintaining accuracy within specified error bounds, in order to achieve higher computational efficiency.

The most computationally simple methods for calculating the ME are the methods of series summation, the most common being the Taylor series expansion

$$\exp(At) = I + tA + \frac{t^2A^2}{2} + \frac{t^3A^3}{6} \cdots = \sum_{n=0}^{\infty} \frac{t^nA^n}{n!} \tag{6.6}$$

Possible problems with this method include the non-convergence and inaccuracies for large values of At. The calculation of ME's for large n is also quite computationally expensive, although the overall speed of this method is relatively quick.

The Padé approximation involves the approximation of an irrational or complicated function with a rational function, which is defined as the quotient of two power series.

$$f(x) = \sum_{i=0}^{\infty} c_i x^i = \frac{\sum_{i=0}^{L} a_i x^i}{\sum_{i=0}^{M} b_i x^i} + O(L+M+1) \tag{6.7}$$

The a_i and b_i coefficients can be calculated by comparing the coefficients of the power series [129].

$$\begin{aligned} a_0 &= c_0 \\ a_1 &= c_1 + b_1c_0 \\ a_2 &= c_2 + b_1c_1 + b_2c_0 \\ a_L &= c_L + \sum_{i=1}^{min(L,M)} b_ic_{L-i} \end{aligned} \tag{6.8}$$

A drawback of this method is that it is only valid near the origin [130], however the scaling and squaring method eliminates this problem by reducing the matrix norm, scaling the domain in such a way that the matrix lies near the origin and returning to the original scaling after the Padé computation has been performed.

The scaling and squaring method [131] is a pre- and post-conditioner for matrix operations. The Taylor series method is not guaranteed to converge or may not converge within a reasonable time if the matrix norm is large due to the ballooning of expansion terms as the series unfolds. This method scales the matrix, before the main matrix operations and reverses the scaling after the matrix operations have taken place. The scaling of the matrix is based on the following matrix identity

$$e^A = \left(e^{A/m}\right)^m$$

The matrix A is scaled, by halving the matrix elements j times until the following condition is satisfied:

$$\|A\|_\infty \leq 1/2$$

The matrix can be re-scaled after the matrix operation by repeated squaring j times. This method can be applied to any approximation method which relies on matrix norm size for a convergent solution.

Two other computationally competitive methods for calculating the matrix exponential are the Eigen and Schür decomposition methods. Decomposition methods tend to be more rigorous in the definition of the matrix exponential when compared to the approximation methods, which generally results in an increased computation time. The main objective of a decomposition method is to split the matrix exponential problem up into smaller sub-problems which rely on particular matrix properties which can simplify the problem. The Eigen decomposition method exploits the fact that the computation of a diagonal matrix exponential is trivial, while the Schür decomposition exploits the reduced complexity of computing a triangular matrix exponential.

This decomposition method exploits the diagonalisation of matrices. If A is $n \times n$ matrix with n distinct eigenvalues, λ_i , and n linear eigenvectors, v_i, then

$$Av_i = \lambda_i \qquad V = (\underline{v}_1, \underline{v}_2 \ldots \underline{v}_n)$$

The matrix, A, may expressed as

$$A = V\Lambda V^{-1} = V * diag\left(\underline{\lambda}_1, \underline{\lambda}_2 \ldots \underline{\lambda}_n\right) * V^{-1}$$

which can also be extended to express A to higher powers.

$$A^2 = V\Lambda^2 V^{-1} = V * diag\left(\underline{\lambda^2}_1, \underline{\lambda^2}_2 \ldots \underline{\lambda^2}_n\right) * V^{-1}$$

$$\therefore A^k = V\Lambda^k V^{-1} = V * diag\left(\underline{\lambda}^k_1, \underline{\lambda}^k_2 \dots \underline{\lambda}^k_n\right) * V^{-1}$$

This result can be inserted into equation 6.6, giving

$$e^A = V * \Lambda * V^{-1} = V * diag\left(e^{\lambda_1}, e^{\lambda_2} \dots e^{\lambda_n},\right) * V^{-1}$$

Once a matrix exponential has been computed it need not be computed again in order to calculate solutions at subsequent time-steps. A matrix identity exists which allows any method of matrix exponential evaluation to allow previous calculations to contribute to current the calculation, iff the matrix is stiff. Despite the "great exponential tragedy" which states exp(A+B)≠ exp(A).exp(B) unless A and B commute, the scalar equivalent does hold. i.e. exp(At+As) = exp(At).exp(As). This identity eliminates the need for successive calculations of any matrix exponential as the matrix exponential can be expressed in the following form:

$$exp\left(At + A\Delta t\right) = exp(At)exp(A\Delta t)$$

This can be extended to

$$exp\left(A\left(t + n\Delta t\right)\right) = exp\left(At\right)\left(exp\left(A\Delta t\right)\right)^n$$

Setting t=0 gives

$$exp\left(An\Delta t\right) = \left(exp\left(A\Delta t\right)\right)^n \tag{6.9}$$

Equation 6.9 results in a more efficient calculation of successive computations of the matrix exponential, as this method requires a single matrix multiplication per evaluation whereas the decomposition methods require two matrix multiplications plus additional matrix construction. A slight drawback of this method is the propagation and multiplication of errors of the initial matrix exponential. However, this drawback can be reduced by ensuring that the initial matrix exponential is calculated using an accurate method.

For post-shutdown calculations and off modes of pulsed systems the input neutron flux to the activation code is zero, which results in the matrix, A, becoming triangular. Parlett's algorithm [132] for computing the function of a triangular matrix, T, exploits the commutivity relation

FT=TF, where F=f(T), and the fact that a function of a triangular matrix is itself a triangular matrix. A summation formula can be derived by solving FT=TF.

$$f_{ij} = t_{ij}\frac{f_{jj} - f_{ii}}{t_{jj} - t_{ii}} + \frac{1}{t_{jj} - t_{ii}} \sum t_{ik} f_{kj} - f_{ik} t_{kj}$$

A1.3 - Comparison of Methods

The numerical results presented in this section compare the Taylor, Pade, Eigen and Schur decomposition methods in terms of their accuracy and speed. The comparison was made using the MATLAB code which was executed on a single core, 32 bit processor. The decomposition methods used the in-built MATLAB functions, which utilize highly optimized FORTRAN libraries.

A1.3.1 Simple 8 Nuclide Example

This first numerical experiment simply calculates the solution of equation 6.4. N is defined as a column vector of size 8, N(0) = rand[0.4], A is an 8x8 matrix and A = rand[-0.2,+0.2]. The Taylor method was used to calculate the matrix exponential. The series was terminated when the matrix norm of the expansion term was close to machine precision.

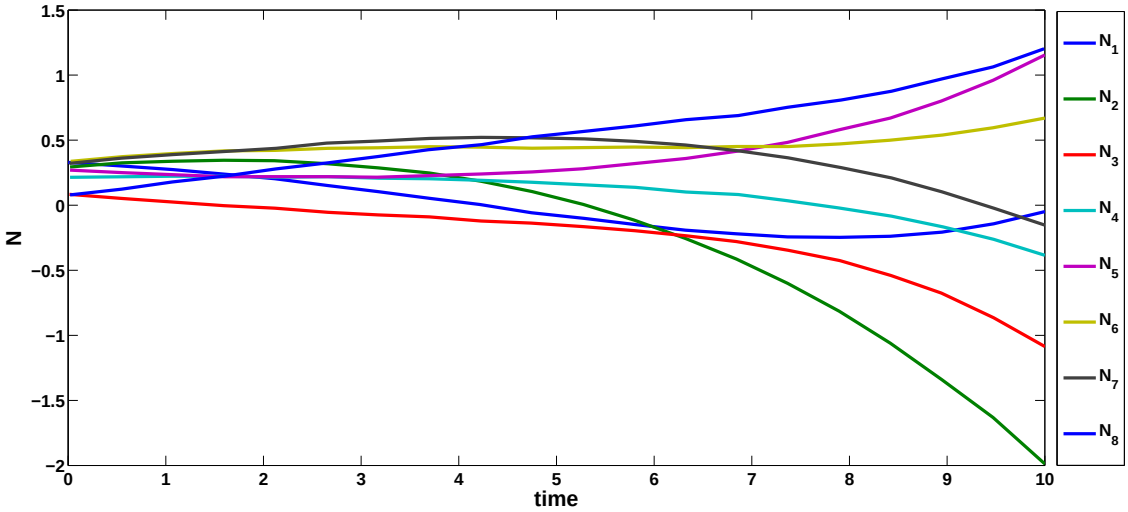

Figure 6.1: The solution of equation 6.4 computed using the Taylor series ME.

A1.3.2 Accuracy

The error, E, is based on the Frobenius norm and is defined as:

$$E = \frac{1}{N} \sum (F_{ij} - f_{ij})^2 \tag{6.10}$$

where A is a $n \times n$ matrix, f = exp(A) is a high precision calculation of the matrix exponential calculated to within machine precision and F is the matrix exponential calculated using Taylor, Pade, Eigen or Schur methods.

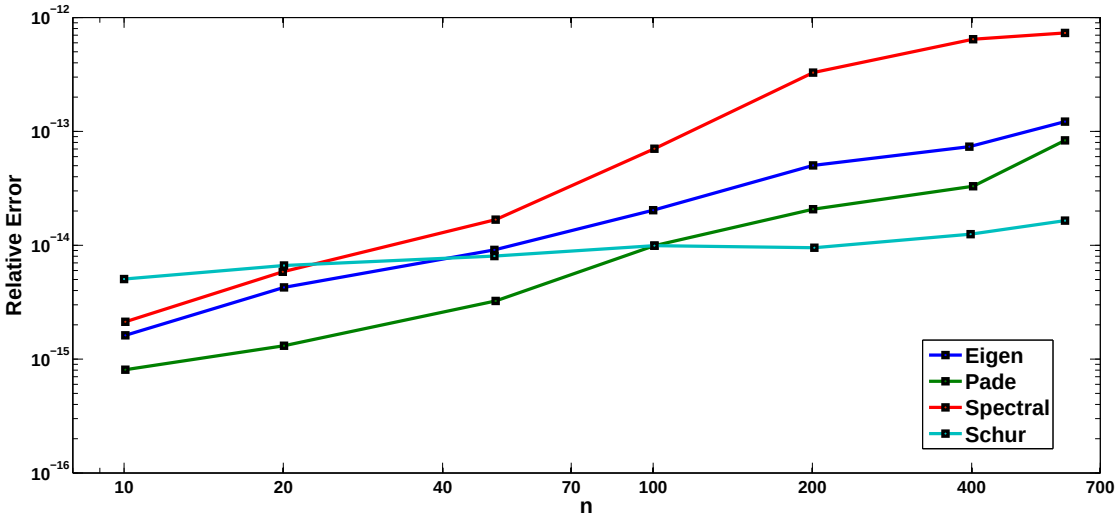

Figure 6.2: The relative error of methods used to calculate the matrix exponential as a function of matrix size.

A1.3.3 Computation Time

The algorithm run time is calculated using the TIMEIT function, available from the MATLAB Exchange (http://www.mathworks.com/ matlabcentral/ fileexchange/18798).

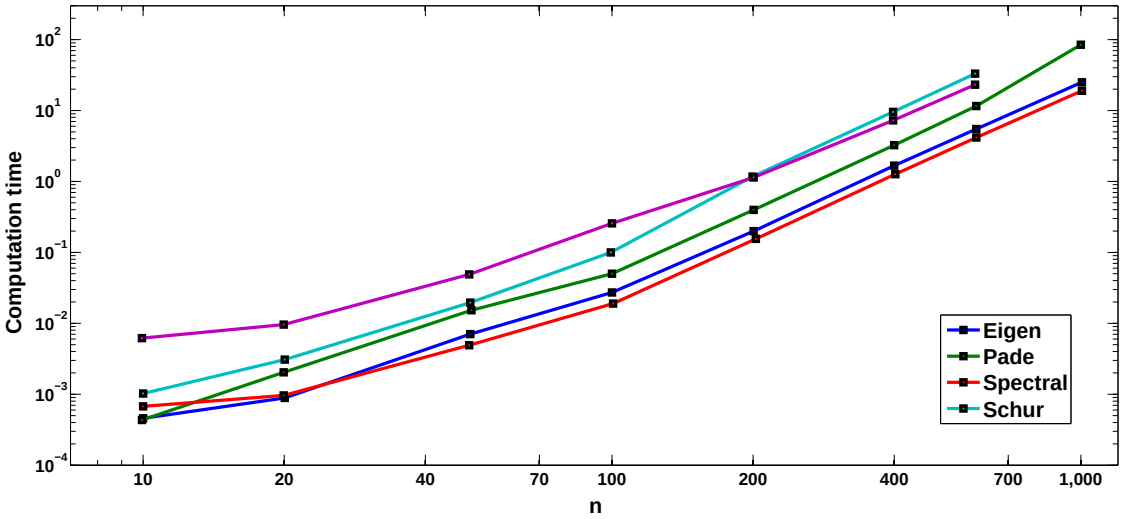

Figure 6.3: The computation time of methods used to calculate the matrix exponential as a function of matrix size.

A1.3.4 Comments on the methods of solving the rate equations

The numerical solution of ODE's via the numerical route has the advantage that it is easily capable of solving systems of ODE's whereby the number of ODE's is increasing, as with the transmutation equations, where the number of nuclides in the system can increase. The matrix exponential method of solving ODE's may be quicker and more accurate for fixed systems of equations, but this cannot be assumed when the number of variables in the system is increasing, due to the matrix exponential needing to be re-calculated every time the number of variables in the system changes. As yet, no activation code exists that implements the matrix exponential method which can efficiently solve the rate equations when the number of variables and equations is increasing.

APPENDIX 2 - FATI Manual

The FATI (Fusion Activation and Transport Interface) code requires two input files: The FILES file and PARAM_INPUT file.

A3.1 - FILES File

The "FILES file" defines the files/directories that FATI are dependent on. Once the FILES file has been configured properly it should not need to be altered.

- FISPACT_DIRECTORY - The directory which contains the FISPACT executable.
- FISPACT_INPUT - The name of the input file named in the FISPACT "FILES" file.
- FISPACT_OUTPUT -The name of the output file named in the FISPACT "FILES" file.
- FISPACT_TAB1 - The name of the TAB1 file named in the FISPACT "FILES" file.
- MCNP_DIRECTORY - The directory which contains the MCNP executable
- MCNP_XSDIR - The pathname of the MCNP XSDIR file
- MCNP_TEMPLATE - The name of the MCNP input file which is to be used as a template by FATI.

Example input file:

FISPACT_DIRECTORY C:\easy-2007\fispact

FISPACT_INPUT co

FISPACT_OUTPUT output

FISPACT_TAB1 tab1

MCNP_DIRECTORY C:\MCNP

MCNP_XSDIR C:\MCNP\mcnp5\Testing\VALIDATION_SHIELDING\xsdir

MCNP_TEMPLATE input1

A.3.2 - PARAM_INPUT File

The program input parameters are specified by an input file "PARAM_INPUT". This input file is used to specify the following parameters:

- **PULSED** (Boolean) - Defines whether the irradiation source is continuous or pulsed. TRUE = Pulsed, FALSE = Continuous.
- **NEUTRON_ENERGY** (Double) - Defines the maximum energy of the neutrons emitted from the source. Energy must be specified in Joules.
- **NEUTRON_POWER** (Double) - Defines the thermal energy of the reactor delivered by neutrons alone (i.e. approx 80% of thermal power). Power must be specified in Watts.
- **PULSED_OFF** (Double) - Defines the temporal length of the "off period" during pulsing. To be used in conjunction with PULSED_OFF_UNIT. This value must be set to zero if PULSE = FALSE.
- **PULSED_ON** (Double) - Defines the temporal length of the "on period" during pulsing. To be used in conjunction with PULSED_ON_UNIT.
- **PULSED_OFF_UNIT** (String) - Defines the temporal unit used to describe the PULSED_OFF period. Allowed units are: Minutes, Hours, Days, Years.
- **PULSED_ON_UNIT** (String) - Defines the temporal unit used to describe the PULSED_ON period. Allowed units are: Minutes, Hours, Days, Years.
- **BURN_CELLS** (Vector Integer) - This keyword allows the user to specify which cells within the MCNP model should undergo burn calculations.
- **BURN_CELLS_PARTICLE** (Vector character) - Specifies the type of irradiation associated with each burn cell. Neutron (N), Proton (H), Deuteron (D) and Triton (T).
- **NO_OF_ITERATIONS** (Integer) - The amount of time-steps to be used for the simulation.
- **MCNP_Update** (Integer) - This specifies the amount of iterations after-which the flux spectrum is updated.
- **FISPACT_MIND** (Double) - This is the cut-off number density to be used with FATI/FISPACT burn-up simulation (i.e. the lowest number density at which a nuclide appears in the FISPACT nuclide output list).
- **TRITIUM_CONTROL** (Vector integer) - Specifies the cells in which the tritium controller is to be operational.
- **TRITIUM_CONTROL_FRACTION** (Vector double) - Specifies the the fraction of tritium to be bred in each of the cells listed in TRITIUM_CONTROL.
- **TRITIUM_CONTROL_S** (Integer) - Specifies the iteration at which the tritium controller is switched on.
- **TRITIUM_CONTROL_F** (Integer) - Specifies the iteration at which the tritium controller is switched on.
- **SET_POINT** (Double)- The $^{6}Li : {}^{7}Li$ ratio which results in a TBR of unity.
- **FILL** (Boolean)- Determines whether mass removed from the blanket is replaced with new material.
- **FILL_NUCLIDE_NAMES** (Vector string) - The names of the nuclides which are to replace nuclides which have been extracted from the system.

- **FILL_NUCLIDE_FRACTION** (Vector double) - The number fraction of the nuclides which are to replace nuclides which have been extracted from the system.
- **EXTRACT** (Boolean) - Determines whether the tritium breeding material is to be purified at each time-step.
- **TARGET_NUCLIDE_NAMES** (Vector string) - A list of nuclides (in symbolic form i.e. Be9) which are subject to be extracted if their number density raises above the thresholds specified by TARGET_NUCLIDE_ND.
- **TARGET_NUCLIDE_ND** (Vector double) - The number density thresholds of nuclides to be extracted.
- **TARGET_NUCLIDE_CONSTS** (Vector double) - The proportion of the excess above the threshold which is to be extracted from the system.
- **TANK_INVENTORY_NAMES** (Vector string) **-** The names of nuclides which reside in the tank at time = 0.
- **TANK_INVENTORY_MASS** (Vector double) **-** The mass of nuclides which reside in the tank at time = 0.
- **NUCLIDES_OF_INTEREST** (Vector string) - The list of nuclides whose number densities are to be automatically tracked.
- **TRITIUM_EFFICIENCY** (Double) - A factor with an interval [0,1] which allows for losses of tritium.
- **TRITIUM_TANK_MASS** (Vector double) - This specifies the target mass of tritium to be stored in the "tank".
- **RATE_TRANSFER** (Boolean) - Specifies whether reaction rates tallied in MCNP override the default multi-group binning approach to calculating reaction rates (this can cause MCNP/FATI to become very slow).
- **CP_MODEL_PULSES** (Integer) - Determines the number of pulses used with the CP model
- **CP_MODEL_UNIT** (string) - Determines the temporal unit of the pulsing used with the CP model
- **CP_MODEL_ON** (Double) - Determines the temporal duration of the “on” period of the pulsing used with the CP model
- **CP_MODEL_OFF** (Double) - Determines the temporal duration of the “off” period of the pulsing used with the CP model
- **PULSED** (Boolean) - Specifies whether the irradiation is continuously on (TRUE) or pulsed (FALSE)
- **NPS** (integer) - The number of particles to be used in each MCNP run.
- **DENSITY_UPDATE** (Boolean) - Determines whether the change in material composition with effect the material density.
- **COVERAGE_FACTOR** (DOUBLE) - A factor with an interval [0,1] that scales the flux magnitude in order to account for regions of diagnostic equipment within the blanket.

- ***** - Comments can also be used on any line providing they are preceded by an asterisk.

Example input file:

— * * INPUT FILE TO SPECIFY PARAMETERS FOR THE MCNPACT PROGRAM * *———

NEUTRON_ENERGY 2.2496E-12 * The energy in Joules of the neutron released from fusion
NEUTRON_POWER 2.0E9 * 2.8759E9 * * 7.660046E7 * The thermal power released by the fusion reactor
PULSED_OFF 0.0 * the dwell period between the on times
PULSED_ON 1.0 * 472.6 *
PULSED_ON_UNIT days *
PULSED_OFF_UNIT days *
NO_OF_ITERATIONS 3000 *
MCNP_UPDATE 3000 * Number of iterations between mcnp updates *
BURN_CELLS 3 4 5 6 *
BURN_CELLS_PARTICLE N N N N *
FISPACT_MIND 1E14 *
TRITIUM_CONTROL 3 4 5 6 10 *3 4 5 6 7 8 * 3 4 5 6 * 2 3 22 23 * 3 4 5 6 * dummy cell to prevent tritium control working but prevents from crashing *
TRITIUM_CONTROL_FRACTION 0.05 0.20 0.50 0.25 0.0 * 0.1666 0.1666 0.1667 0.1667 0.1667 0.1667 *
TRITIUM_CONTROL_S 1000000 *
TRITIUM_CONTROL_F 1000000
TRITIUM_CONST_1 0.85 0.2 0.45 40000.0 60000.0 * 0.008 0.002 0.0015 40000.0 60000.0 *
TRITIUM_CONST_2 0.85 0.2 0.45 40000.0 60000.0
PID_CONST_BOUND 1.03
SET_POINT 0.27 *
FILL FALSE *
FILL_NUCLIDE_NAMES LI6 LI7 PB204 PB206 PB207 PB208 *
FILL_NUCLIDE_FRACTION 0.001 0.079 0.013 0.22172 0.203 0.482 *
EXTRACT TRUE *
TARGET_NUCLIDE_NAMES H1 H2 H3 HE3 HE4 *
TARGET_NUCLIDE_ND 0.0 0.0 0.0 0.0 0.0 *
TARGET_NUCLIDE_CONSTS 1.0 1.0 1.0 1.0 1.0 *
TANK_INVENTORY_NAMES H1 H2 H3 HE3 HE4 LI6 LI7 PB204 PB206 PB207 PB208 *
TANK_INVENTORY_MASS 0.0 0.0 0.0 0.0 0.0 0.0 0.0 0.0 0.0 0.0 0.0 *
NUCLIDES_OF_INTEREST H1 H2 H3 HE3 HE4 LI6 LI7 BE9 O16 TL203 TL204 TL205 PB204 PB205 PB206 PB207 PB208 PB209 BI208 BI209 PO210
TRITIUM_EFFICIENCY 1.0 *
TRITIUM_TANK_MAX 1000.0 *1000
TRITIUM_TANK_CONST 25 *
MAX_RATIO 0.98 *
MIN_RATIO 0.02 *
RATE_TRANSFER FALSE *
CP_MODEL_PULSES 100 *
CP_MODEL_UNIT SECONDS *

CP_MODEL_ON 1E-8 *
CP_MODEL_OFF 0.12499989 *
PULSED FALSE NPS 500000 * 20000
DENSITY_UPDATE FALSE * specifies whether nuclide fraction updates have any effect on the material density
COVERAGE_FACTOR 0.85 * NOT YET IMPLEMENTED!! a la Lee Packer J. Nuc. Materials 417 (2011)
AVAILABILITY 1.00 * NOT YET IMPLEMENTED!!
* COMMENTS HERE * COMMENTS ALWAYS PRECEDED WITH STAR
*————————- * * MCNPACT INPUT FILE END * *————————————

DEFINITIONS: ABBREVIATIONS AND ACRONYMS

Symbol	Description
EUROFER	Low activation steel
FLiBe	A compound of fluorine, lithium and beryllium used for breeding tritium
LiPb	A liquid metal containing lithium and lead used for breeding tritium
HCPB	Helium cooled pebble bed
DCLL	Dual cooled pebble bed
PWR	Pressurised water reactor
NJOY	A nuclear data processing code
ENDF	A nuclear data format
EAF	European activation file
ELM	Edge localised mode
ITER	An international fusion research experiment in Cadarache, France.
DEMO	A fusion power plant that is to succeed ITER
ICF	Inertial confinement fusion
MCF	Magnetic confinement fusion
IFE	Inertial confinement energy
MFE	Magnetic confinement energy
FPY	Full power year
MHD	Magneto-hydro-dynamic
GIMM	Grazing incidence metallic mirror
TBR	Tritium breeding ratio
TSST	Tritium self-sufficiency time
EW	Exempt waste
WDR	Waste disposal rating

DEFINITIONS: ABBREVIATIONS AND ACRONYMS CONT.

Symbol	**Description**
CI	Clearance index
LLW	Low level waste
HLW	High level waste
ILW	Intermediate level waste
MC	Monte Carlo
ACAB	Burn-up code written at Universidad Politecnica de Madrid
CCFE	Culham Centre for Fusion Energy, UK
IRSN	Institute for Radiological Protection and Nuclear Safety, France
LANL	Los Alamos National Laboratory, USA
LLNL	Lawrence Livermore National Laboratory, USA
TART	Neutron transport code written at LLNL
PHOENIX	Burn-up code written at IRSN
VESTA	Transport-burn-up coupling code written at IRSN
ORIGEN	Burn-up code written at LANL
MCNP	Transport code written at LANL
FISPACT	Burn-up code written at CCFE
FATI	Transport-burn-up coupling code written by the author

DEFINITIONS: SYMBOLS (MATHEMATICAL)

Symbol	Description
ρ_{hs}	Density of "hot spot" with ICF capsule
r_{hs}	Radius of "hot spot" with ICF capsule
R	Reaction rate per unit volume
$< \sigma v >$	Single group (effective) cross-section
N_i	Number density of nuclides with species "i"
V	Volume
τ	Confinement time
Q	Energy released per fusion reaction
t	Time
r	Radius
C_s	Speed of sound
E_{out}	Fusion energy released from burning 100% of fuel within ICF capsule
f_B	Fraction of fuel burned within ICF capsule
T	Temperature
β	Effective density-radius product of non-burned fuel in capsule
E_H	Thermal energy needed to initiate fusion burn in an ICF capsule
η_{bf}	Efficiency of beam-fuel coupling
η_d	Efficiency of ICF driver
E_{in}	Energy required by ICF driver in order to initiate fusion burn
Y	Fusion yield
ϕ	Neutron flux
m_i	Mass of nuclide 'i'

DEFINITIONS: SYMBOLS (MATHEMATICAL) CONT.

Symbol	Description
u	Lethargy
$V_{i,CoM}$	Initial velocity of nucleus in CoM frame
$V_{f,CoM}$	Final velocity of nucleus in CoM frame
$v_{i,CoM}$	Initial velocity of neutron in CoM frame
$v_{f,CoM}$	Final velocity of neutron in CoM frame
V_{CoM}	Velocity of CoM
$V_{f,Lab}$	Final velocity of nucleus in Lab frame
$v_{i,Lab}$	Initial velocity of neutron in Lab frame
$v_{f,Lab}$	Final velocity of neutron in Lab frame
$v_{C,Lab}$	Velocity of compound nucleus
θ_{Lab}	Neutron scattering in angle in Lab frame
θ_{CoM}	Neutron scattering angle in CoM frame
m_A	Mass of nucleus
m_n	Mass of neutron
A	$M_{nucleus}/M_{neutron}$
θ	Scattering angle of neutron
Ω	Solid angle subtended by the scattering angle θ
ξ	Lethargy per collision
k_B	Boltzmann constant
v_{th}	Thermal speed of atoms in crystal
M	Energy multiplication factor in blanket
K_{i-j}	Sieverts constant for species 'i' in material 'j'

DEFINITIONS: SYMBOLS (MATHEMATICAL) CONT.

Symbol	Description
R	Universal gas constant
S_i	Specific activity of material 'i'
L_i	Waste disposal limit of material 'i'
λ_i	Decay constant of nuclide 'i'
σ_i^T	Microscopic cross-section of reaction type 'T' in nuclide 'i'
F	Number of flops required per calculation
Q	Size of matrix
n	Ratio of number of flops required by analytic and numerical methods
ψ_p	Neutron flux of ICF pulse
ψ_{SS}	Equivalent steady state neutron flux
$\triangle$	Down time between ICF pulses
$\bigtriangledown$	Time duration of a single ICF pulse
r	position vector
v	velocity
φ	Angular neutron flux
Σ	Macroscopic neutron flux
S	neutron source term
P	Number of particles (histories) in MC simulation
ds	Distance travelled by neutron with velocity,v, in time, dt.
W	Weight of particle used in MC simulations
M	Monte carlo operator
B	Burn-up operator

DEFINITIONS: SYMBOLS (MATHEMATICAL) CONT.

Symbol	**Description**
N_{Diff}	Percentage difference in number density
u(t)	Output of PID controller
K_P	Proportional coefficient used in PID controller
K_I	Integral coefficient used in PID controller
K_D	Differential coefficient used in PID controller
y(t)	Desired output of controller
e(t)	Difference/error between real and desired output of PID controller
R	Ratio of ^{Li6}N : $(^{Li6}N + ^{Li7}N)$
f_i	Fraction of total tritium that is produced by cell 'i'
r	mapping variable to be used to define R

DEFINITIONS: SYMBOLS (NUCLEAR)

Symbol	**Description**
β	Beta (electron) particle
α	Alpha particle
P	Proton
D	Deuterium
T	Tritium
n	Neutron
n'	Scattered neutron

BIBLIOGRAPHY

[1] Nation Physical Laboratory. Fusion reactions of CTR interest.

[2] Y. Kawamura. Research and development of the tritium recovery system for the blanket of the fusion reactor in jaea. *Nucl. Fusion*, 49:17–31, 2009.

[3] M. Abdou. Us participation in the iter test blanket module program.

[4] C W Gordon and A A Harms. Comparative energetics of three fusion-fission symbiotic nuclear reactor systems. *Nuclear engineering design*, 34:269, 1975.

[5] L M Lidsky. Fission-fusion systems: Hybrid symbiotic and augean. *Nuclear Fusion*, 15:151, 1975.

[6] M M H Ragheb. Implementation considerations of coupling dedicated fissile and fusile production fusion and fission reactors. *UWFDM*, 309:9, 1978.

[7] P.Gierszewski R.-D. Penzhorn C.H. Wu D.K. Murdoch, Ch. Day. Tritium inventory issues for future reactors: choices, parameters, limits. *Fusion eng. Des*, 46:255–271, 1999.

[8] R. L. Park. Voodoo science: the road from foolishness to fraud. page 17, 2000.

[9] L G Christoporou. Place of science in a world of value and facts. page 46, 2001.

[10] N A Downie. Industrial gases. *Knlewer Academic Publishers Group*, page 137, 1996.

[11] J Lindl. Development of the indirect drive approach to inertial confinement fusion and the target physics basis for ignition and gain. *Phys. Plasmas*, 2:3933–4023, 1995.

[12] S. Atzeni and J Meyer ter Vehn. The physics of inertial fusion. *Oxford Science publications*, page 31, 2004.

[13] USA Laboratory for Laser Energetics (LLE), University of Rochester. Indirect-drive target.

[14] E. R. Harrison. *Phys. Rev. Lett.*, 11:535, 1963.

[15] C. Maisonnier. *Nuovo Cimento*, 42:332, 1966.

[16] Mordecai D. Rosen. The physics issues that define interial confinemtn fusion gain and driver requirements: A tutorial. *Phys. Plasmas*, 6:1690–1699, 1999.

[17] J A Frenje et al. First measurements of the absolute neutron spectrum using the magnetic recoil spectrometer(mrs) at omega(invited). *Rev. Sci. Instrum.*, 2008.

[18] Tatjana Jevremovic. *Nuclear Principles In Engineering.* Springer.

[19] L J Hamilton J J Duderstadt. *Nuclear Reactor Analysis.* Wiley and Sons.

[20] M. Houry D. Riz, F. Garaude and B.Canaud. Neutron and photon emission of a high-gain direct-drive target for laser fusion. *Nucl. Fusion*, 46:864–867, 2006.

[21] J. Nuckolls. Laser compression of matter to super-high densities: Thermonuclear (ctr) applications. *Nature*, 239:139, 1972.

[22] P Reuss. *Neutron Physics.* EDP Sciences, 2008.

[23] L J Hamilton J J Duderstadt. *Nuclear Reactor Analysis.* Wiley and Sons, 1976.

[24] L.W. Packer. Progress of recent neutronic anlysis for demo concepts. *UKAEA 13th neutronics progress meeting*, 2008.

[25] D Maisonnier. The european power plant conceptual study. *Fusion Eng Des*, 75.

[26] S. Malang L.A. El-Guebaly. Towards the ultimate goal of tritium self-sufficiency; technical issues and requirements imposed on aries advanced power plants. *Fusion Eng. Des.*

[27] William Kuan and Muhamed A Abdou. A new approach for assessing the required tritium breeding ratio and startup inventory in future fusion reactors. *Fus tech*, 35:309–353, 1999.

[28] Y. Gohar and D.L. Smith. Multiplier, moderator and reflector materials for advanced lithium-vanadium fusion blankets. *ICFRM*, 9, 2000.

[29] Y. Gohar. An assessment of neutron multipliers for dt solid breeder fusion reactor. *Transactions of American nuclear society*, 34:52, 1980.

[30] M. Ubeyli. Neutronic performance of new coolants in a fusion-fission (hybrid) reactor. *Fusion Engineering and Design*, 70(4):319 – 328, 2004.

[31] F. Najmabadi A. R. Raffray, D. Haynes. Ife chamber walls: requiremtns, design options and synergy with mfe plasma facing components. *Fusion eng. Des*, 23-31:313–316, 2003.

[32] Meier et al. Osiris and sombrero inertial fusion power plant designs: Final report. *WJSA-92-01(DOE/ER/54100-1)*, 1992.

[33] R. W. Moir. Liquid wall inertial fusion energy power plants. *Fusion eng. Des*, 32-33:93–104, 1996.

[34] M. A. Abdou W.R. Meier, R. Moir. Chamber technology concepts for inertial fusion energy - three recent examples. *Fusion eng. Des*, 42:537–548, 1992.

[35] HiPER Team. HiPER: Technical background and conceptual design report 2007. page 173.

[36] J.P Anthes R.E. Palmer and M.A. Palmer. The effect of background gas on the propagation of a high-intensity nd:glass laser beam to a target. *J. Appl. Phys*, 52, 1981.

[37] Mao-hong LU and Yu-mei LIU. Suppression of stimulated hyer-raman scattering in lithium vapor. *Applied Physics B: Lasers and Optics*, 57:167–176, 1993. 10.1007/BF00334531.

[38] A. J. Mackinnon, M. Borghesi, A. Iwase, M. W. Jones, G. J. Pert, S. Rae, K. Burnett, and O. Willi. Quantitative study of the ionization-induced refraction of picosecond laser pulses in gas-jet targets. *Phys. Rev. Lett.*, 76:1473–1476, Feb 1996.

[39] J.F Latowski S.C Wilks, B.I Cohen and E.A. Williams. Beam propagation for the laser inertial confinement fusion-fission energy engine.

[40] G. Sarri, C. A. Cecchetti, R. Jung, P. Hobbs, S. James, J. Lockyear, R. M. Stevenson, D. Doria, D. J. Hoarty, O. Willi, and M. Borghesi. Spatially resolved measurements of laser filamentation in long scale length underdense plasmas with and without beam smoothing. *Phys. Rev. Lett.*, 106:095001, Feb 2011.

[41] M. E. Sawan. Geometrical, spectral and temporal differences between ICF and MCF reactors and their impact on blanket nuclear parameters. *Fus Tech*, 10:1483–1488, 1986.

[42] B.Badger et al. A light ion beam fusion conceptual reactor design. *KfK*, 4710, 1980.

[43] DOE Team. A technology roadmap for generation iv nuclear energy systems. *U.S DOE Nuclear Energy Research Advisory Committee and the Generation IV International Forum*, Dec 2002.

[44] M Gasparotto R Andreani. Overiew of fusion nuclear technology in europe. *Fus Eng Des*, 61-62:27–36, 2002.

[45] A Sagara A Ying S Malang, A R Raffray. Range of blanket concepts from near term solutions to advanced concepts. *Fus Eng Des*, 61-62:295–306, 2002.

[46] M Futterer J Reimann L Giancarli, G Benamati.

[47] S. Lanza M. Vezzani, N Cerullo. Energetic-economic analysis of inertial fusion power plants with tritium commercial production. *Fus Eng Des*, 51-52:1143–1148, 2000.

[48] D.K. Sze J. reimann A. Terlain H. Moriyama, S. Tanaka. Tritium recovery from liquid metals. *Fus Eng Des*, 28:226–239, 1995.

[49] G. Gervasini and F. Reiter. Tritium inventory and permeation in seperately cooled liquid breeder blankets. *Journal of Nuclear Materials*, 168:304–311, 1989.

[50] Peter Hubberstey, Tony Sample, and Marten G. Barker. Is pb-17li really the eutectic alloy? a redetermination of the lead-rich section of the pb-li phase diagram. *Journal of Nuclear Materials*, 191-194, Part A(0):283 – 287, 1992. <ce:title>Fusion Reactor Materials Part A</ce:title> <xocs:full-name>Proceedings of the Fifth International Conference on Fusion Reactor Materials (ICFRMS-5)</xocs:full-name>.

[51] J. H. DeVan J. R. Keiser and E. J. Lawrence. Compatability of molten salts with type 316 steel and lithium. *J. Nucl. Matter*, 85-86:295–298, 1979.

[52] H Moriyama, A Sagara, S Tanaka, R.W Moir, and D.K Sze. Molten salts in fusion nuclear technology. *Fusion Engineering and Design*, 39-40(0):627 – 637, 1998.

[53] Dale L. and Smith. Evaluation of candidate blanket materials for fusion reactor blanket applications. *Journal of Nuclear Materials*, 122(1-3):51 – 65, 1984.

[54] S. Fukada, Y. Edao, S. Yamaguti, and T. Norimatsu. Tritium recovery system for lipb loop of inertial fusion reactor. *Fusion Engineering and Design*, 83(5-6):747 – 751, 2008.

[55] R. Kirchner J. Riemann and D. Rackel. Tritium recovery from nak-cold traps: investigation of hydrogen release kinetics. *Fus Eng Des*, 18:67–72, 1991.

[56] J. Reimann. Tritium inventory and recovery for a self-cooled pb-li blanket. *Fus Eng Des*, 14:413–425, 1991.

[57] D. K. sze and P. A. Finn. Combined gettering and molten salt process for tritium recovery from lithium. *Fus Eng Des*, 8:339–344, 1989.

[58] S.D Clinton and J.S Watson. The solubility of tritium in yttrium at temperatures from 250 to 400. *Journal of the Less Common Metals*, 66(1):51 – 57, 1979.

[59] F.J. Smith. The solubility of hydrogen isotopes in lithium. *Proc. 9th Symp. Fusion Technology, CONF-760630*, page p325, 1976.

[60] R. D. Wolson V. A. Maroni and G. G. Staahl. Some preliminary considerations of a molten salt extraction process to remove tritium from liquid lithium fusion reactor blankets. *Nucl. Technol*, 25:83, 1975.

[61] Hirotake Moriyama, Teruhito Nagae, and Yasuhiko Ito. Solubility of molten salt into liquid lithium. *Journal of Nuclear Materials*, 211(3):231 – 235, 1994.

[62] IAEA. Classification of nuclear waste, safety series no. 111-g1.1 safety guides, iaea, vienna, austria. 1994.

[63] Csullog et al. The iaea net-enabled waste managment database. *Proceedings of the Waste management 01 conference, Tucson, Arizona, USA*, 2001.

[64] E.T Cheng S. Fetter and F.M. Mann. Long-term radioactive waste from fusion reactors: Part ii. *Fus Eng Des*, 13:239–246, 1990.

[65] G. Olsson K. Broden, M. Lindberg. Management of waste from six potential fusion power plant models. *Fus Eng Des*, 54:349–352, 2001.

[66] M. Zucchetti, L.A. El-Guebaly, R.A. Forrest, T.D. Marshall, N.P. Taylor, and K. Tobita. The feasibility of recycling and clearance of active materials from fusion power plants. *Journal of Nuclear Materials*, 367-370, Part B(0):1355 – 1360, 2007. <ce:title>Proceedings of the Twelfth International Conference on Fusion Reactor Materials (ICFRM-12)</ce:title> <xocs:full-name>Proceedings of the Twelfth International Conference on Fusion Reactor Materials (ICFRM-12)</xocs:full-name>.

[67] L.A. El-Guebaly. Managing fusion high-level waste - a strategy for burning the long-lived products in fusion devices. *Fus Eng Des*, 81:1321–1326, 2006.

[68] P. Wilson D. Henderson, L. El-Guebaly and A. Abdou. Activation, decay heat and waste disposal analysis for aries-at power plant. *Fusion Technology*, 39:444–448, 2001.

[69] L. El-Guebaly. Aries-st nuclear analysis and sheild design. *Fus Eng Des*, 65:263–284, 2003.

[70] D.F.McGinnes. Waste sources and classification. *Deep geological disposal of radioactive waste*, 9, 2007.

[71] J. P. Witherspoon andR. E. Blanco J. P. McBride, R. E. Moore. Radiological impact of airborne effluents of coal and nuclear plants. *Science*, 8:1045–1050, 1978.

[72] L. Di Pace C. Girard N. P. Taylor I. Cook, G. Marbach. Safety and environmental impact of fusion. *EUR (01) CCE-FU / FTC 8/5*, 2001.

[73] J. Sanz J.F. Latowski and J.L. Vujic. The impact of pulsed irradiation upon neutron activation calculations for inertial and magnetic fusion energy power plants. *Fus tech*, 30:1470–1474, 1996.

[74] Steve Fetter, E.T. Cheng, and F.M. Mann. Long-term radioactivity in fusion reactors. *Fusion Engineering and Design*, 6(0):123 – 130, 1988.

[75] J. Sanz S. Reyes and J. F. Latowski. Use of clearance indexes to assess waste disposal issues for the hylife-ii inertial fusion energy power plant design. *Fus Eng Des*, 63-64:257–261, 2002.

[76] IAEA-TECDOC-1000. Clearance of materials resulting from the use of radionuclides in medicine, industry and research.

[77] L. El-Guebaly.

[78] M.A. Hoffman and Y.T. Lee. Impact of improvements in hylife-ii on safety, performance and cost. *Fusion Engineering and Design*, 29(0):105 – 110, 1995.

[79] Ralph W. and Moir. Liquid wall inertial fusion energy power plants. *Fusion Engineering and Design*, 32-33(0):93 – 104, 1996. <ce:title>Proceedings of the Seventh International Symposium on Heavy Ion Inertial Fusion</ce:title>.

[80] Sumer Sahin and Mustafa Ubeyli. Radiation damage studies on the first wall of a hylife-ii type fusion breeder. *Energy Conversion and Management*, 46(20):3185 – 3201, 2005.

[81] Evaluation of hylife-ii and sombrero using 175- and 566-group neutron transport and activation cross sections. *Fusion Engineering and Design*, 51-52.

[82] S Reyes, J Sanz, and J.F Latkowski. Use of clearance indexes to assess waste disposal issues for the hylife-ii inertial fusion energy power plant design. *Fusion Engineering and Design*, 63-64(0):257 – 261, 2002.

[83] Lee et al. *Fusion technology*, 26:74, 1994.

[84] Lester M. and Waganer. Innovation leads the way to attractive inertial fusion energy reactors 'prometheus-l and prometheus-h'. *Fusion Engineering and Design*, 25(1-3):125 – 143, 1994.

[85] Wayne R. Meier, Ralph W. Moir, and Mohamed A. Abdou. Chamber technology concepts for inertial fusion energy - three recent examples. *Fusion Engineering and Design*, 42(1-4):537 – 548, 1998.

[86] K. Weyrich and D.H.H. Hoffmann. Environmental aspects of tritium and active waste - a comparison of four inertial confinement fusion reactor concepts. *Fusion Engineering and Design*, 32-33(0):127 – 131, 1996. <ce:title>Proceedings of the Seventh International Symposium on Heavy Ion Inertial Fusion</ce:title>.

[87] Sviatoslavsky et al. A krf laser driven inertial fusion reactor 'sombrero'. *UWFDM-889: Technology of fusion energy meeting*, 1992.

[88] Sviatoslavsky et al. 'sombrero' a solid breeder moving bed krf laser driven ife reactor. *UWFDM-889: Technology of fusion energy meeting*, 1991.

[89] M.E. Sawan and H.Y. Kharter. Nuclear analysis for the blanket and shield of the krf laser driven inertail fusion reactor sombrero. *Symposium of fuion engineering*, 1993.

[90] I.N. Sviatoslavsky H.Y. Khater, M.E. Sawan and L.J. Wittenberg. Saftey analysis for.

[91] H. Bateman. Solution of a system of differential equations occurring in the theory of radio-active transformations. *Proc. Cambridge Phil. Soc*, 423, 1910.

[92] R.A. Forrest. *FISPACT-2007: User Manual.* UKAEA FUS 534, <www.fusion.org.uk>, London, UK.

[93] O. Cabellos J. Sanz and N. Garcia-Herranz.

[94] P P H Wilson. Phd thesis: ALARA: Analytic and laplacian adaptive radioactivity analysis.

[95] Q. Wang and D. L. Henderson. Racc-pulse: A version of the RACC radioactivity code for pulsed intermittent activity analysis. *UWFDM-980*, 1995.

[96] Charles F. Moler, Cleve; Van Loan. Nineteen dubious ways to compute the exponential of a matrix, twenty-five years later. *SIAM Review*, 45:3–49, 2003.

[97] D.L. Henderson J.E. Sisolak, S.E. Spangler. Pulsed/intermittent activation is fusion energy reactor systems. *UWFDM*, 882, 1992.

[98] *A General Monte Carlo N-Partcile Transport Code, V 2.6.0.* Los Alamos National Laboratory, 2008.

[99] W. Haeck. VESTA User's Manual - Version 2.0.0. *IRSN DSU/SEC/T/2008-331 - Index A* , Institut de Radioprotection et de Surete Nucleaire, France, 2009.

[100] NEA/SINBAD fusion shielding benchmark database: FNS-W, 2006.

[101] Andrew Davis. Private communication.

[102] P. Batistoni et al. Experimental validation of shutdown dose rates. *ITER task T-462 final report*, June 2001.

[103] EASY-II European Activation SYstem. http://www.ccfe.ac.uk/EASY.aspx.

[104] E. Fridman G. Lomonaco E. Shwageraus E. Bomboni, N. Cerullo. Comparison among MCNP-based depletion codes applied to burnup calcuations of pebble-bed HTR lattices. *Nuclear Engineering and Design*, 240:918–924, 2010.

[105] Federico Puente Espal, Chanatip Tippayaku, Kostadin Ivanov & Stefan Misu. MCOR - Monte carlo depletion code for reference LWR calculations. *Annals of Nuclear Energy*, 38:731–741, 2011.

[106] Bernard Verboomen Wim Haeck. *ALEPH 1.1.2 - A Monte Carlo Burn-Up Code.* 2006.

[107] Ferritic/martensitic steels - overview of recent results. *Journal of Nuclear Materials*, 307-311(0):455 – 465, 2002.

[108] M. Abdou et. al. Deuterium-tritium fuel self-sufficiency in fusion reactors. *Fusion Technology*, 9, 1986.

[109] L. W. Packer A. Aures and S. Zheng. Tritium self-sufficiency of hcpb blanket modules for demo considering time-varying neutron flux spectra and materials compositions. *SOFT 2012.*

[110] Heat deposition, damage, and tritium breeding characteristics in thick liquid wall blanket concepts. *Fusion Engineering and Design*, (0):719 – 725, 2000.

[111] R. Pampin. Long-term activation and tritium generation of flowing lithium-lead under prolonged irradiation in fusion power plants. *Fusion Science and technology*, 50:528, 2006.

[112] S. Malang, H. Schnauder, M. S. Tillack. Combination of a self-cooled liquid metal breeder blanket with a gas turnine power conversion system. *Fusion Engineering and Design*, 41:561–567, 1998.

[113] A. Li Puma et al. Breeding blanket design and sytems integration for a helium-cooled lithium-lead fusion power plant. *Fus Eng Des*, 81:469–476, 2006.

[114] P. rocco G. Casini and M. Zuchetti. Radioactivity effects of pb-17li in fusion power reactors. *Fus Eng Des*, 17:351–357, 1991.

[115] Yong Song, Qunying Huang, Yongliang Wang, and Muyi Ni. Analysis on tritium controlling of the dual-cooled lithium lead blanket for fusion power reactor fds-ii. *Fusion Engineering and Design*, 84(7-11):1779 – 1783, 2009. <ce:title>Proceeding of the 25th Symposium on Fusion Technology</ce:title> <ce:subtitle>(SOFT-25)</ce:subtitle>.

[116] YangQuan Chen Dingyu Xue and Derek P. Atherton. *Control System Design*. SIAM, 2007.

[117] Karl Johan Astrom. *Control System Design*. 2002.

[118] http://zone.ni.com/devzone/cda/tut/p/id/3782. National instruments - pid thoery explained.

[119] J.G. Ziegler & N.B. Nichols. Optimum settings for automatic controllers. *Trans. ASME*, 64:759–768, 1942.

[120] MOHD FADZLI BIN MOHD NORIS. Comparison between ziegler-nichols and cohen-coon method for controller tunings. *University College of Engineering & Technology Malaysia*, 2006.

[121] M. Gazelkaya, A. Eksin, and E. YeAYil. Self-tuning of pid-type fuzzy logic controller coefficients via relative rate observer. *Engineering Applications of Artificial Intelligence*, 16(3):227 – 236, 2003.

[122] S. BouallAgue, J. HaggAge, M. Ayadi, and M. Benrejeb. Pid-type fuzzy logic controller tuning based on particle swarm optimization. *Engineering Applications of Artificial Intelligence*, 25(3):484 – 493, 2012.

[123] P. Balasubramaniam. *Control, Computation and Information Systems: First International Conference on Logic, Information, Control and Computation*. Springer, 2011.

[124] B. Wayne Bequette. *Process Control: Modeling, Design and Simulation*. Prentice Hall, 2002.

[125] H. Feuerstein. Self-adjustment of Li in Pb-17Li systems. *J. Nucl. Mater.*, pages 505–507, 1998.

[126] J Sidell. A digital computer program for the solution of stiff sets of ordinary value, first order differential equations. *AEEW-R-799*, 1972.

[127] P. Lancaster and M. Tismenetsky. *The Theory of Matrices*. Academic Press.

[128] L.J. Cummings H.A. Ashi and P.C. Matthews. Comparison of methods for evaluating functions of a matrix exponential. *Applied Numerical Mathematics*, 59:468–486, 2009.

[129] Jerome Soucy. A short introduction to pade approximants.

[130] G. H. Golub and C.F. van Loan. *Matrix Computations*. North Oxford Academic, Oxford, UK, 1983.

[131] N. J. Higham. The scaling and squaring method for the matrix exponential revisited. *SIAM J. Matrix Anal. Appl.*, 26:1179–1193, 2005.

[132] B. N. Parlett. A recurrence among the elements of functions of triangular matrices. *Linear Algebra Appl.*, 14:117–121, 1976.